Geological Evolution of Asteroid Vesta from Dawn Orbital Observations and meteorite Analogs

Ottaviano Rüsch

PhD dissertation

Westfälische
Wilhelms-Universität
Münster

Background image: Dawn Framing Camera image of Vesta during the approach phase.

Fach Planetologie

Inaugural-Dissertation zur Erlangung des Doktorgrades der Naturwissenschaften
im Fachbereich Geowissenschaften der Mathematisch-Naturwissenschaftlichen
Fakultät der Westfälischen Wilhelms-Universität Münster

Surface Evolution of the Asteroid Vesta from Dawn Orbital Observations and Meteorite Analogs

---

vorgelegt von

Ottaviano Rüsch

aus Locarno, Schweiz

Dekan: ……..

Erster Gutachter: ...……..

Zweiter Gutachter: ...……..

Tag der mündlichen Prüfung: ...……..

Tag der Promotion: ...……..

Lebenslauf

Ottaviano Rüsch

Adresse:

Schillerstraße 64, 48155 Münster.

Geburtsort und -datum:

Locarno, Schweiz, 27 April 1987.

Staatsangehörigkeit und Familienstand:

Schweiz, ledig.

Ausbildung:

09.2011 – 11. 2014	Promotion am Institut für Planetologie, Westfälische Wilhelms-Universität, Münster, Deutschland.
09.2009 – 06.2011	Master in Planetologie an der Universität Paris Süd 11, Orsay, Frankreich.
09.2006 – 06.2009	Bachelor in Geologie an der Universität Lausanne, Lausanne, Schweiz.
09.2002 – 06.2006	Abitur am Liceo Cantonale Locarno, Locarno, Schweiz.

Auszeichnung:

NASA Group Achievement Award to Dawn Science Team, 07.2013.

Mitgliedschaft:

American Geophysical Union (AGU) seit 2011
Schweizerische Astronomische Gesellschaft (SAG) seit 2003

Veröffentlichungen:

Zeitschrift der Schweizerischen Astronomischen Gesellschaft (*Orion*). *No. 385* (2014); *No.374* (2013), *No. 317* (2003).

Sprachen:

Italienisch (Muttersprache), Französisch, Englisch, Deutsch

Münster, 7 März 2015

Eidesstattliche Erklärung

Hiermit versichere ich, dass ich die vorgelegte Dissertation selbst verfasst und keine anderen als die angegebenen Quellen und Hilfsmittel benutzt habe. Die aus anderen Quellen wörtlich oder inhaltlich übernommenen Stellen sind unter Angabe des Literaturzitates gekennzeichnet. Diese Arbeit hat in gleicher oder ähnlicher Form noch keiner Prüfungsbehörde vorgelegen.

Ottaviano Rüsch Münster, 7 März 2015

Contents

Abstract

The asteroid (4) Vesta is a ~500 km large main belt silicate body that accreted and differentiated a few million years after condensation of the solar nebula. Terrestrial planets have formed by accretion of similar planetary embryos. Thus, Vesta is interpreted as a survivor protoplanet and the knowledge it yields is essential to understand the early stages of planet formation.

To support mineralogical investigations of Vesta´s surface with near-infrared remote sensing observations, I performed mineralogical and near-infrared (0.7-2.5 µm) analyses of 24 howardite-eucrite-diogenite (HED) meteorites analog to Vesta´s surface. With these analyses, I established an empirical calibration relating the wavelength position of absorption bands to average pyroxene compositions. Compared to previous studies, this calibration is based on a larger meteorites sample and on consistent analyses. I characterized the influence of observation geometry on several spectral features of HED near-infrared spectra (i.e., wavelength position and depth of absorption bands, spectral slopes, band area ratio). I determined the range of phase angles within which the compositional variations (i.e., admixture of olivine or low-albedo material to pyroxene mixture) can be distinguished from observation geometry effects.

I retrieved near-infrared reflectance spectra from the first orbital observations of Vesta acquired by the visible to near-infrared imaging spectrometer (VIR) onboard the Dawn spacecraft. Quantitative analyses of the VIR reflectance spectra using a radiative transfer model revealed the presence of low-Ca and low-Fe pyroxene, high-Ca pyroxene, feldspar and olivine. The ubiquitous presence of such components confirmed a compositionally homogeneous upper layer (i.e., regolith). I applied the empirical calibration to VIR reflectance spectra and found that Vesta´s iron-poor terrains have a $Fs_{30}Wo_5$ pyroxene composition, whereas iron-rich terrains have an average $Fs_{47}Wo_{14}$ pyroxene composition. This confirms that, despite a compositionally homogeneous regolith, different terrains are preserved on Vesta, possibly formed during an early magmatic period. The composition and geologic context of these terrains are broadly consistent with differentiation models for the HED parent body. In addition, I exploited the unprecedented spatial resolution of the VIR reflectance spectra to determine the global spatial distribution of olivine-enriched material on Vesta. A concentration of olivine-enriched areas was found in the northern hemisphere.

I exploited the Dawn Framing Camera (FC) observations to compile a photo-geological map of the northern hemisphere (22°N-90°N) and determine the stratigraphy using dating by

crater size-frequency distribution. The northern hemisphere is composed of an ancient (pre-Veneneian epoch), densely cratered terrain, partly disrupted by a subdued tectonic system of troughs and ridges, possibly formed by a large impact (Veneneian epoch). The presence of olivine-enriched material in such a geologic context partly contradicts many pre-Dawn concepts of Vesta´s interior structure and differentiation based on the HED parent body.

As a consequence, new scenarios for the early evolution of Vesta (pre-Veneneian epoch) have been proposed by other studies. However, none provide consistent explanation for the entire range of observations reported here. In addition, the thesis revealed the geological evolution of the olivine-enriched lithologies of Vesta after the pre-Veneneian epoch. Most lithologies are probably the result of magmatic activity on Vesta and were redistributed across the surface as impact ejecta. Olivine-rich materials were exposed in recent time (Marcian epoch) by subsequent impacts and mass wasting.

Zusammenfassung

Der Asteroid (4) Vesta ist ein großer Silikatkörper des Hauptgürtels, welcher sich einige Millionen Jahre nach der Kondensierung des solaren Nebels bildete und differenzierte. Terrestrische Planeten bildeten sich durch die Anhäufung ähnlicher planetarer Embryos. Aus diesem Grund wird Vesta als ein überlebender Protoplanet interpretiert dessen Wissenspotential ausschlaggebend ist, um die Frühphase der Planetenbildung zu verstehen.

Um die mineralogische Erforschung der Oberfläche Vestas zu unterstützen, habe ich mineralogische und Nahinfrarot-Analysen (0,7-2,5µm) von 24 Howardit-Eukrit-Diogenit-Meteoriten (HED) als Analoge zur Vestaoberfläche durchgeführt. Mit diesen Analysen habe ich eine empirische Kalibrierung ermittelt, welche die Wellenlängenpositionen von Absorptionsbändern in Beziehung zu durchschnittlichen Pyroxenzusammensetzungen setzt.

Im Vergleich zu bisherigen Studien, stützt sich diese Kalibrierung auf eine größere Anzahl an Meteoritenproben sowie einheitliche Analysen. Ich habe den Einfluss der Beobachtungsgeometrie auf einige spektrale Eigenschaften von HED-Nahinfrarot-Spektren beschrieben (d.h. Wellenlängenpositionen und Intensität von Absorptionsbändern, spektrale Steigungen, Bandflächenverhältnis). Ich habe festgestellt, dass Variationen der Zusammensetzung (d.h. Beimischung von Olivin oder niedrig-Albedo-Material zu Pyroxenmischungen) innerhalb einiger Phasenwinkelbereiche von Effekten der Beobachtungsgeometrie unterschieden werden können.

Ich habe die ersten orbitalen Beobachtungen von Vesta durch das visible to near infrared imaging spectrometer (VIR) an Bord der Dawn-Sonde entnommen. Unter der Verwendung eines Strahlungs-Transfermodells, zeigten quantitative Analysen der VIR-Reflektionsspektren die Präsenz von kalzium- und eisenarmen Pyroxen, kalziumreichen Pyroxen, Feldspat sowie Olivin. Das allgegenwärtige Auftreten solcher Komponenten bestätigte eine obere Schicht (d.h. Regolith) von homogener Zusammensetzung. Ich habe die empirische Kalibrierung auf VIR-Reflektionsspektren angewendet und fand heraus, dass eisenarme Gebiete Vestas eine $Fs_{30}Wo_5$-Pyroxenzusammensetzung haben, wohingegen eisenreiche Gebiete eine durchschnittliche $Fs_{47}Wo_{14}$-Zusammensetzung zeigen. Dies bestätigt, dass trotz eines Regoliths homogener Zusammensetzung, unterschiedliche Gebiete auf Vesta, womöglich aus einer frühen magmatischen Periode, bewahrt wurden. Die Zusammensetzung und der geologische Kontext dieser Gebiete stimmen grob mit Differenzierungsmodellen des HED-Mutterkörpers überein. Darüber hinaus, nutzte ich die zuvor unerreichte räumliche Auflösung der VIR-Reflektionsspektren, um die globale räumliche Verteilung von Olivin

reicherem Material auf Vesta zu bestimmen. Eine Konzentration von Olivin reicheren Gebieten wurde in der nördlichen Hemisphäre gefunden.

Ich nutzte Beobachtungen der Dawn Framing Camera (FC), um eine photogeologische Karte der nördlichen Hemisphäre (22°N-90°N) anzufertigen und die Stratigraphie mittels Datierungen durch Kratergrößen-Frequenzverteilungen festzustellen. Die nördliche Hemisphäre setzt sich aus altem (prä-Veneneianische Epoche), stark verkratertem Terrain zusammen, welches teilweise durchzogen ist von einem schwach ausgeprägten tektonischen System aus Gräben und Rücken, die möglicherweise durch einen Impakt gebildet wurden (Veneneia-Epoche). Das Auftreten von Olivin reicherem Material in einem solchen geologischen Kontext steht teilweise in Widerspruch zu vielen Konzepten zur inneren Struktur und Differenzierung Vestas aus der Zeit vor Dawn Untersuchungen.

In Folge dessen wurden neue Szenarios der frühen Entwicklung Vestas (prä-Veneneianische Epoche) in neuen Studien vorgeschlagen, von denen jedoch keines eine Erklärung aller hier präsentierten Beobachtungen bietet. Darüber hinaus zeigte diese Arbeit die geologische Entwicklung der olivinhaltigen Lithologien Vestas nach der prä-Veneneianischen Epoche auf. Die Lithologien sind vermutlich das Resultat magmatischer Aktivität Vestas und wurden als Impaktejekta über die Oberfläche verteilt. Olivinreiche Materialien wurden vor geologisch kurzer Zeit (Marcianische Epoche) durch Impakte und Hangrutschungen freigelegt.

Danksagung

Zuallererst möchte ich mich herzlich bei Prof. Dr. Harald Hiesinger bedanken - für die Möglichkeit, am Institut für Planetologie zu promovieren, für seine Kritik bezüglich meiner Arbeit sowie für die Einführung in die Forschungswelt. Des Weiteren möchte ich Knut Metzler, Andreas Morlok, Dennis Reiß, und Gino Erkeling danken, die mich stets motiviert haben und mich bei meiner wissenschaftlichen Arbeit unterstützt und beraten haben. Technische Unterstützung leisteten Thorsten Grund und Manuel Ahmedi. Die Zusammenarbeit mit den DoktorandInnen Hannes, Jackie, Kathrin, Jan-Hendrik und Jan sorgte für eine entspannte Arbeitsatmosphäre und eine tolle Zeit im Institut.

Für diese Arbeit habe ich auch von Forschern außerhalb des Instituts für Planetologie große Unterstützung bekommen: Aus dem Max Planck Institut für Sonnensystemforschung in Göttingen (Andreas Nathues, Vishnu Reddy), aus dem Instituto Nazionale di Astrofisica in Rom (Maria Cristina De Sanctis, Eleonora Ammannito), aus dem Deutsches Zentrum für Luft und Raumfahrt (Ralf Jaumann, Thomas Roatsch), sowie aus der Freien Universität Berlin (Nico Schmedemann, Thomas Kneissl). Darüber hinaus gab mir Edward Cloutis von der Universität Winnipeg hilfreiche Anregungen.

Entstanden ist die Doktorarbeit zu einem großen Teil anhand der Verarbeitung der durch die NASA Dawn Mission erworbenen Daten. Dafür möchte ich mich bei dem Dawn Principal Investigator C.T. Russell sowie den Dawn Mitgliedern bedanken. Die zahlreichen und ertragreichen Diskussionen mit den Dawn Mitgliedern beeinflussten meine wissenschaftliche Arbeit positiv.

Für die maßgebliche Begleitung vor und während meiner Doktorarbeit danke ich meinen ehemaligen Dozenten und Forschern der Universität Paris Sud 11, Francois Poulet, Mathieu Vincendon, und Frédéric Schmidt. (*Merci!*)

Auch meine Familie (*Grazie!*) und meine Freundin haben zum Erfolg dieser Doktorarbeit beigetragen.

7 März 2015

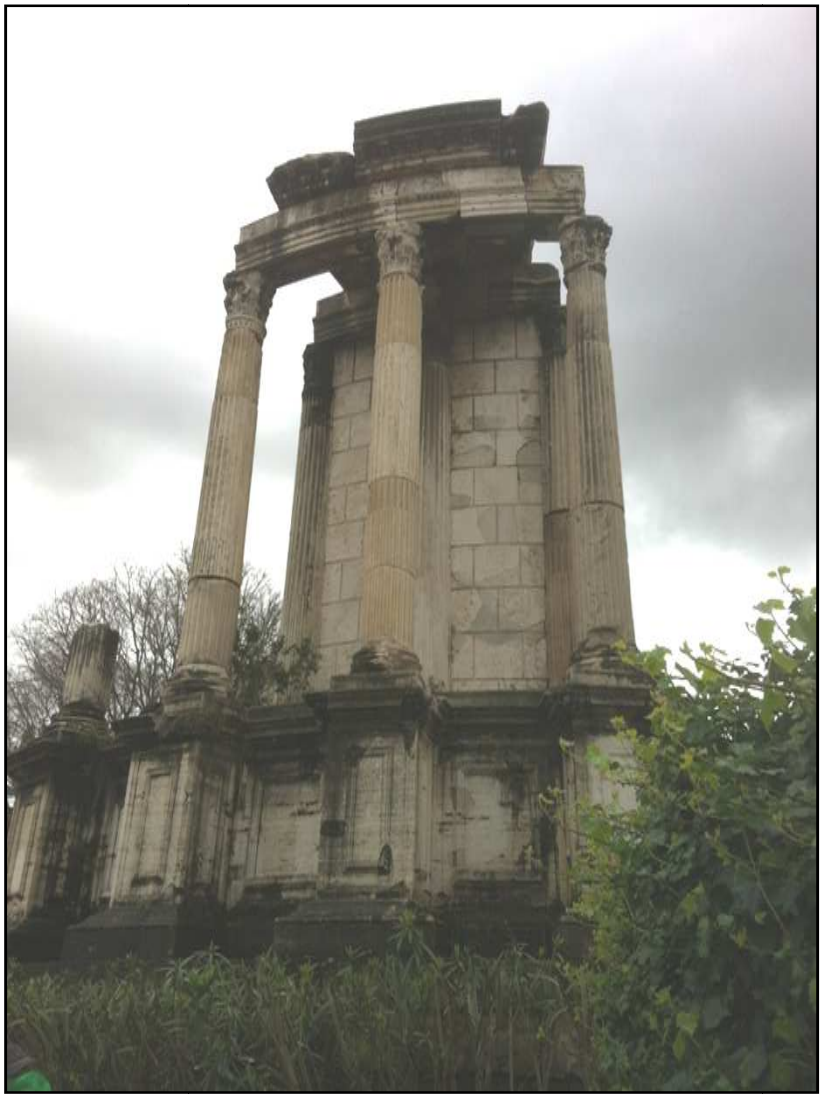

The ruins of the temple of Vesta in the Roman Forum, Rome.

„Mit dem grössten Vergnügen eile ich, Ihnen, mein theuerster verehrungswürdigster Freund! Anzugeigen, dass ich so glücklich gewesen bin, am 29. März abermals *einen neuen Planeten,* von der Familie der Asteroiden, zu entdecken. Diesmal war die Entdeckung eigentlich kein Zufall, und hätten Witterung und Mondschein es nicht verhindert, so würde ich diesen Mitbürger unseres Sonnensystems wenigstens schon 14 Tage früher aufgefunden haben. Nach meiner Hypothese über diese Asteroiden nämlich – deren Wahrheit oder Falschheit ich übrigens dahin gestellt sein lasse, und die ich nur dazu benutze, wozu Hypothesen nur überhaupt nützlich sein können, nämlich uns zu und bei Beobachtungen zu leiten – habe ich, wie Ihnen bekannt ich, gefolgert, dass alle Asteroiden, deren es noch sehr viele geben mag, den nord-westlichen Theil des Gestirns der Jungfrau und den westlichen Theil des Gestirns des Wallfisches passiren müssen. Regelmässig durchmustere ich also, jeden Monat einmal, einen mir mit allen seinen Sternen sehr bekannt gewordenen Theil desjenigen dieser beiden Gestirne, das gerade seiner Opposition am nächsten ist. Als ich am 29. März Abends bald nach 8 Uhr eine solche Durchmusterung des nördlichen Flügels der Jungfrau vornahm, fiel mir sogleich ein unbekannter heller Stern, wenigstens von der 6. Grösse, westlich von No. 223 Ihres Verzeichnisses und No. 20 ηv Flamsteed auf, den ich ohne Bedenken augenblicklich für einen neuen Planeten hielt.“

Wilhelm Olbers, 3. April 1807,

Astronomishes Jahrbuch für 1810, S. 194-201

in Schilling, Wilhelm Olbers: Sein Leben und Seine Werte, 1894

Preface

This thesis is based on peer reviewed articles submitted and published by the author in scientific journals. Three first-authored articles present the main results of the thesis related to the spectral properties of HED meteorites, to the geology and mineralogy of Vesta and were entitled:

Article I	*Near infrared spectroscopy of HED meteorites: Effects of viewing geometry and compositional variations* submitted to Icarus, 03.2015 by **Ruesch, O.**, H. Hiesinger, E. Cloutis, L. Le Corre, J. Kallisch, P. Mann, K. Markus, K. Metzler, A. Nathues, and V. Reddy.
Article II	*Detections and geologic context of local enrichments in olivine on Vesta with VIR/Dawn data* in Journal of Geophysical Research, 2014a, volume 119, issue 9, pages 2078-2108. by **Ruesch, O.**, H. Hiesinger, M. C. De Sanctis, E. Ammannito, E. Palomba, A. Longobardo, M. T. Capria, F. Capaccioni, A. Frigeri, F. Tosi, F. Zambon, S. Fonte, G. Magni, C. A. Raymond and C. T. Russell.
Article III	*Geologic map of the northern hemisphere of Vesta based on Dawn Framing Camera (FC) images* in Icarus, 2014b**,** volume 244, pages 41-59. by **Ruesch, O.**, H. Hiesinger, D. T. Blewett, D. A. Williams, D. Buczkowski, J. Scully, R. A. Yingst, T. Roatsch, F. Preusker, R. Jaumann**,** C. T. Russell, and C. A. Raymond.

Six additional peer reviewed journal articles were published by the author in collaboration with scientists of the Dawn team. These articles describe results that support the discussion presented in this thesis. Of these six articles, three co-authored publications describe results of

spectral analyses and the detection and characterization of the minerals pyroxenes and olivine on Vesta's surface:

Article IV	*Modal mineralogy of the surface of Vesta: evidence for ubiquitous olivine and identification of meteorite analogue* in Icarus, 2014, in press. by Poulet, F., **O. Ruesch**, Y. Langevin, and H. Hiesinger.
Article V	*Olivine in an unexpected location on Vesta's surface* in Nature, 2013, volume 504, pages 122–125. by Ammannito, E., M. C. De Sanctis, E. Palomba, A. Longobardo, D. W. Mittlefehldt, H. Y. McSween, S. Marchi, M. T. Capria, F. Capaccioni, A. Frigeri, C. M. Pieters, **O. Ruesch**, F. Tosi, F. Zambon, F. Carraro, S. Fonte, H. Hiesinger, G. Magni, L. A. McFadden, C. A. Raymond, C. T. Russell and J. M. Sunshine.
Article VI	*Small fresh impact craters on asteroid 4 Vesta: A compositional and geological fingerprint* in Journal of Geophysical research, 2014, volume 119, issue 4, pages 771-797. by Stephan, K., R. Jaumann, M. C. De Sanctis, F. Tosi, E. Ammannito, K. Krohn, F. Zambon, S. Marchi, **O. Ruesch**, K.-D. Matz, F. Preusker, T. Roatsch, C. A. Raymond and C. T. Russell.

Three additional publications present details of specific geological features of the northern hemisphere and the production and chronology functions necessary for dating surface units:

Article VII	*Vesta's north pole quadrangle Av-1 (Albana): Geologic map and the nature of the south polar basin antipodes* in Icarus, 2014, volume 244, pages 13-22. by Blewett, D.T., D. L. Buczkowski, **O. Ruesch**, J. E. Scully, D. P. O'Brien, R. Gaskell, T. Roatsch, T. J. Bowling, A. Ermakov, H. Hiesinger, D. A. Williams, C. A. Raymond and C. T. Russell.
Article VIII	*Geomorphology and structural geology of Saturnalia Fossae and adjacent structures in the northern hemisphere of Vesta* in Icarus, 2014, volume 244, pages 23-40. by Scully, J. E.C., A. Yin, C.T. Russell, D.L. Buczkowski, D.A. Williams, D.T. Blewett, **O. Ruesch**, H. Hiesinger, L. Le Corre, C. Mercer, R.A. Yingst, W.B. Garry, R. Jaumann, T. Roatsch, F. Preusker, R.W. Gaskell, S.E. Schröder, E. Ammannito, C.M. Pieters, C.A. Raymond, the Dawn Science Team.
Article IX	*The cratering record, chronology and surface ages of (4) Vesta in comparison to smaller asteroids and the ages of HED meteorites* in Planetary and Space Science, 2014, volume 103, pages 104-130. by Schmedemann, N., T. Kneissl, B.A. Ivanov, G.G. Michael, R.J. Wagner, G. Neukum, **O. Ruesch**, H. Hiesinger, K. Krohn, T. Roatsch, F. Preusker, H. Sierks, R. Jaumann, V. Reddy, A. Nathues, S. Walter, A. Neesemann, C.A. Raymond and C.T. Russell.

This thesis reviews the above first-authored articles (Article I, II and III), and discuss their implications by inter-correlation with the other co-authored publications. The thesis has the following structure. Chapter 1 presents the rationale of this work; Chapter 2 gives background information on the Dawn mission instruments and HED meteorites; Chapter 3 covers the methods of data analyses, such as photo-geological and spectral mapping and dating of surface units. The summary of the results of Article I, II and III are found in Chapter 4. Chapter 5 discusses the implications of the articles´ main results. Concluding remarks are given in Chapter 6 and an outlook in Chapter 7. The complete articles are found in the appendix. This thesis is concluded by three non-peer-review outreach articles presenting

Vesta, the scientific outcomes of the Dawn mission at Vesta, and Dawn´s next target: the dwarf planet Ceres. The outreach articles are :

Rendez-vous avec l´astéroïde (4) Vesta
in Orion (Schweizerische Astronomische Gesellschaft), 2012,
volume 374, pages 16-20.
by **Ruesch O.**, J. Amalberti, G. Andjic.

Vesta sans voiles
in Orion (Schweizerische Astronomische Gesellschaft), 2014,
volume 385, pages 28-29.
by **Ruesch O.** and J. Amalberti

La planète naine Cérès
in Orion (Schweizerische Astronomische Gesellschaft), 2014,
volume 385, pages 26-27.
by **Ruesch O.**

1. Introduction

Towards the end of the eighteenth century, astronomers in central Europe realized that the ideal sequence of planets orbiting at predictable distances from the Sun (Titus-Bode law) was interrupted between Mars and Jupiter, at around 3 Astronomical Unit (AU). In the early years of the nineteenth century, objects with a star-like appearance were found in this gap by G. Piazzi, W. Olbers and K. Harding (e.g., Foderà Serio et al., 2002). It was recognized that a particular region now called the main belt existed in the Solar System, populated by bodies smaller than planets, but different from comets (e.g., Foderà Serio et al., 2002). Those bodies were designated as asteroids (Herschel, 1802). At the turn of the twentieth century, their improved understanding let to the distinction between the largest asteroids, one of which has been classified as dwarf planet (IAU Resolution, 2006), from the remaining significantly smaller asteroids. Such distinction reflects the current understanding of the main belt: a region where objects underwent the major stages of planet formation without accreting into a single large body (e.g., Kirkwood, 1867; Safranov, 1969; Weidenschilling and Cuzzi, 2006). These objects, termed proto-planets, were ~1000 km large bodies formed by accretion of kilometer-sized planetesimals (e.g., Greenberg et al., 1978; Wetherill and Stewart, 1989). Their material melted through radiative heating and possibly led to differentiation, i.e., the formation of a core surrounded by a mantle and a crust (e.g., McSween et al., 2002). At distances shorter than ~2 AU, proto-planets accreted to form the Earth and the other terrestrial planets. At around 3 AU, instead, the gravitational influence of Jupiter led to collisions and dynamical excitations that destroyed most of the objects leaving only few intact large proto-planets and a myriad of smaller shattered debris (e.g., Wetherill and Stewart, 1989; O´Brien and Sykes, 2011). The surviving proto-planets represent the only examples of relatively small, differentiated planetary bodies (e.g., Russell et al., 2006). Astronomical observations have revealed that they are compositionally different, i.e., different proto-planet are dominated by different silicates and ice/silicates mixtures (e.g., Hilton, 2002; Bus et al., 2002; Gaffey et al., 2002). Their diversity suggests variations in the primitive materials of the Solar Nebula, as well as different evolutionary paths between different proto-planets (e.g., de Pater and Lissauer, 2010; Russell et al., 2011). The surviving “planetary embryos” like Vesta and Ceres are thus crucial for the understanding of the early stages of terrestrial planets formation and for the early history of the Solar System (e.g., Russell et al., 2006). The relevance of such bodies for the understanding of the Solar System history was already understood by Wilhelm Olbers and Pierre-Simon Laplace, as they speculated about a possible genetic relationship between asteroids and meteorites (Schilling, 1894).

The “new citizen of the Solar System”, as Wilhelm Olbers refers to, or the fourth asteroid in order of discovery, was first observed by Olbers in Bremen, Germany, on March 29, 1807 (Schilling, 1894). Few months later C. F. Gauss suggested its name Vesta (Bode, 1825). During almost two centuries, scientific research dedicated to this asteroid was limited to orbital properties, albedo, and the size of the object. With a semi-major axis of 2.36 AU, Vesta emerged as an uncommon body due to its brightest albedo among asteroids and its large size (radius of ~280 km, McCarthy et al., 1994). Density estimates of ~ 3300 km/m^3 (actual value 3456 km/m^3, Russell et al., 2012) first hinted to a silicate-dominated body (Schubart and Matson, 1979). A major turning point in the knowledge about Vesta occurred with the first charged couple device (CCD) observations at the beginning of 1970 (e.g., McCord et al., 1970; McFadden et al., 1977). In reflectance observations between 0.4 and 1.1 µm an absorption band was identified and attributed to Fe^{2+} crystal field transitions as in pyroxene spectra, implying the predominance of basaltic material at the surface (McCord et al., 1970). A strong similarity was found between the spectra of Vesta and of achondrite meteorites, the howardites, eucrites, diogenites, HED (Chapman and Salisbury, 1973), forging for the first time the now widely-accepted asteroid-meteorite link (McCord et al., 1970; Binzel and Xu, 1993; Gaffey, 1993).

Vesta´s pyroxene dominated surface was interpreted as evidence for an intact, basaltic crust, differing from the more common silicate surfaces of asteroids composed of both pyroxene and olivine, and usually pointing to a more primitive or disrupted body (e.g., Gaffey et al., 2002). The basaltic crust confirmed that Vesta underwent internal differentiation (e.g., Keil, 2002). Such process was investigated in great detail on the basis of HED meteorites. The approach to consider HEDs as Vesta’s samples was first suggested by the very similar iron-bearing low calcium pyroxene, or pigeonite, and later by further evidences of the meteorite-asteroid link. It was shown that a significant quantity of material was ejected from Vesta during the formation of a large basin at the South Pole (Thomas et al., 1997). The impact site represented the possible source region of material that later formed the V-Type asteroids in the Vesta asteroid family (Vestoids) (Thomas et al., 1997). Small, <10 km wide, pigeonite-bearing asteroids (V-type) were detected between Vesta and the Kirkwood orbital resonance 3:1 (and also the ν_6 resonance), in a region representing an orbital pathway between Vesta and the Earth (Binzel and Xu, 1993). Near Earth Asteroids with V-type characteristics were also identified (Cruiskshank et al., 1991; Migliorini et al., 1997). Thus, meteoroids similar to the latter could have impacted on Earth in the past and delivered HED material (e.g., Migliorini et al., 1997). It is important to stress that these observations support the delivery of Vesta

material to Earth through orbital resonances, they do not constitute a definitive proof of the Vesta-HED link, however. Arguments suggesting the contrary arise from both studies of meteorites and astronomical investigations. Oxygen isotope ratios of most HEDs and iron IIIAB meteorites suggest a single source for both groups, implying that HEDs derive from a disrupted body, whereas Vesta is mostly intact (e.g., Clayton and Mayeda, 1996). In addition, the picture is further complicated by the fact that not all HEDs have identical oxygen isotope ratios, but there are some outliners, such as Ibitira and Pasamonte (e.g., Wiechert et al., 2004). This might suggest multiple bodies with a basaltic crust (e.g., Scott et al., 2009). Iron meteorites imply the formation of a few tens of protoplanets, which extensively melted and formed a basaltic crust (e.g., Burbine et al., 2002); HEDs should therefore come from different disrupted proto-planets and not a single body (e.g., Wasson, 2013). Astronomical observations indicate that many V-type asteroids are not related to the Vesta family and are probably collisional debris of disrupted differentiated bodies (e.g., Lazzaro et al., 2000; De Sanctis et al., 2011; Hardersen et al., 2014). The debate around this subject constitutes one of the motivations for this thesis. Note that a close to definitive establishment of the Vesta-HED link will probably require an isotopic analysis of Vesta´s rocks.

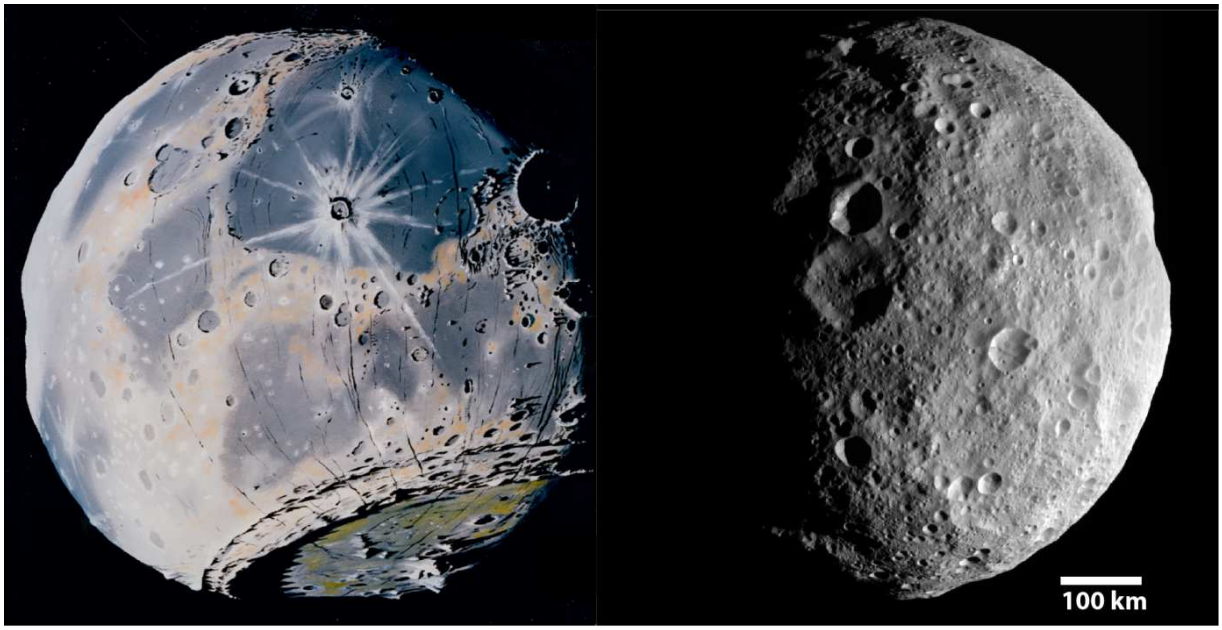

Figure 1.1 *Left: artist conception of Vesta before the launch of the Dawn mission. Vesta was depicted with a close to spherical shape despite the large impact basin at the South Pole. Note also darker lunar-like basaltic surfaces (Jerry Armstrong, 2000). Right: Dawn Framing Camera image of Vesta from an altitude of 6000 km centered on the North Pole. The surface is dominated by impact craters.*

The study of HED meteorites, and thus insight into the differentiation of Vesta is challenged by establishing the exact relationship between the crystallization of eucrites and diogenites on the HED parent body. Many eucrites represent basaltic material composed of pyroxenes and plagioclase, whereas diogenites are cumulate, orthopyroxenite rocks with minor olivine (e.g., Hutchison, 2004; McSween et al., 2011). One scenario assumes that Vesta underwent a single global melting episode, leading to a magma ocean (e.g., Takeda, 1979; Righter and Drake, 1997; Ruzicka et al., 1997). Its crystallization resulted in a thick olivine mantle and a lower and upper crust represented by diogenites and eucrites, respectively (e.g., Takeda, 1979; Righter and Drake, 1997; Ruzicka et al., 1997). This scenario predicted that the olivine dominated mantle would be uplifted and exposed in the South Pole impact site (e.g., Gaffey, 1997; McSween et al., 2011). However, because this model could not explain all geochemical and trace element diversities (e.g., Mittlefehldt, 1994; Fowler et al., 1995), alternative models were proposed. A model referred to as serial magmatism suggests that diogenites were mainly formed by intrusions (e.g., Mittlefehldt, 2000; Shearer et al., 2010) into an already existing eucritic crust (e.g., Barrat et al., 2010; Yamaguchi et al., 2011). The corollary of this latter model is that the olivine mantle would be thinner than in the magma ocean scenario (Yamaguchi et al., 2011).

The South Pole impact basin is a candidate location for crust and mantle investigations. For example, Pieters et al. (2011) argued that the structure of the first tens of kilometers of Vesta´s crust will provide information on the style of igneous activity and on the differentiation of the body. Similarly, Wilson and Keil (2012) proposed that volcanic constructs potentially present on today's surface of Vesta might be related to early magmatism, approximately 4.5 Ga ago. The morphologies and ages of these volcanic deposits were expected to inform on the type and history of Vesta's volcanism. The illustration of Vesta in Figure 1.1 is based on such prevision. On the other hand, HEDs also emphasize the role of impact cratering on the HED-Vesta parent body (e.g., Metzler et al., 1995). A first direct evidence for an intense bombardment history is the nature of the howardites: they consist of impact breccia of both eucrites and diogenite material (e.g., Bischoff et al., 2006).

The relevance and wide-reaching implications of the debated questions, such as how exactly Vesta differentiated and the details of its volcanic and impact history, justified the launch of a spacecraft for its close inspection. The NASA Discovery mission Dawn carries a payload consisting of three instruments from Germany, Italy and the United States: two redundant cameras (FC), a visible to near-infrared spectrometer (VIR) and a gamma-ray and neutron detector (GRaND) (Russell et al., 2003; 2011). Using ion propulsion, the spacecraft

reached the asteroid Vesta in July 2011 and stayed into orbit until August 2012 when it was redirected toward the dwarf planet Ceres for an encounter in March 2015 (Russell et al., 2013).

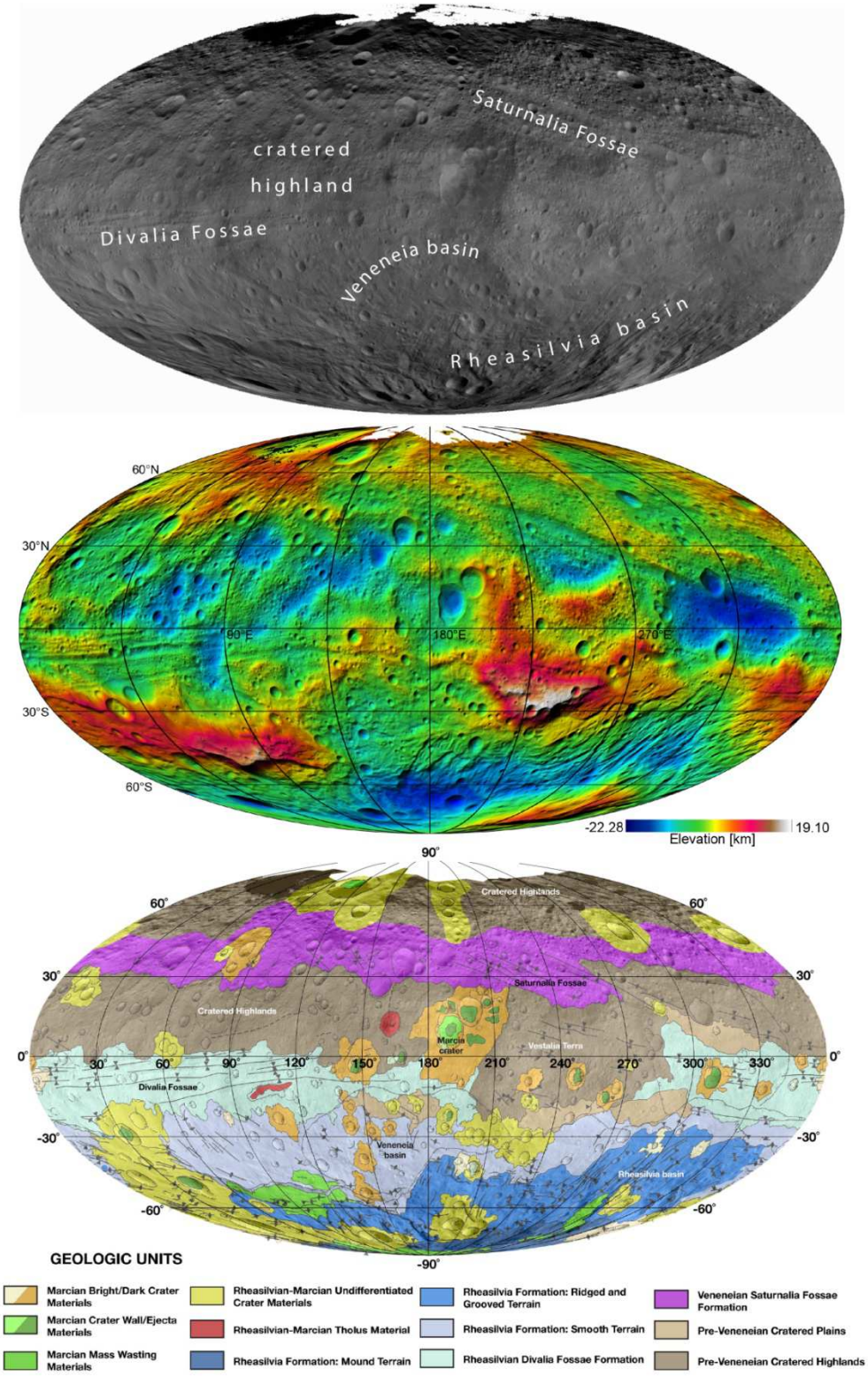

Figure 1.2 *Global mollweide projection of FC mosaic, topography and geologic map of Vesta (from top to bottom) derived from Dawn (Roatsch et al., 2013; Williams et al., 2014a). The geologic map is partly based on Ruesch et al., (2014b) - Article III. White areas at the North Pole are unobserved.*

As depicted in the global geologic map of Figure 1.2 produced from Dawn observations, Vesta´s surface is dominated by impact craters. The two largest craters, located in the southern hemisphere, named Rheasilvia and Veneneia, have formed two systems of troughs and ridges running along the equator and in the northern hemisphere (e.g., Jaumann et al., 2012; Williams et al., 2014a). On the rims of the two basins, ejecta resurfaced older terrains, whereas within their interior large-scale mass wasting occurred (e.g., Jaumann et al., 2012; Otto et al., 2013; Williams et al., 2014a). Morphological evidence for volcanism was not found due to the intense bombardment history (e.g., Williams et al., 2014b). Rare ridges of possible magmatic intrusions were identified, but magmatic structures in the crust were not found (Buczkowski et al., 2014). The ubiquitous presence of pyroxenes in Vesta´s regolith and in rocky outcrops was nevertheless taken as evidence for basaltic activity early in Vesta´s history (e.g., De Sanctis et al., 212). Briefly, Dawn revealed a body shaped by impact processes with no evidence for igneous-derived morphologies.

In this framework, this thesis focuses on specific geological regions and specific mineralogical characteristics in order to retrace the surface evolution from the initial surface built by igneous activity to the one observed today. Observations of Vesta in the near infrared spectral range were supported by laboratory analyses of meteorite analogues to Vesta, the HED meteorites. In particular, investigations focused on olivine, a tracer for ultramafic magmatism and ancient terrains in the northern hemisphere. Specifically, this thesis is structured by three intercorrelated subjects:

- Quantification of the effects of variable pyroxene composition and olivine and the effects of observation geometry on the near infrared reflectance properties of natural basaltic mixtures, analog to Vesta´s surface.
- On the basis of orbital near infrared observations, identification of any olivine-rich lithology on Vesta, and determination of its local morphology.
- Characterization of the geological history of the region bearing olivine-rich lithologies, i.e., the geology of the northern hemisphere.

To address these subjects, HEDs have been analyzed chemically and spectrally under varying observation and illumination conditions in the laboratory to constrain their variability. I exploited Dawn Framing Camera (FC) images to produce a geologic map and crater size-frequency distribution (CSFD) measurements of the northern hemisphere for absolute dating. In addition, I identified olivine on the surface and detailed its spatial distribution with reflectance spectroscopy, which exploits the electromagnetic spectrum between 0.4 and ~ 3.5

µm. Reflectance spectra were derived from the Dawn Visible to near InfraRed spectrometer (VIR).

2. Dawn operations, payload and HED meteorites

2.1 Dawn operations

Observations of Vesta by the Dawn instruments were performed from three different orbits with decreasing altitude, as depicted in Figure 2.1, starting July 2011 (Russell et al., 2013). This approach was necessary because the three scientific instruments on board had different requirements in terms of altitude of observation. The highest orbit named "Survey" provided an overview of the asteroid needed to plan subsequent mission phases. The "High Altitude Mapping Orbit" (HAMO-1) was optimized for the VIR and FC observations of equatorial and southern latitudes. Nominally, this phase is subdivided into 6 cycles, each cycle consisting of 10 orbits needed to cover the entire surface by the FC. Note that the northern hemisphere had seasonal shadows and was poorly illuminated during the HAMO-1 period. The "Low Altitude Mapping Orbit" (LAMO) was chosen mainly to satisfy the GRaND measurement requirements, although FC and VIR also acquired data. During LAMO, a cycle is defined as one week. Once having completed the observations at LAMO orbit, the spacecraft did not escaped the gravity of Vesta directly. Instead, it returned to the "High Altitude Mapping Orbit" altitude (HAMO-2) for additional FC and VIR measurements. This latter maneuver allowed for observations of the northern hemisphere of Vesta under improved illumination conditions. Also, additional time from unused operation margin after LAMO was available, and the HAMO-2 phase was further extended. A last set of data collection was performed at an altitude of ~6000 km during the departure phase. The spacecraft left Vesta gravitational attraction in August 2012 and was redirected to asteroid Ceres, for an encounter planned in March 2015 (Russell et al., 2013). Additional

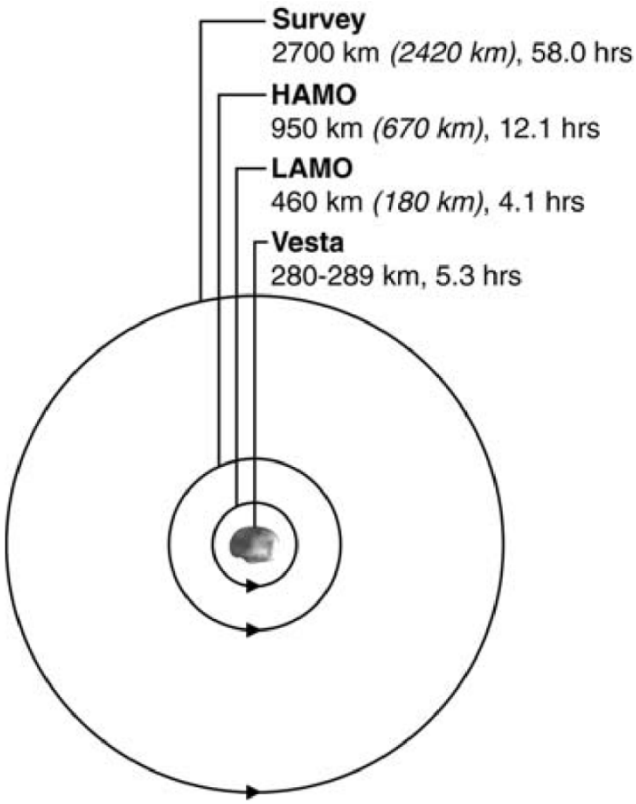

Figure 2.1 *Polar circular orbits of Dawn spacecraft around Vesta. The radius and times of revolution are approximate. Altitudes above Vesta are given in parenthesis (Russell et al., 2007).*

description of the orbital operations can be found in Polanskey et al. (2011).

The spacecraft itself makes use of an ion propulsion system with three thrusters, and electrical power from solar panels articulated around the y-axis (Figure 2.2). The three payload instruments are directly fixed to the spacecraft and pointing in the z direction (Figure 2.2). The high-gain antenna for down-link of science data is boresighted in the x direction. A detailed description of the spacecraft is presented in Rayman et al. (2006) and Thomas et al. (2011).

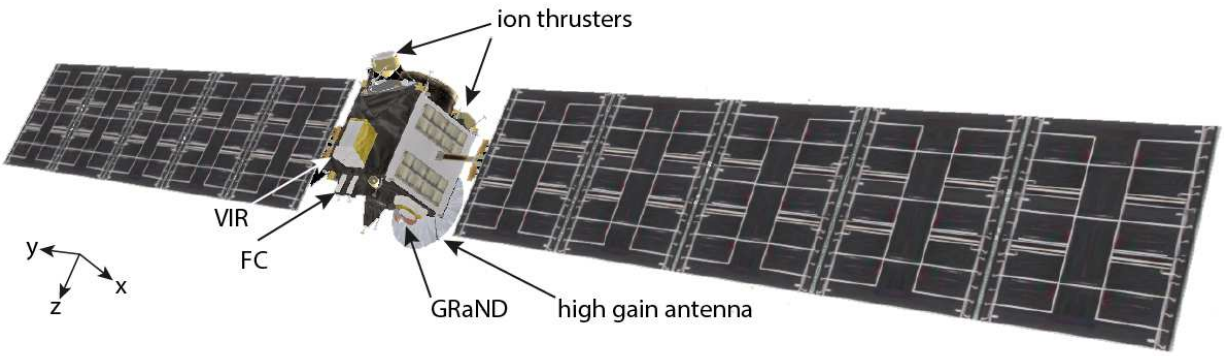

Figure 2.2 *Diagram of the Dawn spacecraft with the three instruments and key components. With deployed solar panels, as shown here, the spacecraft measures 20 m in width (diagram from Celestia – Chris Laurel).*

2.2 Framing Camera (FC)

Two redundant Framing Cameras were built and operated by the Max Planck Institut für Sonnensystemforschung with the participation of the Deutsches Zentrum für Luft und Raumfahrt, Institut für Planetenforschung (Sierks et al., 2011). During the operations at Vesta, only one camera was activated. Each camera has a panchromatic (clear) filter and 7 band-pass color filters covering the visible to near infrared range of the electromagnetic spectrum. The instantaneous field of view of 94 µrad/pixel provided a pixel scale of ~60 meters/pixel and ~20 meter/pixel at HAMO and LAMO altitudes, respectively. Over 99% coverage of Vesta´s surface was obtained with the clear filter during HAMO-1 and 2 (Russell et al., 2013).

Figure 2.3 depicts the different spatial coverages obtained during different mission phases with the FC clear-filter. In the area of study, the northern hemisphere, two factors led to large unobserved areas during LAMO: the season during data acquisition and large topographic variations. The limited coverage of the footprints at the northernmost latitudes and shadowed areas are evident in Figure 2.3. Such effects were reduced during HAMO-2 and the departure phase. Nevertheless, even for shadowed areas, the very high sensitivity of the FC CCD

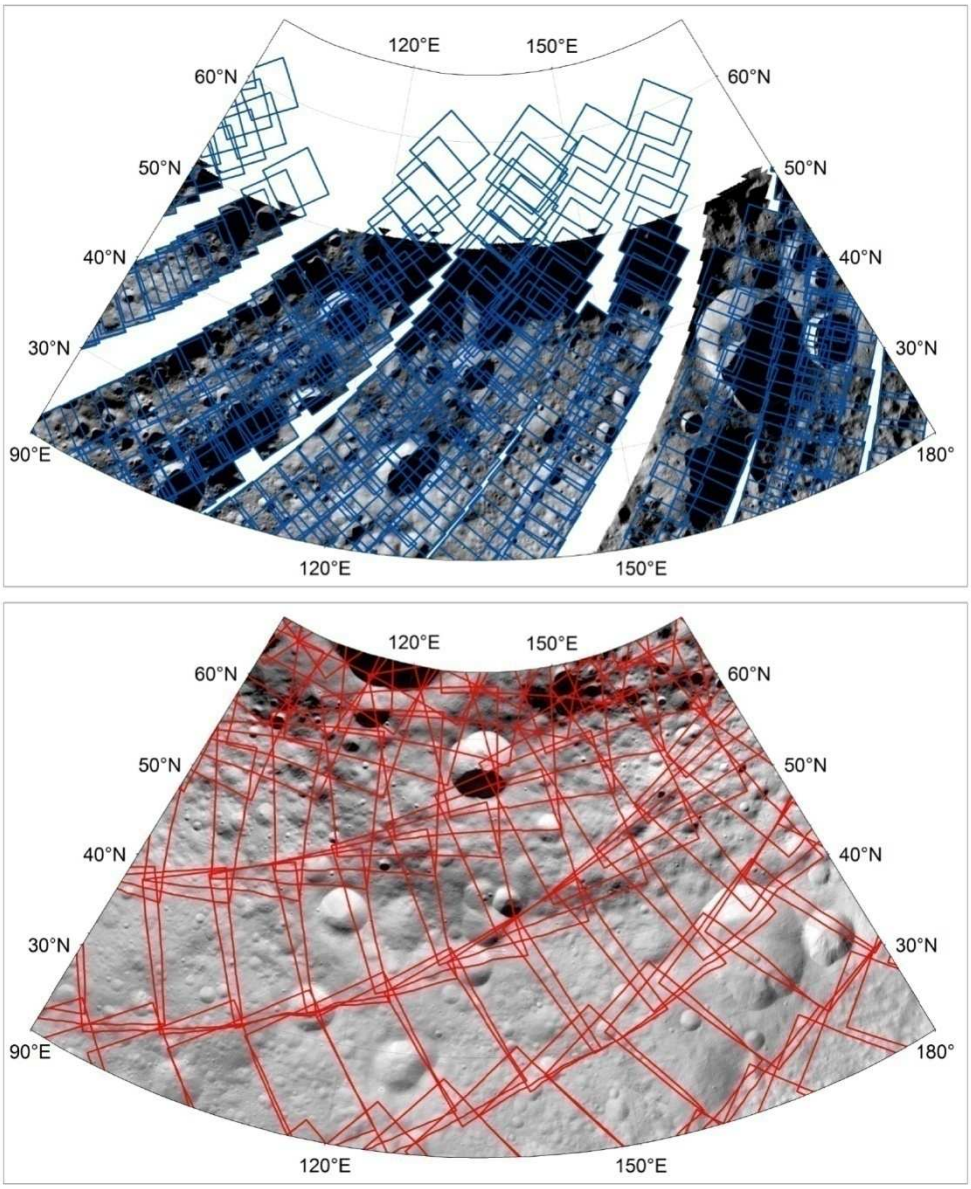

Figure 2.3 *Lambert conformal conic projection of a quadrangle of interest between 22°N-66°N and 90°E-180°E. Up: FC LAMO footprints in blue (only cycles 1 to 9 shown for clarity) overlaying a LAMO mosaic. Shadowed areas are present and the footprints coverage is not complete. Shadowed area northern of 50° not shown. Bottom: FC HAMO-2 footprints (only cycle 5 shown for clarity) in red overlaying a HAMO-2 mosaic. Note the absence of large shadowed areas and the complete coverage. The better spatial coverage is at the expense of the smaller spatial resolution, as the size of the single footprint suggests.(Footprints data from S.Walter, Freie Universität, Berlin).*

allowed for the detection of faint light reflected by nearby illuminated areas, enabling some scientific use (Ruesch et al., 2014b – Article III). Because of such differences in coverage and spatial resolution, a clear-filter mosaic was produced for each mission phase (Roatsch et al.,

2013). A given area of the surface was observed multiple times under different geometric conditions, as evident in Figure 2.3, allowing the application of the stereo-photogrammetry method to derive digital elevation models (DTMs) (Raymond et al., 2011; Jaumann et al., 2012). Such higher-level datasets were produced by the Deutsche Zentrum für Luft und Raumfahrt (DLR) (Jaumann et al., 2012; Roatsch et al., 2013).

As a consequence of the described differences in coverage, I chose to base the geological mapping (see Chapter 3.2) on the HAMO-2 mosaic. Nevertheless, the higher resolution LAMO images provide key observations, as have been revealed, for example for ejecta material (Ruesch et al., 2014b – Article III). Thus, LAMO images have been investigated where available.

2.3 Visible to near infrared spectrometer (VIR)

Reflectance data between 0.5 and 2.5 µm were derived from the Visible to near InfraRed mapping spectrometer VIR, managed by the Instituto Nazionale di Astrofisica (INAF) in Rome (De Sanctis et al., 2011). VIR uses a diffraction grating as dispersing element and two detectors to acquire a matrix for the visible (VIS) and infrared (IR) wavelength range. Nominal dimensions of the matrix are 256 pixels in the spatial dimension (samples) and 456 pixels in the spectral dimension (bands) (Figure 2.4). The 256 pixels in the spatial dimension constitute the so called slit. Spectral resolution is of 1.8 nm/band in the visible range (0.25-1.05 µm) and of 9.8 nm/band in the near-infrared range (1.0-5.0 µm). Each of the 256 pixels has an instantaneous field of view of 250 µrad, resulting in a pixel scale at the surface of 700 meter/pixel during Survey and 200 meter/pixel during HAMO. Observations of up to 67 % of the surface during Survey, were performed in pushbroom mode or with a scanning mirror as depicted in Figure 2.4 (De Sanctis et al., 2013). Pushbroom mode or scanning provided the additional spatial dimension (lines), to the two-dimensional matrix (samples and bands), creating a “cube” for each observation. An example of a VIR “cube” is shown in Figure 2.4.

The issue related to shadowed areas, as described for the FC, also applies for the VIR instrument. Because of the relatively lower sensitivity of the VIR IR detector, compared to the FC, artifacts appeared both within and up to few VIR pixels away from non-illuminated areas. The calibration of the instrument was performed for ideal nadir conditions and optimal signal (Ammannito et al., 2007). For extreme observation geometries and for shadowed areas, i.e., for data with lower signal, the calibration does not compensate known artifacts. Such artifacts are related to junction of order-sorting filters placed on the sensitive area of the detector

(Ruesch et al., 2014a – Article II). As a consequence, observations of the northern hemisphere were considered reliable only for the HAMO-2 phase, although Survey data for northern latitudes were also acquired. To exploit the latter data I developed a filter parameter to use during the data reduction pipeline (Ruesch et al., 2014a – Article II). Artifacts of lower importance are introduced by the inhomogeneity of the detectors´s slit and are referred to as stripes. In addition, spikes and even-odd artifacts, due to the detectors readouts, affect the spectral dimension (Ammannito et al., 2007).

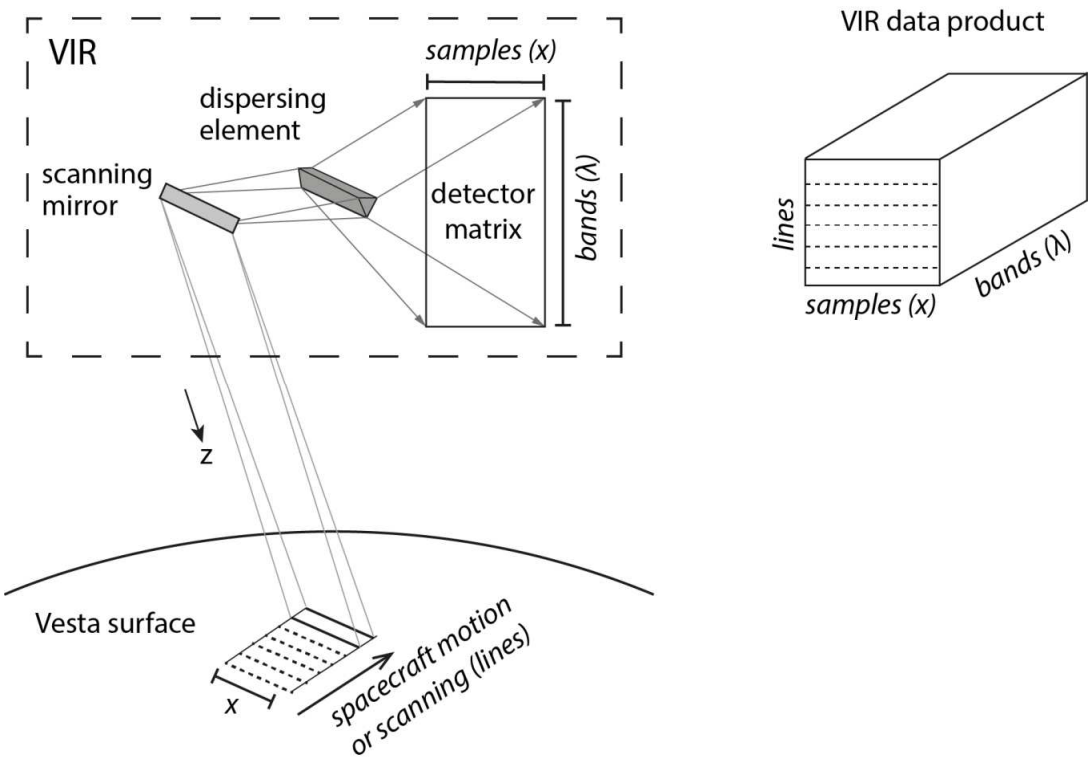

Figure 2.4 *Left: mode of observation of the VIR instrument and relation between the two spatial dimensions (samples and lines) and one spectral dimension (bands). Direction of observation is indicated by the z arrow. Right: scheme of a VIR hyperspectral cube.*

These artifacts affect a narrow range of wavelengths (<0.1 µm) and have no direct influence on the overall shape of the spectra, which is used for mineralogical investigations (see Chapter 3.5.2). A factor that controls the overall shape of the VIR spectra is the Instrument Transfer Function (ITF) (shown in Figure 3.4). To overcome uncertainties on the accuracy of the ITF (which affect all the spectra acquired in nominal condition in the same way), it is useful to analyze VIR spectra relative to each other and discern relative variations to avoid misinterpretation.

2.4 Gammay ray and neutron detector (GRaND)

The third instrument of Dawn, the gamma ray and neutron detector (GRaND) takes advantages of cosmogenic nuclear reactions and radioactive decay at depths of up to a few decimeters from Vesta´s surface to determine elemental abundance distributions (Prettyman et al., 2011). The iron abundance map (Yamashita et al., 2013) was used in this thesis as a complementary dataset (Ruesch et al., 2015 – Article I) and its derivation is briefly presented here. GRaND sensors acquired gamma-rays spectra (in counts/s/keV) with characteristic gamma-ray peaks produced by Fe thermal neutron capture reactions. First, the background signal due to gamma rays and other photons was subtracted from the Fe peak areas, to obtain the Fe counting rate (Yamashita et al., 2013). Subsequently, corrections to the Fe counting rate were applied for live times, variations in the intensity of galactic cosmic rays, and most importantly, for the solid angle of observation. Because the Fe counting rate is proportional to the Fe abundance *and* the number density of neutron, a correction is necessary to obtain the Fe abundance only. The neutron number density is estimated by taking into account the effects of neutron absorption (e.g., Fe, Ca, Al, Ti) and hydrogen abundances (Prettyman et al., 2013). The produced map is imported into a geographic information system (GIS) described in section 3.1

2.5 HED meteorites samples

Howardites, eucrites, and diogenites (HED) are differentiated achondrite meteorites and represent a single group of meteorites due to their similar texture, mineralogy, oxygen isotopic ratios, Fe/Mn elemental ratios, and petrological relationships (e.g., Clayton and Mayeda, 1983; Mittlefehldt et al., 2004; Hutchison, 2004). The HED parent body probably formed very early in the Solar System, with a core formation and silicate differentiation occurring within the first ~5 Myr after CAI condensation (Kleine et al., 2002).

Most diogenites are monomict, fragmental breccias of original coarse-grained En_{72-77} orthopyroxenites (e.g., Mittlefehldt et al., 2004). Olivine (Fo_{61-78}, Beck and McSween, 2010; Shearer et al., 2010) can be occasionally present in high abundances (e.g., Beck et al., 2012). Troilite, metal and silica are accessory phases, as well as chromite, Ca-rich pyroxene and plagioclase (e.g., Hutchison, 2004). It is relatively well established that a single process during the magmatic activity of the early HED parent body was responsible for the formation of orthopyroxenite diogenites and olivine-rich (harzburgitic, Figure 2.6) and olivine-dominated (dunitic) diogenites, but the exact process is still debated (e.g., Shearer, et al., 2010). Diogenites and olivine diogenites could represent plutons or different horizons in

layered intrusions within the HED parent body (Fowler et al., 1995; Shearer et al., 1997 ; Mittlefehldt, 2000, Shearer et al., 2010; Beck and McSween, 2010). The magmas would have been derived from batches of the HED body mantle (Shearer et al., 2010). Alternatively, the lithologies could have been produced during the crystallization of a magma ocean (Warren, 1985; 1997; Righter and Drage, 1997 ; Ruzicka et al., 1997, Gosh and McSween, 1998).

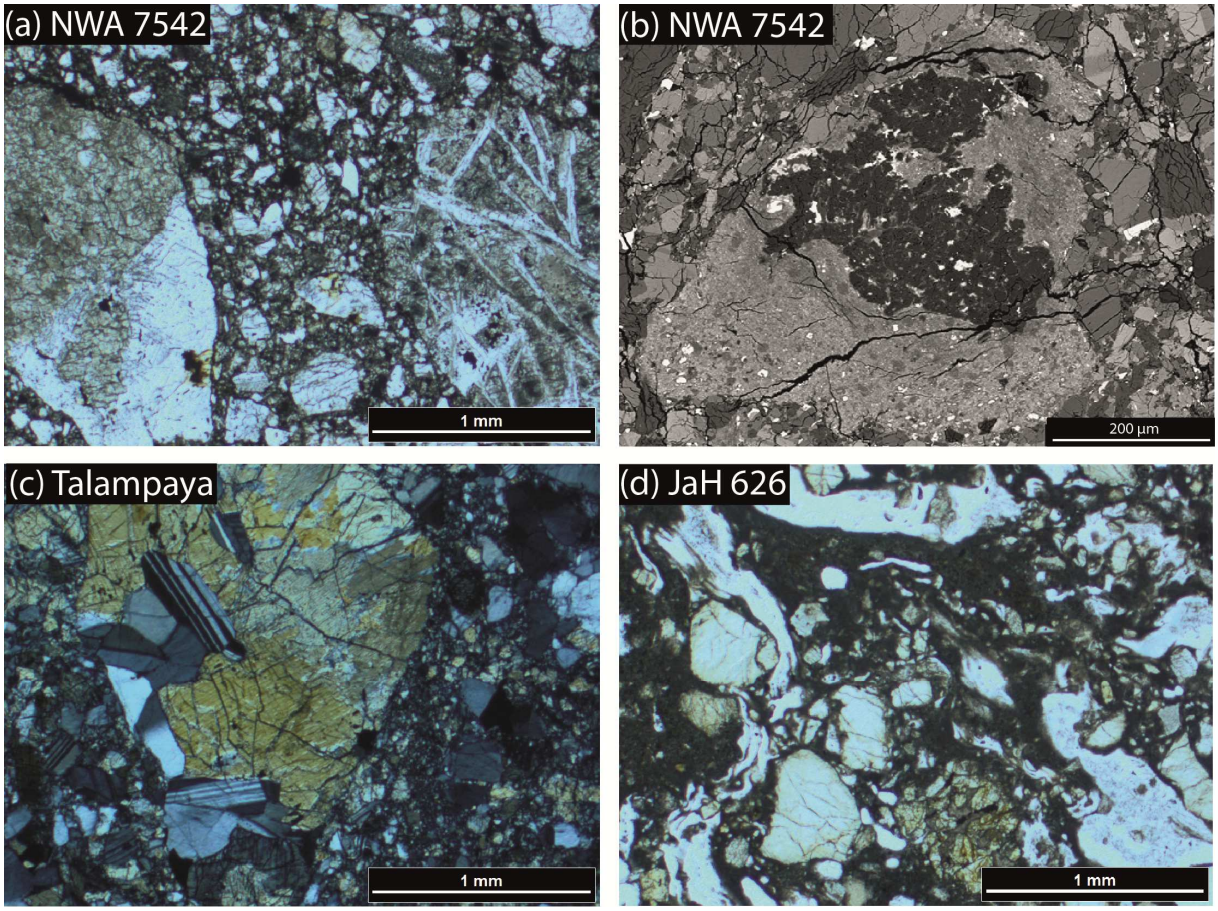

Figure 2.5 *(a) Transmitted light of a polymict eucrite in thin section showing diogenitic and eucritic clasts. (b) SEM-BSE image (from K. Metzler) of a carbonaceous chondrite clast in NWA 7542 consisting of an olivine chondrule fragment (dark) embedded in a fine-grained interchondrule matrix. (c) Polarized light of a thin section showing a cumulate eucrite with large pyroxene grains with exsolution lamellae. (d) Transmitted light image showing an uncommon eucrite consisting of an impact melt rock with vesicular melt and plagioclase with fluidal texture.*

Eucrite meteorites are found in a variety of textures: basaltic, cumulate, monomict breccia and polymict breccia (see McSween et al., 2011 for a review). The major minerals are An_{75-95} plagioclase and pigeonite, often with exsolution lamellae of augite. Minor minerals are silica, ilmenite, chromite, troilite and metals (e.g., Hutchison, 2004). Most eucrites are

equilibrated through thermal metamorphism with augite lamellae in a host homogeneous pigeonite (e.g., Takeda and Graham, 1991; Yamaguchi et al., 1996). Clouding is observed in their pyroxene and plagioclase phases, consisting of precipitated sub micrometer-scale opaques minerals (Harlow and Klimentidis, 1980). Inversion of pigeonite to orthopyroxene is observed for the most equilibrated eucrites, with a narrow range of Mg/(Mg+Fe) and a wide range of Ca/(Ca+Fe). Most eucrites also experienced shock, brecciation and melting events (e.g., Metzler et al., 1995). Unequilibrated eucrites show chemical zoning of pyroxene and have a wide range of Mg/(Mg+Fe). Cumulate eucrite have intermediate Mg/(Mg+Fe) values between diogenites and non-cumulate eucrites (e.g., Hutchison, 2004).

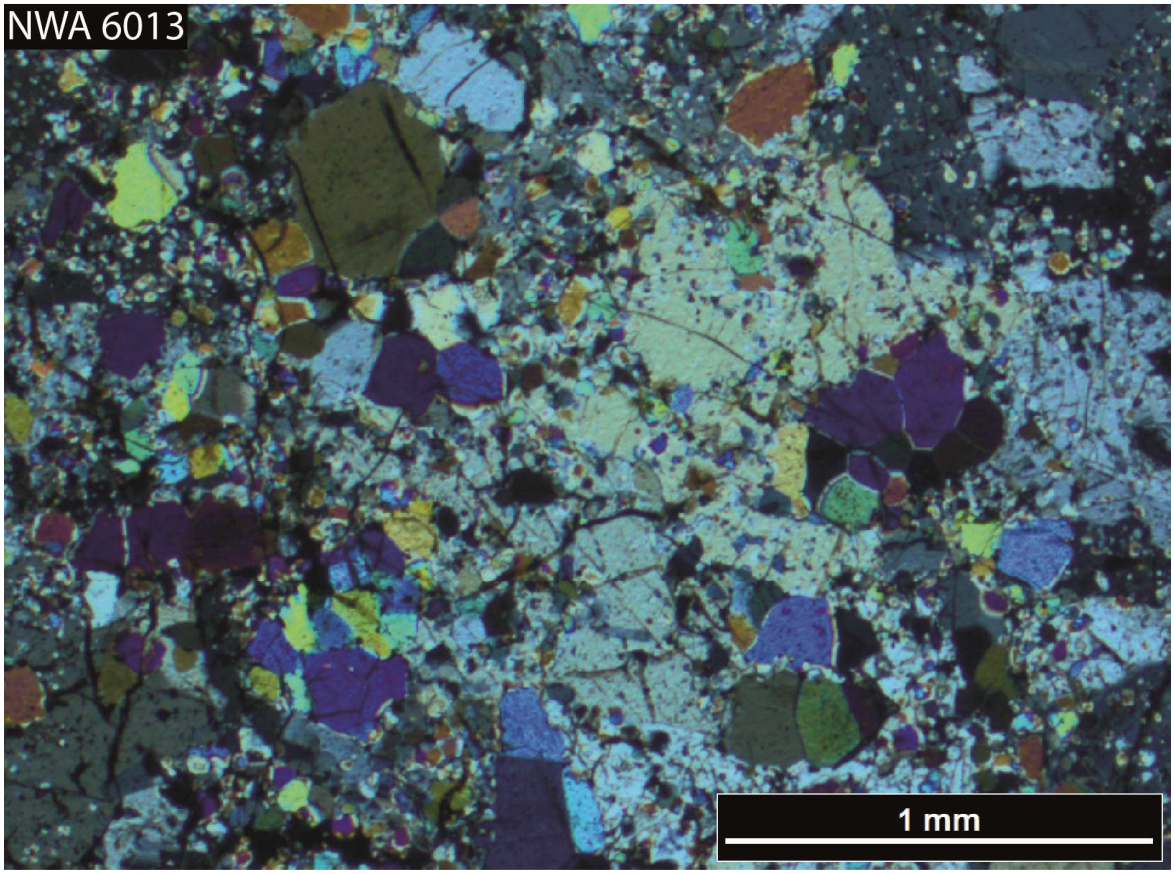

Figure 2.6 *NWA 6013 (in polarized light) is a relatively uncommon olivine-bearing diogenite. Olivine grains (average Fo_{74}) have a bimodal size distribution.*

Howardites are breccia with more than 10 vol% of eucrites (ophitic to subophitic basalt clasts, granulite clasts) and 10 vol% of diogenites (pyroxene fragments), set in a fine-grained clastic matrix. Impact rock clasts and impact melt droplets can occur (e.g., Ruesch et al., 2015 – Article I). Of interest for Vesta are rare carbonaceous chondrite clasts, as in the polymict eucrite NWA 7542 shown in Figure 2.5 (e.g., Zolensky et al., 1996). Often of the CM type, the clasts have a phyllosilicate (mostly serpentine) rich matrix, which is responsible for

hydrous absorption bands in the near-infrared spectral range (Cloutis et al., 2011). With Dawn observations, these absorption bands have been identified locally on Vesta (McCord et al., 2012; Reddy et al., 2012; Nathues et al., 2014). The nature of howardites implies that both eucrites and diogenites formed on the same body and underwent brecciation, mixing and thermal metamorphism within the parent body regolith (e.g., Metzler et al., 1995; Bischoff et al., 2006).

At the Institut für Planetologie of the Westfälische Wilhelms-Universität Münster I studied a total of 13 eucrites, 6 howardites and 5 diogenites.

3. Methods

3.1 Image data processing and visualization

Since digital image data were acquired by spacecraft, a reliable system for their cartographic and scientific analyses was needed. The United States Geological Survey (USGS) developed and maintains the Integrated System for Imagers and Spectrometers (ISIS) that enables researchers to geometrically rectify and calibrate planetary images and spectrometer data, as well as to apply post-processing procedures, for example, to generate image mosaics (e.g., Anderson et al., 2011).

Raw images, also referred as Experimental Data Record (EDR) are usually in a standard format consisting of a file containing the data and an attached or detached label containing a description of the data (Planetary Data System or PDS format). The calibration of Dawn FC images and VIR cubes requires several steps, the most important being dark current subtraction and flat field division (e.g., Sierks et al., 2011; De Sanctis et al., 2011). Eventually, a Radiance Data Record (RDR) product is obtained by converting the DN (digital numbers) values into radiometric units. Navigation and ancillary data such as spacecraft position, pointing, body shape and orientation, and Sun position are stored in SPICE (Spacecraft Planet Instrument Camera-matrix Events) kernels. Ground position (i.e., latitude/longitude) and photometric viewing angles of an image can be computed with ISIS using such kernels. Images with known ground position can be map projected and mosaics can be constructed. All these processes were applied to the FC images by the DLR (Roatsch et al., 2012; 2013). I processed the VIR data using ISIS starting from the RDR format, as detailed in section 3.5.4.

The higher-level products were then further investigated with several software packages, discussed below. The transfer was done directly from ISIS to a Geographic Information System (GIS) or through interface packages such as the ISIS DLM system for transferring ISIS data to the Interactive Data Language (IDL) system.

For the purpose of photo-geological mapping and absolute model age determination, ArcGIS provided by the Environmental Systems Research Institute (ESRI) was used. The software allows the visualization and superposition of different raster products in a common map projection. The image products ingested into ArcGIS were FC clear filter and color images and mosaics, VIR mineralogic maps, GRaND elemental maps, and digital elevation models. In the ArcGIS environment, several processing steps (e.g., stretching) and spatial

inquiries (i.e., pixel values) can be performed on the raster data. In addition, vector data can be used for the production of photo-geological maps (e.g., Nass et al., 2011).

3.2 Photo-geological Mapping

A morphological map of a planetary surface contains information on relevant surface units, linear features and stratigraphy (e.g., Wilhelms et al., 1990). It is based on the interpretation of surface textures (e.g., roughness) and topographic reliefs to identify three-dimensional material units (e.g., Tanaka et al., 2009). The study of cross-cutting relationships and surface dating by CSFD measurements provide time-stratigraphic relationships between the units. For the purpose of mapping by the Dawn Science Team, the surface of Vesta was subdivided into 15 quadrangles following the scheme of Greeley and Batson (1990) and named Av-1 through Av-15 (Figure 3.1). In Ruesch et al. (2014b) – Article III, I mapped Av-1 to Av-5 located in the northern hemisphere, i.e., covering the latitudes from 21°N to the North Pole. For quadrangle Av-1, the imaging data were projected in a polar stereographic map, whereas for quadrangles Av-2 to 5 a Lambert projection was chosen (e.g., Snyder, 1987). The scale for the northern hemisphere was 250,000. The geologic units were outlined in vector polygones in association with raster products in the ArcMap environment of ArcGIS. The first step in mapping consisted in the definition of geological contacts. Usually, a gradational contact was

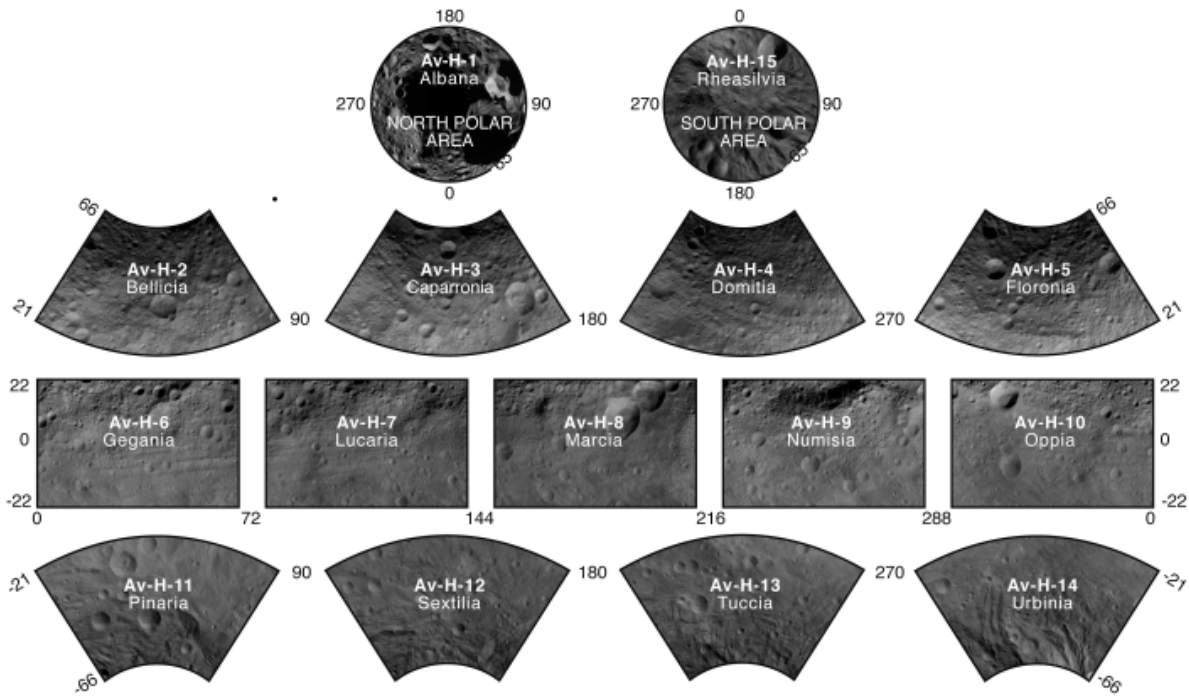

Figure 3.1 *The Vesta mapping quadrangles with quadrangle numbers and official IAU names (Roatsch et al., 2013).*

defined for ejecta material, whereas an approximate contact was used for tectonically altered terrains. Geologic units were defined, once all the geologic contacts were identified. Spatial inquiries between the vector (e.g., polylines and polygones) and the raster data (e.g., FC mosaic), as well as extraction of topographical profiles from DTM, were performed within the ArcMap environment. The Small Body Mapping Tool was used for the visualization of the DTM (Kahn et al., 2011).

3.3 Absolute Model Age determination of surface units

Like many planetary surfaces, Vesta´s surface is subject to the bombardment by small bodies, mostly asteroids. In the absence of geological processes that obliterate impact craters, a surface unit accumulates craters with time (e.g., Neukum, 1983). Thus, the amount of craters within a given surface unit (density) is related to the formation or exposure time of the unit and the impact rate (e.g., Hartmann, 1966). This is valid for any range of crater diameters (e.g., Neukum, 1983). The crater density versus crater diameter range is referred to as the Production Function (PF) (Neukum, 1983). Neukum (1983) established that for any planetary surface in the inner Solar System or in the main belt the PF is controlled by an impactor population with a certain size-frequency distribution (SFD). This assessment is based on the high similarity between the SFD of the lunar and Mars impactors and the Near Earth Asteroids SFD (e.g., Neukum, 1983; Neukum et al., 2001; Werner, 2005). The determination of the impactor population can be calculated using several lunar areas of different ages (Neukum, 1983). First, the crater size-frequency distribution (CSFD) of the areas is determined. Then, the crater diameters are converted to projectile (impactor) size using impact scaling laws. The scaling laws use reasonable assumptions on the target and projectile properties (density), impactor velocity, and strength to gravity transition (Ivanov, 2001; Schmedemann et al., 2014 – Article IX). After conversion, a lunar projectile SFD for each area is obtained. After normalization of the projectile SFDs of different areas, a single SFD of the lunar impactor population is obtained (Neukum, 1983).

The work by Schmedemann et al. (2014) – Article IX follows the approach first established by Neukum (1983) for the terrestrial planets and considers that the impactor population on Vesta is represented by the impactor population in the inner Solar System, i.e., the lunar impactor population. Following this assumption, the SFD of the lunar impactor population was converted into the SFD of projectiles on Vesta (Schmedemann et al., 2014 – Article IX). Scaling laws are used to convert projectile sizes into crater diameters on Vesta.

The PF of Vesta gives the cumulative number of craters of diameters larger or equal than D (in km), formed on a square km area exposed to the projectile bombardment for a given time:

$$log(N_{cum}) = a_0 + \sum_{k=1}^{11} a_k \, log(D)^k \quad (1)$$

the coefficients a_k are:

Coefficient	Vesta rev3 (Schmedemann et al., 2014 – Article IX)
a_0	-3.1643
a_1	-3.0382
a_2	0.5445
a_3	0.67305
a_4	0.11447
a_5	-0.34186
a_6	-0.15077
a_7	0.079115
a_8	0.035557
a_9	-0.0099727
a_{10}	-0.002574
a_{11}	0.00058434

The coefficient a_0 is a function of the time of exposure and is given by:

$$a_0 = \log(\mathrm{N}_{cum}(D \geq 1\ km)) \quad (2)$$

where $\mathrm{N}_{cum}(D \geq 1\ km)$, the cumulative number of craters of diameter larger or equal 1 km, also referred to as N(1), is given by:

$$\mathrm{N}_{cum}(D \geq 1\ km) = \mathrm{k}_1 r\ (e^{k_2 t} - 1) + \mathrm{k}_3 t \quad (3)$$

Where t is the surface exposure age in [Ga] measured backwards from the present. Equation (3) is called the Vesta chronology function (CF) and is defined using the same time dependence as for the moon. k_1 in equation (3) is equal to k_1 of the lunar chronology, derived empirically (see below). r is the ratio of the current crater formation rate on Vesta to the rate on the Moon: $r = \frac{k_{3\ vesta}}{k_{3\ moon}}$. The factor k_2 describes the rate of the exponential decay of collisions during the first ~1 Ga of Solar System history: it is a constant (k_2 = 6.93) valid for all chronology functions. For t lower than ~3 Ga, the rate of collisions is constant and is given

by k_3 (k_3=0.02037), using the intrinsic collision probability and the number of available projectiles (O'Brien and Greenberg, 2005; Bottke et al., 1994).

The lunar chronology function (and k_1) can be defined by (i) relating radiometrically dated lunar samples to their geological unit, and (ii) measuring the N(1) of the surface of the geological unit. The definitive relation of a dated sample to its lunar geological unit is not straightforward, especially in the case of ejecta samples (e.g., Stöffler and Ryder, 2001). Thus, several chronology functions have been proposed (e.g., Stöffler and Ryder, 2001). The CF given in equation (3) was derived by Neukum (1983) using a least square fit between the absolute ages of radiometrically dated samples and the measured N(1) of potential lunar source region.

The derivation of absolute model ages on Vesta requires the above described production and chronology functions and CSFD measurement on a given area. The area must be within a geologic unit, have homogeneous texture and be free of crater clusters formed by secondaries. A specifically developed software presented in Kneissl et al. (2011) is used within the ArcGIS software to perform the diameter measurement of each crater. The CSFD measurement is binned and displayed in a logarithmic plot (Arvidson et al., 1979). The PF is fitted to the CSFD measurements by varying the a_0 coefficient. Although the fit needs to include the highest possible number of bins, small diameter bins influenced by secondary cratering or resurfacing needs to be avoided. If there is morphologic evidence for one (or more) resurfacing event, two (or more) PF might be fitted to the CSFD measurements. Once a satisfying fit is achieved, equation (3) is solved for t with the a_0 of the fitted PF. A stochastic age error on N(1) is used to evaluate differences between different unit ages derived with the same PF and CF. It is calculated from the measured counting statistics:

$$\sigma = \pm N_{cum} * \frac{1}{\sqrt{n}} \tag{4}$$

Where n is total number of craters used for the fit (Arvidson et al., 1979; Michael and Neukum, 2010).

It has been argued that the dynamical history that delivers impactors to the inner Solar System (NEA) is different from the collisional history of bodies within the main belt (e.g., O'Brien et al., 2014). Also, the SFD of the inner Solar System might have changed early in the history of the Solar System (at around ~3.8 Ga), contrary to the assumption by Neukum (1983) (e.g., Wilhelms et al., 1978; Strom et al., 2005; Head et al., 2010; O'Brien et al., 2014). Thus, alternatives approaches to the above described method considered the dynamical history of the asteroid belt to determine the SFD of the impactors and the impact rate versus

time relationship on Vesta (O'Brien et al., 2014). Details on an alternative dynamical-based approach can be found in O'Brien et al. (2014) and Marchi et al. (2012). In Ruesch et al. (2014b) – Article III the alternative approach was tested revealing, however, inconsistencies between the measured CSFD and the dynamical-based SFD.

3.4 Electron Probe Microanalyses

Electron probe microanalyses were performed to determine the chemical compositions of minerals in HED samples. This analytical method is based on diagnostic x-ray spectra emitted by elements (e.g., Reed, 1993; Nesse, 1998). Electrons are usually produced by a heated tungsten filament. Through electromagnetic fields, electrons are focused on the sample, usually a carbon coated thin section. When the electron beam strikes the samples, x-rays are emitted with a spectrum consisting of a continuum and characteristic peaks. The latter are produced by the emission of radiation following the replacement of a dislodged electron in the shells of the atoms. The energy, i.e., wavelength, of the radiation is equal to the energy difference between the outer shell and the K shell of the atom (e.g., Reed, 1993), and the radiation intensity is proportional to the amount of a given element present in the sample. In the microprobe, the x-rays are measured by a wavelength dispersive spectrometer (WDS) based on crystals (e.g., Zachariasen, 1967). To derive the absolute abundance of an element with peak intensities, the instrument response is calibrated using minerals standards of well know composition. Following the technique of Philibert and Tixier (1968), for each element, the specimen/standard detector counts (i.e., intensity) ratio ("k-ratio") multiplied by the concentration of the element in the standard is calculated. Then, a matrix correction is applied to the k-ratio to obtain the absolute concentration of a given element. The matrix correction takes into account additional processes occurring during x-ray production, such as backscattered electrons, enhancement (fluorescence) and absorption of x-ray, and the efficiency in the production of x-rays (Philibert and Tixier, 1968). With these corrections, it is possible to measure the abundance of elements with an uncertainty of about 0.1-0.01 wt% (e.g., Reed, 1993).

For this study, I used a microprobe JEOL JXA 8900 of the Interdisziplinäres Centrum für Elektronen mikroskopie und Mikroanalyse (ICEM) of the Westfälische-Wilhelm Universität Münster.

3.5 Reflectance spectroscopy

3.5.1 Near infrared reflectance spectra

Usually, remote sensing reflectance spectra consist of bidirectional diffuse reflectance and can be defined with the angles incidence (i), emission (e) and phase angle (α) as follow. If a surface receives an incident collimated radiant power per unit area $J\mu_0$ with J the irradiance [W m^{-2} sr^{-1}] and $\mu_0 = cos(i)$, the scattered radiance of the surface measured by a detector is $Jr(i, e, \alpha)$ with $r(i, e, \alpha)$ the *bidirectional reflectance*. The *Bidirectional Reflectance Distribution Function* is defined as $BRDF(i, e, \alpha) = \frac{Jr(i,e,\alpha)}{J\mu 0}$ with units [str^{-1}] (Hapke, 2012). For clarity, the spectral dependence on each parameter is omitted. Usually, reflectance data are expressed as *radiance factor (I/F)*, i.e., the ratio of the bidirectional reflectance of a surface $r(i, e, \alpha)$ to that of a perfectly diffuse surface (Lambert) illuminated at i=0 (Hapke, 2012). The bidirectional reflectance of a Lambertian surface is expressed as $r_L = A_L * \mu_0/\pi$ (Hapke, 2012). A_L is the direction-hemispherical reflectance and is equal to 1 for a perfectly diffuse surface (Hapke, 2012).

$$I/F = RADF(i, e, \alpha) = \pi\, r(i, e, \alpha) \tag{5}$$

In the literature it is often referred to the *reflectance factor*, denoted here as REFF i.e., the ratio of the bidirectional reflectance of a surface to that of a perfectly diffuse surface under the same illumination conditions (Hapke, 2012).

$$REFF(i, e, \alpha) = \pi\, r(i, e, \alpha)/\mu_0 \tag{6}$$

The reflectance spectra in this work are expressed with this latter parameter. Several mathematical models have been developed to express the bidirectional reflectance in physical terms of the surface (e.g., Hapke, 1981; Douté and Schmitt, 1998, Shkuratov et al., 1999; Shkuratov et al., 2011). They are partly based on the radiative transfer equation that governs the radiation field through a medium which absorbs, emits and scatter radiation (Chandrasekhar, 1960).

Here, the physical factors controlling the bidirectional reflectance are described. These factors are fully or partly taken into account by current models for particulate surfaces (e.g., Hapke, 1981; Douté and Schmitt, 1998, Shkuratv et al., 1999). The intrinsic properties of a surface material (independent on particle size and shape) are described by the optical constants or complex refraction index (e.g., Bohren and Huffman, 1983). They are the principal factor controlling the spectral features of mafic material in the near-infrared range

(e.g., Bohren and Huffman, 1983; Lucey, 1998) and their physical origin is described in section 3.5.2. The influence of particle size on reflectance spectra is described by radiative models (e.g., Hapke, 1981; Shkuratov et al., 1999) and a detailed experimental study of grain size variations on HED near-infrared spectra was presented in Cloutis et al. (2013). It is known experimentally that the geometry conditions influence a reflectance spectrum through phase reddening, i.e., stronger absorption at shorter wavelengths compared to longer wavelengths and resulting increase in spectral slope (e.g., Adams and Filice, 1967; Gradie et al., 1980; Reddy et al., 2011; Schröder et al., 2014; Ruesch et al., 2015 – Article I). Geometric conditions also influence absorption bands (e.g., Gradie et al., 1980, Reddy et al., 2011; Ruesch et al., 2015 – Article I). The radiative transfer model proposed by Hapke (1981; 2012) explains such effects by the varying contributions of single and multiple scattering (e.g., Hapke, 2012). However, alternative explanations have been proposed (e.g., Schröder et al., 2014). As a consequence of the still ambiguous origin of such effects, and in order to quantify the spectral variations due to geometry effects, part of this thesis focuses on laboratory measurements of HED samples under varying geometric conditions (Ruesch et al., 2015 – Article I). Temperature effects, although known to contribute to a spectrum shape (e.g., Burns, 1993; Moroz et al., 2000; Burbine et al., 2009) are minor for the range of temperatures during Vesta VIR observations (Longobardo et al., 2014). The exact influence of additional factors, such as porosity and roughness, is poorly understood by current radiative transfer models but is known to affect particulate reflectance spectra (e.g., Adams and Filice, 1967; Capaccioni et al., 1990; Shepard and Helfenstein, 2007; Hapke, 2008). Finally, if the grains of a particulate surface have different compositions (e.g., pyroxene, feldspar); their mixture will influence the reflectance spectra with a nonlinear function (e.g., Nash and Conel, 1974; Singer, 1981; Hapke, 1981; Mustard and Pieters, 1989; Poulet et al., 2014 – Article IV). On Vesta, the mixture occurs at a sub-pixel scale, i.e., below the spatial resolution of the observation (e.g., Poulet et al., 2014 – Article IV), usually at a kilometer scale for VIR observations (De Sanctis et al., 2011). The mixture can be considered “intimate”, i.e., photons encounter grains of different composition before escaping the surface and reaching the detector (e.g., Hapke, 1981). In addition, the grains are possibly not homogeneous, but present compositional variations at a sub-grain scale (e.g., inclusions).

3.5.2 Absorption bands

As detailed above, the position, width and strength of absorption bands in a spectrum are diagnostic of the chemical, mineralogical and physical properties of the target surface (e.g.,

Clark, 1999). The mechanisms of absorption are electronic transitions, molecular rotation, and lattice vibration (e.g., Burns, 1993; Hapke, 2012). In the near-infrared range, electronic transitions are important and are presented here. Molecular vibrations are responsible for bands in the mid-infrared range (e.g., Burns, 1993; Hapke, 2012).

Charge transfer absorption is an electronic transition occurring when electrons transfer between ions. The resulting band centers usually occur in the ultraviolet, with the wings of the absorption extending into the visible range (Clark, 1999). C*rystal-field* absorption of an incident photon is enabled by electronic transitions from a lower to a higher energy level (Burns, 1993). In transition elements the energy separation between orbital levels is termed crystal-field splitting parameter (Δ_o) and for cation-oxygen transitions is inversely proportional to the cation-oxygen interatomic distance (r). In an octahedral framework of oxygen atom the *d*-orbital energy levels of Fe^{2+} are splitted into e_g and t_{2g} orbitals (Figure 3.2). Depending on the geometry (e.g., distortion) of the octahedral sites M1 and M2, further splitting occurs (e.g., Burns, 1993). The Δ_o between the energy levels can also be represented as wavenumber (cm^{-1}), and controls the positions of absorption bands. Thus, the structure or geometry of the crystallographic site hosting the transition elements (e.g., Fe^{2+} in olivine or pyroxene) is directly influencing the crystal-field splitting parameter and thus the absorption (e.g., Burns 1993; Klima et al. 2007, 2011). The variability of the M1 and M2 crystallographic sites of pyroxenes and its implications are explained below.

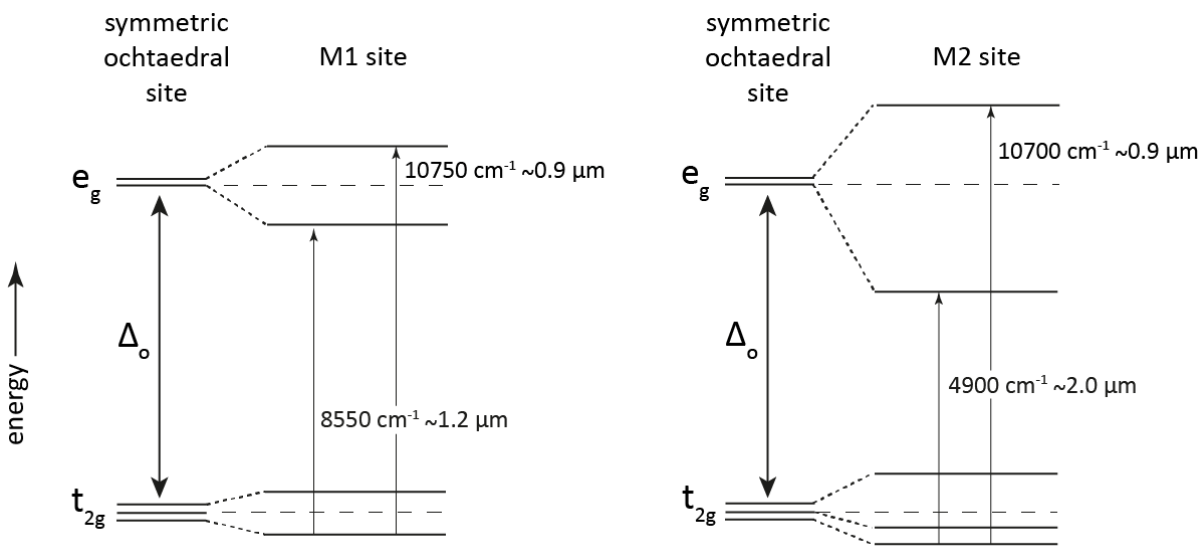

Figure 3.2 *Energy level diagrams for the 3d orbitals of Fe^{2+} in orthopyroxene. The slightly distorted crystallographic M1 site and the strongly distorted M2 site are shown together with orbital splitting in regular octahedral sites. Main electronic transitions and their corresponding wavelengths are indicated (adapted from Burns, 1993).*

The M1 crystallographic site in pyroxenes corresponds to a relatively symmetric octahedral site and usually hosts the following cations: Mg^{2+}, Fe^{2+}, Mn^{2+}. As illustrated in Figure 3.2, Fe^{2+} in the M1 site creates crystal-field absorptions at ~0.9 µm and ~1.2 µm. With increasing abundance of the larger Fe^{2+} cation by replacement of the smaller Mg^{2+} in ortophyroxene, the crystal-field splitting parameter decrease ($\Delta_o \alpha r^{-5}$), and the wavelength position of the ~0.9 µm band slightly increase (Bums, 1993). Usually, however, the band at 0.9 µm is masked by the stronger crystal-field absorption due to Fe^{2+} in the M2 site (Burns, 1993). The stronger bands due to Fe^{2+} in the M2 site are the results of the larger and highly distorted polyhedral site that enables substantial crystal-field splitting (e.g., Burns, 1993; Denevi et al., 2007; Klima et al., 2007; 2011). The M2 crystallographic site hosts Mg^{2+}, Fe^{2+}, Mn^{2+} and Ca^{2+} (e.g., Adams, 1974; Burns, 1993). Note that although the M2 site can host several cations, it is preferentially filled by Fe^{2+} in the absence of Ca^{2+}. Main bands are located at ~0.9 µm and ~2.0 µm and are responsible for the characteristic bands of pyroxenes (Burns, 1993). With increasing Ca^{2+} in the crystals, the M2 site increases in size. As a result, the crystal field splitting parameter decreases, and the ~1 and ~2 µm bands created by Fe^{2+}slightly shift to longer wavelengths (e.g., Hazen et al., 1978; Burns, 1993).

3.5.3 VERTEX 70v reflectance spectra

For laboratory measurements of reflectance spectra, I operated a fourier transform spectrometer VERTEX 70v hosted at the IR/IS Laboratory of the Institut für Planetologie of the Westfälische Wilhelms-Universität Münster. In the VERTEX 70v, an interferometer unit with exchangeable beam splitters allows a range of wavelengths to be measured near-simultaneously (e.g., King et al., 2004). Raw data consists of an interferogram, i.e., an intensity (voltage) versus retardation (optical path difference) spectrum. A fourier transform is then applied for conversion to the frequency domain and for obtaining an intensity versus energy (wavelength) spectrum (Figure 3.3) (e.g., King et al., 2004). For the range 0.7 to 2.0 µm (NIR) a DigiTect InGaAs detector operating at room temperature and a Tungsten light source were used. Whereas for the range 2 to 16 µm (MIR) a DigiTect HgCdTe (MCT) detector cooled with liquid nitrogen and a Globar thermal source were employed (Bruker Optics). A Spectralon standard for the NIR range and an Infragold standard for the MIR range were provided by the Labsphere company. The vendor provided a correction factor for the Spectralon in the range 0.7-2.0 µm. This correction factor *C* (with values higher than 0.93) is wavelength dependent (Labsphere report, 2014).

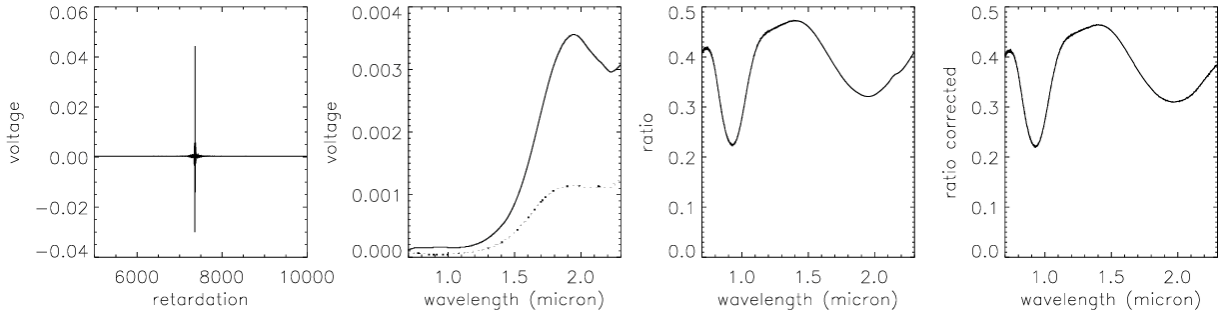

Figure 3.3 *Retrieval of reflectance spectra from the VERTEX 70v spectrometer. From left to right: interferogram of a sample, spectrum as a function of wavelength for a sample (dashed line) and a standard (continuous line), sample to standard ratio, ratio corrected using factor C described in the text (note the removal of a bump at 2.15 µm).*

To simulate the particulate surface of Vesta's soil, the samples were powdered and dry sieved at 4 different particle size: 500-250 µm, 250-90 µm, 90-45 µm and 45-0 µm. The latter grain size range is most similar to the average Vesta surface (e.g., Hiroi et al., 1994). As described above, a reflectance spectrum is also a function of the geometry of observation, i.e., incidence, emission and phase angles. A Bruker A513/Q goniometer was used to vary the incidence and emission angles independently. The arms of the goniometer move only in one plane, without variation of the azimuth angle. This means that all the measurement were performed on the principal plane, no azimuth variations. Due to mechanical constraints, the smallest incidence and emission angles allowed are 13° for both angles. The light source aperture diameter was set at 4 mm, leading to a ellipse of 8.3x7.2 mm illuminating the circular sample cup of 10 mm diameter (for an incidence angle of 30°). This setup enables enough light at the detector but prevents illumination of the aluminum cup. All measurements were performed in low pressure environment (10^{-3} bar) to avoid absorption bands due to water vapor.

If the detector measures a voltage $V(i, e, \alpha)$ in the near-infrared, and if it is assumed that $V_{standard}(i, e, \alpha)$ results from a perfectly reflecting diffuser, the reflectance factor can be calculated as:

$$\mathrm{REFF}(\mathrm{i}, \mathrm{e}, \alpha) = \frac{V_{sample}(i,e,\alpha)}{V_{standard}(i,e,\alpha)}\, C \qquad (7)$$

This is illustrated in Figure 3.3. However, calibration standards are known to deviate from perfect Lambertian behavior, (e.g., Pieters, 1983; Mustard and Pieters, 1989; Bonnefoy et al.,

2000). Alternative methods to retrieve the reflectance factor are described in Pommerol et al. (2011) and Gunderson et al. (2007). The principle of reciprocity states that for a uniform surface without inhomogeneity, illuminated by light from a collimated source, the following relation must be satisfied: $REFF(i, e, \alpha) = REFF(e, i, \alpha)$ (Hapke, 2012). This test provides a robust method to estimate the uncertainties of the measurements, related to instrumental errors and to the inhomogeneity of the sample (e.g., Pommerol et al, 2013). The standard deviation over the entire spectral range is less than 1% with larger errors in the range 0.7-1.2 µm compared to the 1.2-2.5 µm range.

3.5.4 VIR reflectance spectra

Here, the specific data reduction and calibration of the VIR dataset is laid out. A more general description is given in section 3.1. An in-depth presentation of the VIR instrument, data reduction and calibration can be found in De Sanctis et al. (2011), in Ammannito (2007), in Filacchione and Ammannito (2011), in Filacchione (2006), as well as in Capria and Joy (2011).

The level 1a or EDR of the VIR data consist of spectra expressed in digital number (DN). The first steps in the calibration pipeline consist in the subtraction of the dark current and identification of anomalous pixels (e.g., dead, saturated). Dark current measurements were acquired before and after each observation. Next, the data were spectrally calibrated by associating a central wavelength (λ) and width to each band using ground calibration data. The data are radiometrically calibrated by converting each DN spectrum into physical units (i.e., in radiance *R(λ)* [W m^{-2} sr^{-1} μm^{-1}]) through an Instrument Transfer Function (ITF) and the exposure time (Figure 3.4). It is important to note that the ITF is a critical component for the calibration and has direct influence on the shape of the spectra and their absorption bands. The ITF was measured on ground before launch and consists of the instrument response multiplied by the flat field (De Sanctis et al., 2011; Ammannito et al., 2007). Calibration lamps within the instrument allow for validation or modification of the ground-based ITF during the flight (De Sanctis et al., 2011; Ammannito et al., 2007). The completely calibrated data is referred to as level 1b or RDR. The *reflectance factor* is obtained from the RDR following equation (6) (Figure 3.4):

$$REFF = \frac{R(\lambda)}{S(\lambda)\,/d^2}\frac{\pi}{\mu_0} \tag{8}$$

where the solar irradiance at Vesta is $S(\lambda)/d^2$ with $S(\lambda)$ the solar irradiance at 1 AU and d the distance Sun-Vesta in AU. As seen in Figure 3.4, reflectance factor spectra contain spikes and even-odd effects. Post-processing corrections can be applied to correct them (e.g., Ruesch et al., 2014a – Article II).

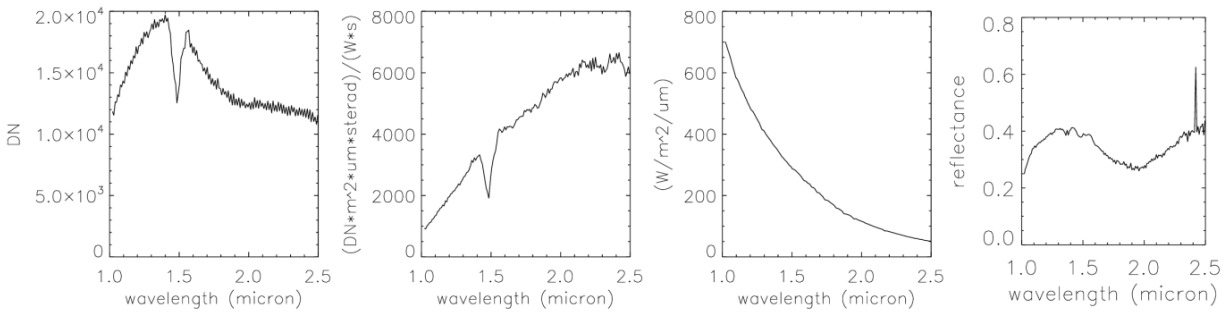

Figure 3.4 *Key spectra for the calibration of VIR IR data. From left to right: ITF, measured radiance R(λ), solar irradiance S(λ), and the final product, i.e., the reflectance factor.*

3.5.5 Analysis of reflectance spectra

To characterize a reflectance spectrum, key spectral parameters can be calculated. For pyroxenes dominated spectra, the parameters are the absolute reflectance usually measured at

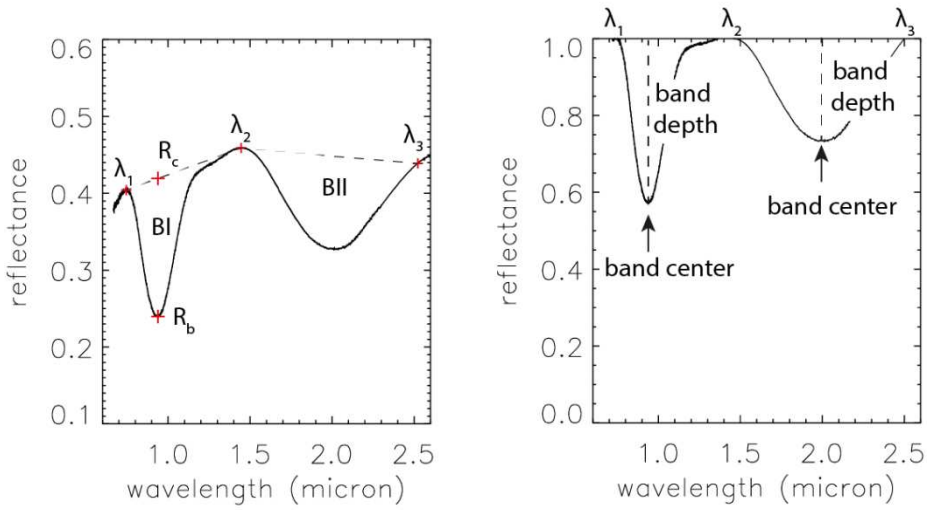

Figure 3.5 *Left: Reflectance spectrum of a pyroxene-dominated sample. Two broad absorption bands (BI and BII) are visible. Points λ_1, λ_2, and λ_3 are tie points at or close to the continuum of the spectrum, and separated by the absorption bands. Between the tie points, continua are approximated by dashed lines. R_b and R_c denote the reflectance at the band minimum and at the continuum. Right: reflectance spectrum divided by the continua. The depth and center are shown for both bands.*

0.56 µm, the spectral slope, i.e., the ratio of reflectance 0.75/0.56 and 1.45/0.75, and the depth of the relevant absorption bands, as illustrated in Figure 3.5 (e.g., Cloutis et al., 1986). The band depth is defined as $1-R_b/R_c$, where R_b is the reflectance at the band minimum and R_c the reflectance at the continuum (Clark and Roush, 1984). The bands centers are calculated by first dividing the reflectance spectrum by the bands continua, then by measuring the wavelength of the minimum of reflectance (Figure 3.5) (e.g., Burbine et al., 2009; Ruesch et al., 2015 – Article I). Cloutis et a. (1986) found that an additional parameter (Band Area Ratio, BAR) is useful to characterize spectra of pyroxene-olivine mixtures. The parameter is the ratio of the area within the BII and the area within the BI. The parameter exploits the fact that olivine admixture lead to different changes in the BII area relative to the BI area.

4. Review of articles

4.1 Ruesch et al., 2015 - Article I

Manuscript I treats laboratory investigation of the HED meteorites. The HED electron microprobe analyses are presented in section 3.4, and spectral analyses in section 3.5.5. From the suite of 24 HEDs, 4 samples have been spectrally analyzed as a function of observation geometry, and their investigations constitute the first part of Ruesch et al. (2015) – Article I. The comparison between the spectral analyses of the entire HED suite and the sample compositions represents the second part of this study.

Figure 4.1 illustrates reflectance spectra for a representative HED sample, the howardite NWA 1943, acquired under 24 observation geometries. As expected from previous studies (e.g., Gradie, 1980; Reddy et al., 2011), the main changes occur for the overall reflectance. Increasing incidence angles lead to a decrease of reflectance, whereas increasing emission angles, lead to a slight increase followed by a decrease in reflectance. Also identifiable in Figure 4.1 is the decrease of the ~1 µm and ~2 µm bands depths, as incidence and emission angles increase. The band depth decrease is weak to absent for incidence angle i=0°, i=15° and i=30°, and is considerable for i=45° and i=60°. In Ruesch et al. (2015) – Article I, I have compared the band depth decrease with changes in reflectance at 0.56 µm and found similarities with variations caused by compositional effects. Admixture of low albedo material to an eucrite powder leads to a decrease of reflectance and pyroxene band depth, as found by Cloutis et al. (2013). For an emission angle of ~45° or greater, such trend is undistinguishable from that due an increase in incidence angle. Thus, this needs to be considered in compositional investigations based on remote sensing data. Furthermore, as expected from previous studies (e.g., Gradie and Veverka, 1986), critical changes due to increasing incidence and emission angles are found for the spectral slopes and band area ratio parameter. As phase angles increase, the visible slopes first increase, than decrease, whereas the near-infrared slopes have a tendency to increase monotonically. Systematic changes are not found for the band area ratio parameter as phase angles, incidence or emission angles increase. The viewing and illumination conditions are found to have no effects on the band position, confirming previous studies (e.g., Beck et al., 2011). Thus, this latter spectral parameter can be used with reliability for compositional investigations.

In the second part of this study, the exact position of the ~1 µm (BI) and ~2 µm (BII) bands are calculated for the whole HED suite. These positions are compared to the average

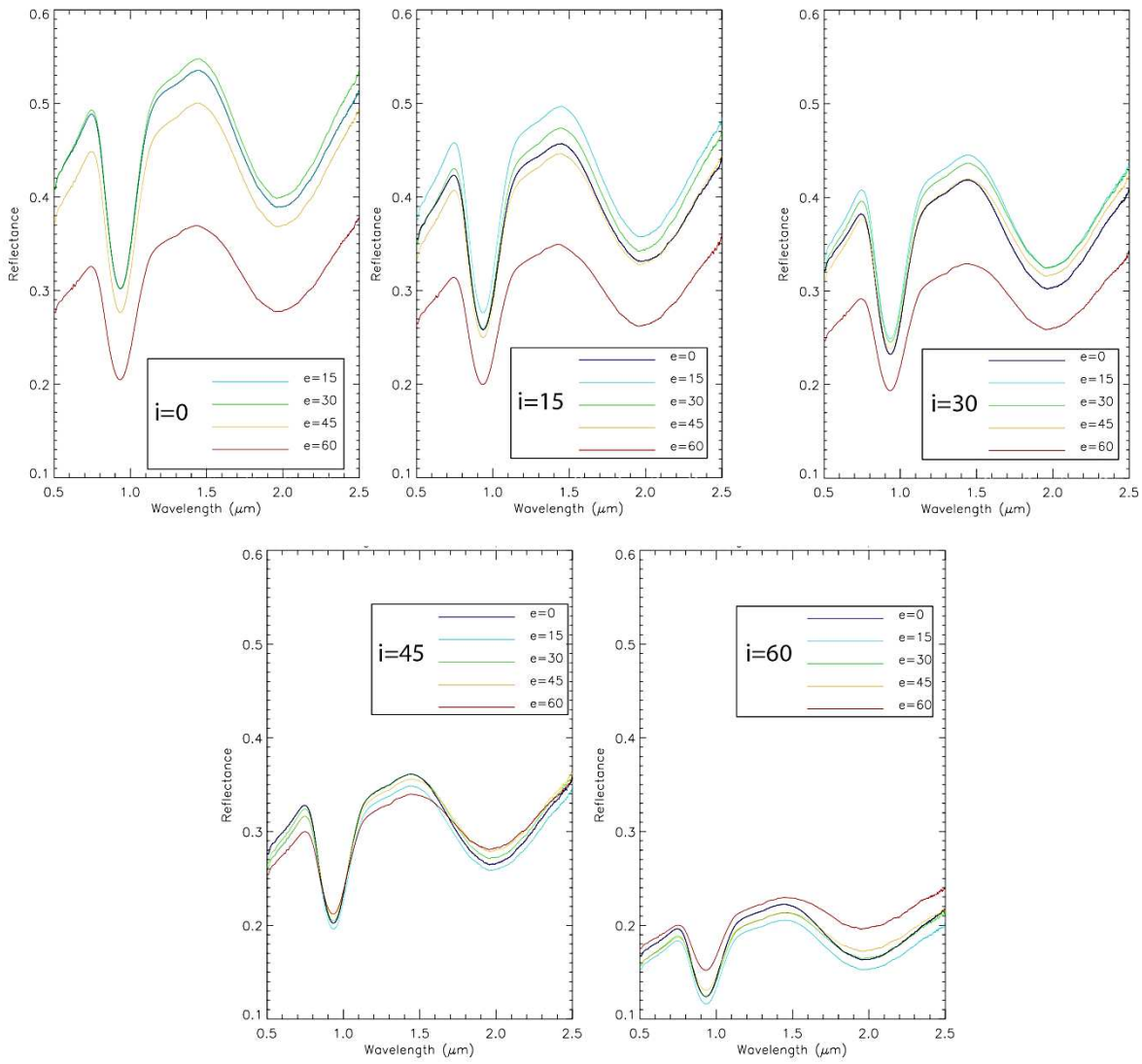

Figure 4.1 *Reflectance spectra of the NWA 1943 sample. Each plot illustrates measurements under the same incidence angle (i) but varying emission angles (e).Note (1) how the overall reflectance decrease, (2) the reflectance decrease is greater outside the absorption bands, leading to a decrease of the bands depths, (3) new bands do not appear, e.g., constant presence of the shoulder at ~1.2 μm.*

Ferrosilite (Fs) and Wollastonite (Wo) content of the samples powders obtained from EMPA analyses (described in section 3.4). As expected from the crystal field theory (e.g., Burns, 1993), a general proportionality was found between the Fs and Wo contents and the BI and BII positions. For pyroxene contents higher than Fs~50, discrimination between variations in iron and calcium content is ambiguous, as BI and BII centers are controlled by both elements. Previous studies have established empirical equations relating the band positions to the Fs and Wo contents (Gaffey et al., 2002; Burbine et al., 2009). I have investigated the validity of

these empirical calibrations by using the new and independent spectral and compositional dataset (21 pyroxene-dominated HEDs) compiled in this study. As a result, I found systematic differences of, in average, Fs~5 mol% and Wo~2 mol%. To overcome such discrepancies, I have provided new calibrations based on the HED suite.

These new calibrations have been applied to selected regions on Vesta, for which the modal mineralogy was modeled in Poulet et al. (2014) – Article IV. Band positions have been calculated from VIR reflectance data. The latter have been retrieved with the same methodology developed for Ruesch et al. (2014a) – Article II and Poulet et al. (2014) – Article IV, and described in section 3.5.5. The most iron-rich terrain has a pyroxene composition of $Fs_{47}Wo_{14}$ and the most iron-poor terrain has a composition of $Fs_{30}Wo_{5}$ (Figure 4.2). The use the Burbine et al. (2009) calibrations, which are based on fewer HED samples, results in slightly higher Fs and Wo values (Figure 4.2).

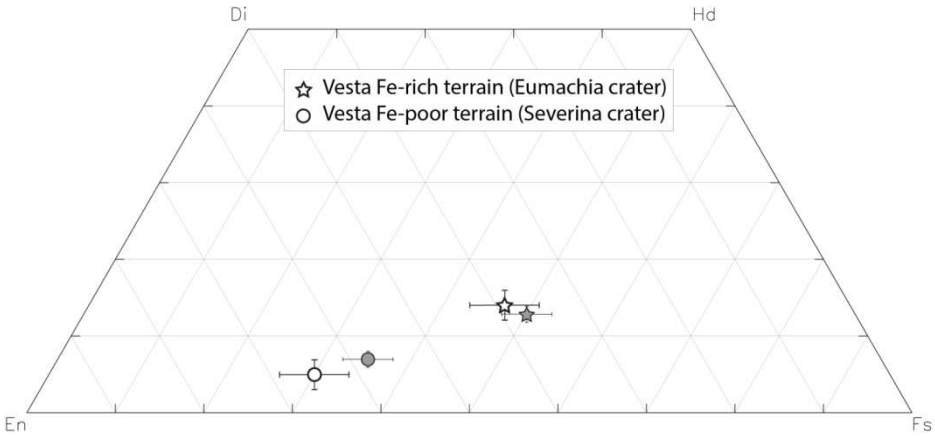

Figure 4.2 *Pyroxene quadrilateral with derived compositions for two end member terrains on Vesta. Solid symbols show compositions calculated with the calibration of Burbine et al. (2009) and open symbols with the calibration developed in Ruesch et al. (2015) – Article I.*

These pyroxene compositions are consistent with the derived modal mineralogy (including low-Ca and high-Ca pyroxene) by Poulet et al. (2014) – Article IV. They correspond to the spatial average composition of few kilometers wide areas. The low-iron area is located in the southern hemisphere, in the topographically low Rheasilvia basin, whereas the high-iron area is located in the equatorial region at higher elevation (Poulet et al., 2014 – Article IV). These contexts suggest that the igneous activity of the early Vesta formed lithologies with varying pyroxene compositions as a function of the depth, or elevation. As also found by De Sanctis et al. (2012), Prettyman et al. (2012), and Yamashita et al. (2012), these lithologies are

consistent with a predicted crust structure of the HED parent body (Takeda, 1979; Righter and Drake, 1997; Ruzicka et al., 1997; Pieters et al., 2011; McSween et al., 2013).

4.2 Ruesch et al., 2014a - Article II

The discovery of olivine based on VIR data was reported in Ammannito et al. (2013) – Article V. The study revealed that the spectral signature of olivine is subdued relative to pyroxenes, implying a relatively low amount of olivine at the spatial sampling of VIR (~170 m/pixel). It is worth mentioning that the determination of the iron content of olivine by reflectance spectra is not straightforward, as the olivine absorption bands are also a function of the grain size of the olivine, which is an additional unknown (e.g., Sunshine and Pieters, 1998; Poulet et al., 2014 – Article IV). Furthermore, the observed olivine on Vesta is always admixed with pyroxene, i.e., in a multicomponent nonlinear mixing (Moroz and Arnold, 1999). The location of the spectral signature of olivine was found in the northern hemisphere, associated with craters Bellicia and Arruntia, and not in the southern hemisphere where the exposed olivine-dominated mantle was expected (e.g., Pieters et al., 2011; McSween et al., 2013). Thus, although the early result identified a spectral signature of olivine in a few limited regions, no evidence for an olivine-dominated mantle was found (Poulet et al., 2014 – Article V).

As a follow-on study, Ruesch et al. (2014a) – Article II investigated the global spatial occurrences of olivine enrichments and their local morphological settings. In order to detect the spectral signature of olivine, a method was developed to study the subtle variations of the VIR spectra. In particular, spectral parameters were calculated for the whole dataset. Spectra with key parameter variations (e.g., in the Bellicia-Arruntia region) were visually investigated and attention was given to the wavelength increase of the band at ~1.2 µm, to the wavelength shifting of the band center near ~2 µm, and to the overall decrease of the pyroxenes bands with decreasing albedo. Following the visual investigations, thresholds based on the spectral parameters were defined in order to identify enrichments in olivine relative to the surroundings (Figure 4.3). Knowledge of geometry effects acquired during the study of Ruesch et al. (2015) – Article I was exploited for the development of the spectral parameters.

In this study, the area around craters Bellicia and Arruntia first identified in Ammannito et al. (2013) – Article V was confirmed to be the most olivine enriched area on Vesta, and was spectrally mapped in detail (Figure 4.4). A dozen of additional sites were identified with an equal or weaker spectral signature of olivine as the Bellicia-Arruntia region (Ruesch et al., 2014a – Article II).

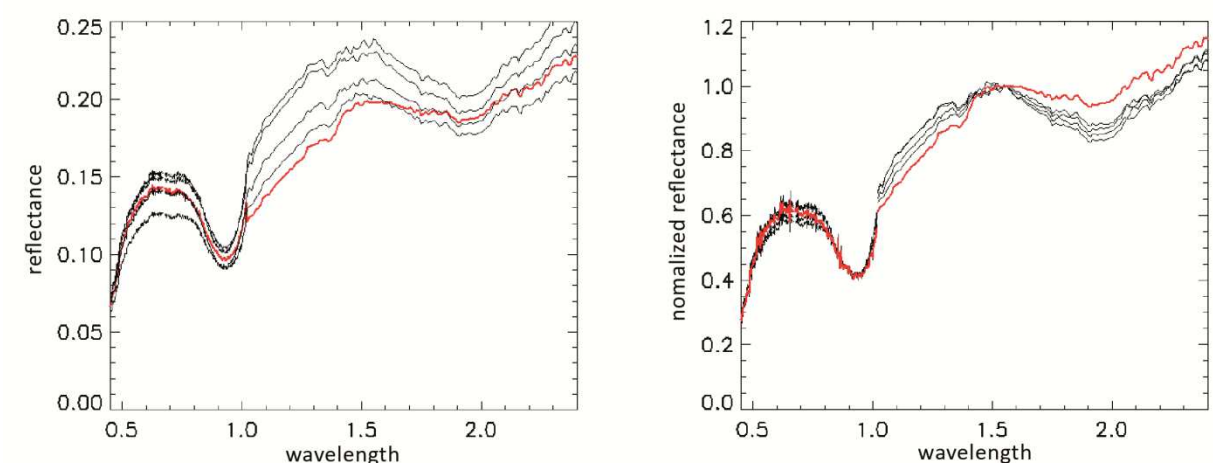

Figure 4.3 *VIR spectra of Bellicia crater from Ruesch et al. (2014a) – Article II. The spectra are taken outside and within (red spectrum) an olivine rich area. Note the large spectral variation between 1.0 and 1.5 µm.*

Once olivine enriched pixel were identified, they were mapped to characterize their spatial variations. All but one site are located within the eastern hemisphere, northward of ~40°S (Ruesch et al., 2014a – Article II). The identified sites cover an area of 5-25 km^2 each. The sites are found at or near impact craters of diameters between 5 to ~50 km. The craters are morphologically fresh and younger than 600-1000 Ma (Ruesch et al., 2014b - Article III, Ruesch et al., 2014a – Article II). The geologic contexts of the olivine-rich areas are diverse. Often they correspond to downslope material (dust or debris avalanches) and to spurs on crater walls. Other occurrences are associated with small craters less than ~1 km. Only a few sites are related to the Rheasilvia impact ejecta and to low-Fe pyroxenes. These latter sites directly sample material that was located at depths of a few to few tens of kilometers before the impact of the Rheasilvia basin (Ruesch et al., 2014a – Article II). Thus, small-scale enrichments in olivine and low-Fe pyroxene were present within the crust before the Rheasilvia impact.

The investigations of the geologic context imply that olivine-enriched surfaces on today´s surface are poorly gardened. It is proposed that once exposed on the surface, olivine grains get fractured, broken apart and mixed within the surface regolith. As the regolith is spectrally dominated by pyroxenes, the olivine signature will decrease with time.

On the basis of a comparison with laboratory mixtures of olivine and orthopyroxene, the highest concentration of olivine was estimated at ~50-60 vol% (Ammannito et al., 2013 – Article V). The quantitative estimation of the lowermost concentration of olivine in the soil of Vesta was the subject of Poulet et al. (2014) – Article IV, and is briefly described here.

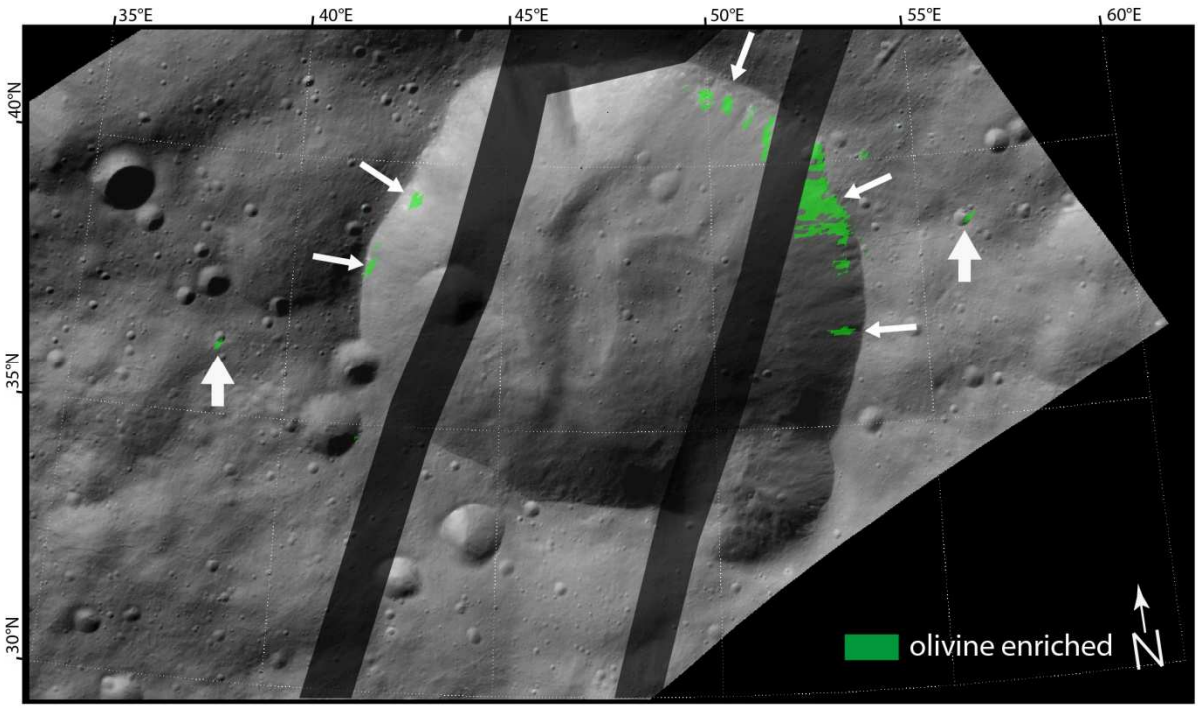

Figure 4.4 *Framing Camera images of the impact crater Bellicia and olivine enriched areas identified in Ruesch et al. (2014a) – Article II. Olivine is found on the Bellicia crater wall, where rocky spurs and mass wasting occur (thin arrows). Smaller craters on the ejecta of Bellicia also expose olivine-rich material (thick arrows). Bellicia crater is approximately 60 km in diameter.*

In Poulet et al. (2014) – Article IV, spectral modeling based on the Shkuratov radiative transfer theory (Shkuratov et al., 1999) was used to fit near-infrared spectra for a subset of the HED suite presented in Ruesch et al. (2015) – Article I. Abundance estimates of the end-member mineral spectra were accurate to within 15-25 vol%. The particle sizes of the end-members were also appropriately estimated. Next, the same modeling technique was applied to VIR data. With the expected minerals, i.e., low-Ca and low-Fe pyroxene, high-Ca pyroxene, plagioclase, and olivine, satisfactory fits of the VIR spectra were achieved. The retrieved mineralogy was relatively uniform for different terrains of Vesta, confirming the presence of a well-gardened regolith. It was found that the olivine component was required in modeling each studied spectrum, with abundances around 10-15 vol%. Furthermore, a bimodal distribution of grain sizes was inferred with coarse-grained olivine (~200 µm) and fine-grained (~100 µm) pyroxenes and plagioclases. Such widespread low amount of olivine in Vesta´s soil is consistent with morphological observations (described in Ruesch et al., 2014b – Article III) indicating regolith mixing of olivine and pyroxene. The implications of such findings are discussed in Chapter 5.

4.3 Ruesch et al., 2014b - Article III

In manuscript III, the geologic maps of the 5 quadrangles of the northern hemisphere of Vesta are presented. With the support of CSFD measurements, the geological evolution of the hemisphere is discussed. Here, the geologic units and events characterizing the history of the northern hemisphere on Vesta are briefly presented in chronological order, from the oldest to the youngest (Figure 4.4). It is noteworthy to mention that inconsistencies with the production function are found for terrains older than ~3 Ga, leading to less reliable absolute model ages for such older units (Ruesch et al., 2014b – Article III).

The unit *cratered highland* (brown color in Figure 4.4) has a densely cratered surface and usually stands at higher elevations relative to the other major units. In Schmedemann et al. (2014) – Article IX, its age was approximated at 3.4-3.8 Ga. It is interpreted as an ancient crustal material fractured by impacts (Ruesch et al., 2014b – Article III and Blewett et al., 2014 – Article VII). It has similar characteristics, although lower elevation, as Vestalia Terra, interpreted as a plateau overlying a fossil mantle plume (Raymond et al., 2013; Buczkowski et al., 2014). Three ruin (i.e., morphologically subdued) basins have formed on the cratered highland, i.e., Caesonia (~100 km in diameter), Varronilla (~200 km in diameter) and Postumia (~200 km in diameter). A fourth large impact occurred sometime later at the South Pole and formed the Veneneia basin (Jaumann et al., 2012). This event marks the end of the Pre-Veneneian epoch and the beginning of the Veneneian epoch (Williams et al., 2014a). The Veneneia impact disrupted part of the cratered highland terrain in the northern hemisphere. Such modified terrains were defined as *Saturnalia Fossae cratered terrain* and the *Saturnalia Fossae trough terrain* (dark and light purple, respectively in Figure 4.4). Both units are characterized by ridges and troughs up to tens of km in length. They are more frequent and less subdued in the *Saturnalia Fossae trough terrain* compared to the *Saturnalia Fossae cratered terrain*. The Rheasilvia impact occurred at the actual South Pole at about 3.5 Ga or 1 Ga, depending on the chronology (Schmedemann et al., 2014 – Article IX; Williams et al., 2014a; Marchi et al., 2012). This event defined the beginning of the Rheasilvian epoch (Williams et al., 2014a). Large tectonic features related to Rheasilvia are not recognized in the northern hemisphere. Small scale lineations (i.e., ridges, grooves), however, might be surface expressions of faults induced by the Rheasilvia impact (Scully et al., 2014 – Article VIII). Near the Veneneia and Rheasilvia antipodal areas, small-scale linear depressions were also identified, consistent with impact-induced stresses (Blewett et al., 2014 – Article VII). However, large-scale morphological features at the basins antipodes, instead, as seen on larger bodies such as the Moon and Mercury, are lacking (Blewett et al., 2014 – Article VII). The

evolution of the northern hemisphere after the Rheasilvia event is characterized by impact craters of diameter less than ~60 km. Bellicia crater, which mineralogy is described in Ruesch et al. (2014a) – Article II, represents one of these event. It partly impacted on the ancient crustal material of unit *cratered highland*. Overall, these young impacts formed a continuous ejecta blanket and outer discontinuous ejecta (various level of yellow in Figure 4.4). Starting at about 100-150 Ma, the Marcian epoch succeeded the Rheasilvian epoch (Ruesch et al., 2014b – Article III; Williams et al., 2014a). Such epoch is characterized by morphologically fresh features. Low albedo ejecta also characterize some craters, and are interpreted as signs of exogenous contamination by carbonaceous chondrite material (Reddy et al. 2012; McCord et al., 2012). The most recent events consist of mass movements, such as fine-grained debris avalanches, especially at steep slopes on crater walls.

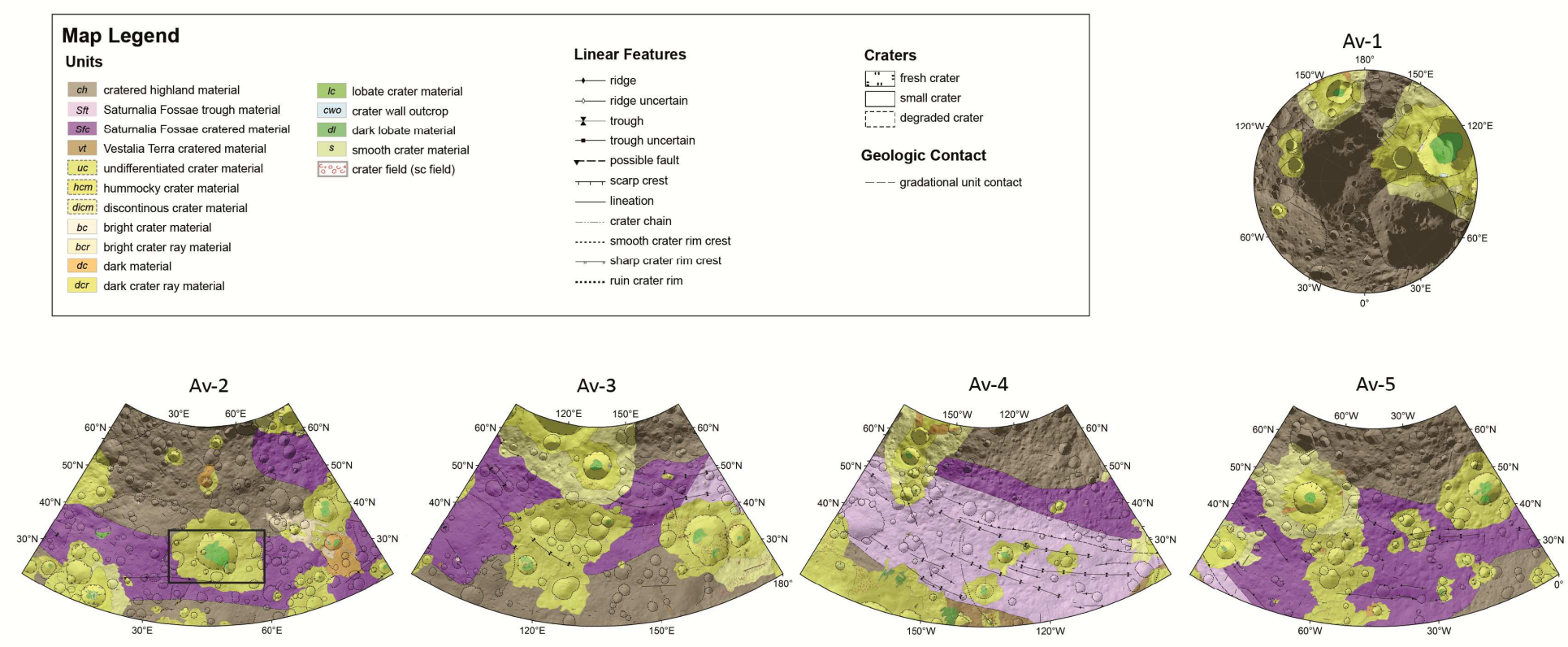

Figure 4.5 *Geologic maps of the northern hemisphere of Vesta subdivided into five quadrangles (see Figure 3.1), from Ruesch et al. (2014b) – Article III. Inset in Av-2 indicates location of Figure 4.3 (Bellicia). The brown color unit is the cratered highland, formed during the Pre-Veneneian epoch. Purple and light purple units are terrains fractured by the Veneneia impact. Yellow units indicate crater materials formed during the most recent epochs, the Rheasilvian and Marcian.*

5. Discussion

5.1 Overview

Vesta's geological history has been divided into four epochs, from the older to the younger: Pre-Veneneian, Veneneian, Rheasilvian and Marcian (e.g., Williams et al., 2014a; Ruesch et al., 2014b – Article III). Here I present the major events and processes that occurred during these epochs and that can be retraced to today´s surface morphology and mineralogy. Results from Articles I, II, III and IV form the basis of this discussion, which focuses on the olivine bearing materials and their parent lithologies.

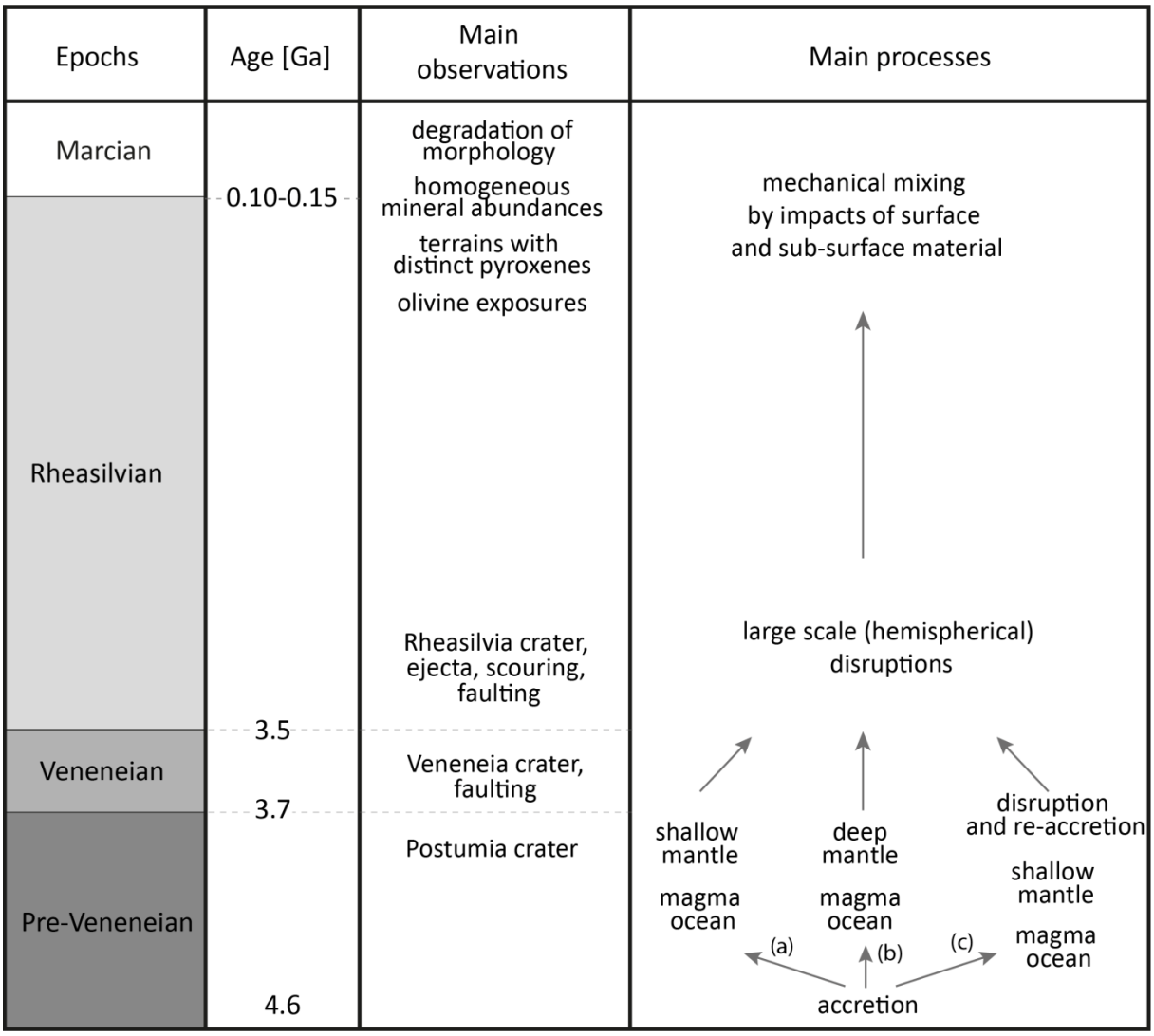

Figure 5.1 *Chronological table summarizing the geological history of Vesta, subdivided into Vesta´s four geological epochs. In the "Main processes" column, interpretations explaining the main observations and the different scenarios (a, b and c) for the Pre-Veneneian epoch are reported. Absolute ages are discussed in Williams et al., (2014a).*

5.2 The Pre-Veneneian Epoch

Despite the relatively homogeneous modal abundances of minerals (Poulet et al., 2014 – Article IV; Stephan et al., 2014 – Article VI), compositionally distinct terrains are present on today´s Vesta (De Sanctis et al., 2012; Yamashita et al., 2013; Stephan et al., 2014 – Article VI ; Ruesch et al., 2015 – Article I) and in one occasion with a distinct morphology (Vestalia Terra, Buczkowski et al., 2014). These terrains have probably formed during the magmatic activity of the Pre-Veneneian epoch. An additional piece of evidence for the preservation of terrains comes from the previously mentioned olivine-enriched material in close proximity to low-iron pyroxene and in association with Rheasilvia ejecta (Ruesch et al., 2014a – Article II). Such minerals are reminiscent of small scale ultramafic complexes, such as plutons, formed during the Pre-Veneneian epoch. If these terrains are indeed relatively intact and of magmatic origin, they were preserved up to the Marcian epoch despite the disruption and distribution of part of the crust due to large impacts (at least up to ~500 km in diameter). This interpretation fits into the scenario of Vesta as an intact differentiated protoplanet (Russell et al., 2012; De Sanctis et al., 2012) (Figure 5.1, a and b), where pristine magmatic constructs such as plutons would be exposed by later impacts (e.g., Pieters et al., 2011), during the Veneneian, Rheasilvian and Marcian epochs. The magmatic activity was probably related to the crystallization of a magma ocean, as several chemical and isotopical studies of HEDs propose (McSween et al., 2011; Barrat et al., 2010; Takeda, 1979; Righter and Drake, 1997; Ruzicka et al., 1997). As a consequence of the magma ocean crystallization, several studies predict a 15-20 km thick crust represented by eucrites and diogenites, overlaying a (shallow) olivine mantle (McSween et al., 2011; McSween et al., 2013). This “shallow mantle” scenario (Figure 5.1, a) is in agreement with several HED analyses, but it is not supported by Dawn observations (Ammannito et al., 2013 – Article V, McSween et al., 2013).

To explain the lack of mantle exposure within the large basins, it has been proposed that Vesta has a thicker crust than previously modeled, possibly as thick as 80 km (Figure 5.1, b; Clenet et al., 2014). A thicker crust and a deep mantle would be the result of intrusions after global-scale melting (i.e., the magma ocean) and after deep cumulate crystallization, as suggested by some HED analyses (Barrat et al., 2010; Yamaguchi et al., 2011). Such putative intrusions could also explain the small-scale ultramafic plutons exposed by Rheasilvia (Ruesch et al., 2014a – Article II).

The idea of Vesta being a relatively intact protoplanet, contrasts with another scenario developed to explain the missing olivine mantle. Consolmagno et al. (2014) proposed that during the Pre-Veneneian, the collisional environment was so intense that it disrupted the

protoplanet, and that Vesta formed by re-accretion of altered and chemically stripped material (Figure 5.1, c). This latter scenario could provide an explanation for the tentatively proposed widespread low-abundance of olivine (Poulet et al., 2014 – Article IV). In fact, Article IV proposed that the intense impact bombardment of the Veneneian and/or pre-Veneneian epoch has disrupted and globally distributed the olivine-dominated mantle (Poulet et al., 2014 – Article IV). Although this observation supports a re-accretion model as proposed by Consolmagno et al. (2014), a note of caution is necessary. Uncertainties remain on the VIR ITF (Ammannito pers. com.) and thus on the identification of widespread olivine. As a consequence, a confirmation of the ITF reliability is needed before far-reaching interpretation can be made. Impacts during the Pre-Veneneian epoch leading to global-scale resurfacing have possibly been erased in later epochs. Thus, for such ancient events, morphological investigations provide no insights. At this point, the production functions presented in chapter 3.3 can be helpful to illustrate the range of bombardment scenarios during the Pre-Veneneian. The empirical lunar-like production function predicts that the number of Rheasilvia-sized impacts formed before ~3 Ga was high, reaching a total of 6 Rheasilvia-sized impacts at ~4 Ga (Schmedemann et al., 2014 – Article IX). Thus, I suggest that global-scale resurfacing would have been possible by such putative large impacts. It is worth mentioning that the numbers of impacts before ~ 4.1 Ga cannot be modeled because the lunar-like production function is defined for ages up to ~ 4.1 Ga (Schmedemann et al., 2014 – Article IX). The other end-member scenario for the history of impacts during the Pre-Veneneian is provided by the production function of the dynamical model (O´Brien et al., 2014). This latter function predicts less than 2 Rheasilvia-sized impacts over the entire Vesta´s history (O´Brien et al., 2014). In this scenario, Rheasilvia was probably the only largest impact, implying no global-scale resurfacing events. This limit of size and number of impacts on Vesta is a consequence of an observational constrain: Vesta retains a largely intact basaltic crust (e.g., Davis et al., 1985), and thus was not shattered (e.g., Davis et al., 1985; O'Brien et al., 2014).

Note that although two different approaches have been developed for the Vesta impact history, none provides an explanation for an observed excess in crater density between ~8 to ~11 km in diameter (Ruesch et al., 2014b – Article III). Hence, further investigations on the Vesta production functions are needed and could provide new insights into the bombardment history.

In addition to (i) the lack of olivine-dominated lithology in the deepest region of Vesta, (ii) the possible widespread low abundance of olivine, and (iii) the small-scale occurrences of olivine enriched material, a fourth unexpected mineralogical observation deserves to be

mentioned. Within the Rheasilvia basin, i.e., in the deepest region of Vesta, VIR observations identified exposures of a high albedo material probably with a high content of feldspar (Zambon et al., 2014). Feldspar was expected to be present on Vesta on the basis of eucrite mineralogy, and Poulet et al. (2014) – Article IV indeed reported that feldspar is widespread on Vesta, although with apparently small abundances. The detection of a feldspar-rich material at great depths within Vesta is unexpected, however, and is reminiscent of a felsic lithology. In recent years the importance of felsic rocks in planetary bodies has been revisited (Terada and Bischoff, 2009; Wray et al., 2013; Carter and Poulet, 2013) and might also be of importance for Vesta. Hence, future HED studies and petrological models should take such lithology into consideration.

It appears that the 3 main scenarios (Figure 5.1, a, b and c) are capable of at least partly explaining the present characteristics of Vesta and the inferred properties of the HED parent body. The whole sets of observations are not explained by a single model, however. The difficulty probably arises from the two opposite sets of observations and interpretations. One set gives insights into planetary differentiation models from HED meteorites, the other is forced to constrain the models from orbital remote sensing.

5.3 The Rheasilvian and Veneneian Epochs

The Veneneian and Rheasilvian epochs were punctuated by two large impact events. Studies based on impact modeling have shown that impacts of the size of the Rheasilvia and Veneneia basins distributed ejecta material several kilometers thick all over the Vesta surface (Jutzi et al. 2013). Such ejecta were interpreted as having distributed material rich in olivine presumably from the mantle. Ruesch et al. (2014b) – Article III revealed that thick ejecta from the basins in the southern hemisphere is not distributed globally, but is limited to the southern and equatorial regions (Ruesch et al. (2014b) – Article III; Stephan et al., 2014 – Article VI). Only small-scale ridges and lineations might originate from Rheasilvia ejecta scouring (Ruesch et al., 2014a – Article II; Ruesch et al., 2014b – Article III; Scully et al., 2014 – Article VIII). The amount of material that could have been distributed by such process (ejecta scouring) is not well constrained (Ruesch et al., 2014a – Article II). On one hand, the amount of material distributed from the southern to the northern hemisphere by such process is limited, as most ejecta material is deposited within one crater radius from the rim (e.g., Housen and Holsapple, 2011). On the other hand, the sizes of the Rheasilvia and Veneneia basins are large relative to Vesta's diameter; a special case usually not taken into account in common ejecta modeling and investigated in great detail (e.g., Housen and Holsapple, 2011).

Nevertheless, the absence of clear morphological resurfacing by the Rheasilvia and Veneneian ejecta at northern latitudes is taken to exclude an link between most of the olivine-rich sites and the south polar basins. In only a few locations in the southern hemisphere, the relationship with Rheasilvia has been clearly established (see next section) (Ruesch et al., 2014a – Article II).

The presence of an ubiquitous low-amount of olivine, as suggested in Poulet et al. (2014) – Article IV, implies an olivine-rich parent lithology, such as an olivine-rich mantle, and an efficient process of mixing (Poulet et al., 2014 – Article IV). The question remains whether the Rheasilvia and Veneneia impacts were responsible for the exposure of the main olivine lithology (Poulet et al., 2014 – Article IV), or whether older impacts already disrupted and partly distributed the material. Because the ejecta from the Rheasilvia impact is not globally present, I suggest that previous impacts, during the Pre-Veneneian epoch, were responsible for the global distribution of olivine-bearing material. Pre-Veneneian relicts of impact basins that can be recognized on today´s surface are few, and smaller than Rheasilvia (e.g., Postumia basin is ~200 km in diameter). Thus, large basins responsible for global resurfacing, if they occurred, were later erased or obscured by subsequent impacts.

5.4 The Marcian Epoch

During the most recent epoch, the Marcian, the surface evolution was dictated by impacts and the formation of craters with diameters less than ~60 km. Each impact started a multitude of processes. Rapid overturn of material occurred up to approximately 5 km deep (Ruesch et al., 2014b – Article III; Melosh, 1989), followed by exposure at the surface of un-gardened material. Vertical redistribution of material at the surface by ejecta emplacement was limited to less than ~30 km (Ruesch et al., 2014b – Article III; Melosh, 1989). No impact event with global effects occurred. At the crater interiors, mass wasting processes were active, including slumps, debris flows and fine-grained avalanches. Note that additional processes occurred, not discussed in this thesis. Such processes are related to volatile loss and pitted terrain formation (Denevi et al., 2012) and impact melt formation, leading to melt flows and ponds (Williams et al., 2014b). During the Marcian epoch, mass wasting processes were responsible for the exposure of material enriched in olivine materials and with compositionally distinct pyroxenes. After exposure, the fresh material was subject to surface mixing. Such long-lasting process is due to micrometeorite bombardment and led to regolith formation (Pieters et al., 2012). It is also responsible for the globally uniform abundance of minerals (Poulet et al.,

2014 – Article IV). During this epoch, the sub-surface material underwent several cycles of exposure to the surface, mechanical mixing and burial by overlaying material.

Exposure of olivine-enriched material requires further discussion. In Ruesch et al. (2014a) – Article II a magmatic lithology was proposed for the origin of the olivine-enriched material (further discussed in section 5.2), whereas Nathues et al. (2014) argued that the dozen of olivine enriched sites do not all share the same origin. Observations described in Ruesch et al. (2014a) – Article II highlight diverse geologic contexts and are consistent with this latter interpretation. Nathues et al. (2014), however, suggested that most of the olivine-enriched material is due to infall of olivine-rich impactors (e.g., chondritic and achondritic-like material), whereas only fewer locations were explained by endogeneous, possibly magmatic, material. Although the exogeneous origin cannot be completely excluded, one specific observation argues against a major contribution from infall material. The sites are limited to one hemisphere, whereas dark material occurrences, that have a well established exogeneous origin (McCord et al., 2012; Reddy et al., 2012; Stephan et al., 2014 – Article VI), are found globally. The shallow depths at which the material occurs is interpreted to imply a surface (exogenic) source (Nathues et al., 2014). In Ruesch et al. (2014a) – Article II it is shown how the depth of the material is related to the exposure process: olivine-rich material cannot be observed at greater depths on today´s surface because it is probably covered by mass wasting deposits. Thus, the shallow depth does not necessarily suggest a shallow or exogenous origin (Ruesch et al., 2014a – Article II).

5.5 Note on the origin of HED

The “missing mantle” topic discussed above constitutes a major inconsistency between the mineralogy of Vesta’s interior and that of the HED parent body. Thus, strong evidence for the genetic link between the two bodies remains elusive, although there have been attempts to reconcile the observed rarity of olivine on Vesta with the mineralogy of the HED parent body (McSween et al., 2013; Clenet et al., 2014). On the other hand, the pyroxene chemistry and distribution is in agreement with predictions for the HED parent body (Ruesch et al., 2015 – Article I; De Sanctis et al., 2012; Ammannito et al., 2013). As demonstrated in Ruesch et al. (2015) – Article I, the pyroxenes on Vesta are very similar to those of the HEDs in their iron and calcium contents (Ruesch et al., 2015 – Article I). An eucritic lithology is relatively well preserved, whereas a pure diogenite lithology is not found in the study of Ruesch et al. (2015) – Article I, suggesting that the lithology is rare, possibly due to intense disruption and mixing (Ruesch et al., 2015 – Article I). Indeed, Zambon et al. (2014) confirm that diogenites are

composed of only a few percent of fresh material. The partial ambiguity on the HED origin remaining after the Dawn mission suggest that, future orbital remote sensing observations should ideally be coupled with in situ measurements.

6. Conclusions

In this thesis I exploited a range of remote sensing approaches, from photo-geologic mapping to meteorite spectroscopy, to unveil part of Vesta´s geological history from the first orbital observations of a large asteroid provided by Dawn.

HED meteorites have been investigated as they provide the closest near-infrared spectral analog to Vesta´s surface. With an interferometer-based spectrometer, I characterized the HED near-infrared reflectance spectra and their variations as a function of observation geometries. The quantitative relation between spectral properties and pyroxene composition has been determined on the basis of the largest and most representative HED samples suite to date. The main outcomes and applications of this investigation are:

(1) Spectral variations due to geometry effects can be distinguished from compositional variations, i.e., olivine or low albedo material admixture, within a certain range of low phase angles (Ruesch et al., 2015 – Article I).

(2) Using a subset of HEDs, a radiative transfer modeling for reflectance spectra was tested to determine modal abundances (Poulet et al., 2014 – Article IV).

I retrieved reflectance spectra of Vesta from VIR/Dawn data acquired at unprecedent spectral and spatial detail. Here, the main results obtained on the basis of VIR data are summarized.

(3) By applying the quantitative relationship between spectral properties and pyroxene compositions to the VIR spectra, I determined absolute pyroxene composition of different areas on Vesta. Their distinct pyroxene compositions probably reflect distinct terrains of magmatic origin formed during the earliest Vestan epoch, the Pre-Veneneian (Ruesch et al., 2015 – Article I).

(4) By applying the radiative transfer modeling to VIR spectra, the presence on the surface of the following minerals is detected: low-iron pyroxene, high-iron/calcium pyroxene, plagioclase, and olivine (Poulet et al., 2014 – Article IV). Their abundances are relatively homogeneous across the whole surface of Vesta. Although the reliability of the VIR calibration needs confirmation, olivine appears to be widespread and constitutes 10-15 vol% (Poulet et al., 2014 – Article IV).

(5) Higher abundances of olivine (upper limit 50-60 vol%) are found in spatially limited areas (<25 km^2), usually occurring in the eastern hemisphere (Ruesch et al., 2014a – Article II). Largest occurrences are in the northern latitudes. No evidence for an olivine-dominated mantle was found, contradicting previous models for Vesta´s differentiation (Ammannito et al., 2013 – Article V; Ruesch et al., 2014a – Article

II). I surmise that the lack of an olivine-dominated mantle is related to the general low abundance of olivine-dominated asteroids in the main belt.

I have exploited the unique images provided by the FC/Dawn to produce a photo-geological map of the northern hemisphere, where the higher abundances of olivine are found. Also, I determined absolute model ages of specific terrains by crater size-frequency measurements. These investigations revealed:

(6) The olivine-bearing material is subject to surface mixing and to cycles of exposure and burial occurring at least during the Vestan epoch, the Marcian epoch (<150 Ma) (Ruesch et al., 2014a – Article II; Ruesch et al., 2014b – Article III). Putative small-scale ultramafic complexes of olivine and low iron pyroxene on the southern hemisphere were exposed by the large Rheasilvia impact (Ruesch et al., 2014a – Article II).

(7) The Rheasilvia (~3.5 Ga) and Veneneia (~3.7 Ga) impacts created graben systems but did not affect the northern hemisphere with resurfacing events (Ruesch et al., 2014b – Article III). Hence, they were not responsible for the distribution of most of the olivine-enriched material. This partly contradicts impact modeling of ejecta emplacement. Global-resurfacing events – if any - must have occurred earlier, during the Pre-Veneneian (>3.7 Ga).

These original results provide constraints on the differentiation and history of a large proto-planet. A few scenarios for Vesta differentiation and early evolution have been proposed by other studies (e.g., McSween et al., 2013; Clenet et al., 2014; Consolmagno et al., 2014). Each of these scenarios receives support by one or several of the observations reported in this thesis, i.e., points 3 to 7. However, none of the scenarios provide consistent explanations for the entire range of observations. Thus, it might be necessary to revisit the concepts of differentiation and the structure (crust-mantle boundary) of protoplanets: for example, by taking into account a thicker crust as proposed, for example, by Clenet et al. (2014). Alternatively, a more extreme change of ideas might be necessary, for example the view of Vesta as a re-accreted body (Consolmagno et al., 2014). Whether based on pre-Dawn knowledge or developed in recent years, both scenarios deserve further investigations. The lack of mantle exposure (Ruesch et al., 2014a – Articles II; Ammannito et al., 2013 – Article V) constitutes an apparent disagreement with the current concepts of the HED parent body, and does not provide further support for the genetic link between HED and Vesta. Nevertheless, the range of iron and calcium contents in pyroxene on Vesta (Ruesch et al., 2015 – Article I) is consistent with the HED parent body.

7. Outlook

The understanding of Vesta as presented in this study and the differences and inconsistencies with our current understanding of HEDs reveal the importance of planetary exploration by spacecraft. Pre-Dawn concepts of Vesta´s interior structure and differentiation based on HED, although mostly agreed upon, are partly incorrect. These concepts need to be partly revisited in the light of recent Dawn results. The crucial, comprehensive characterization of Vesta was possible only after orbit insertion: a fly-by mission would have revealed only a partial and possible false understanding of this main belt body. On the other hand, the genetic link between HED and Vesta remains an open question, even after the success of the Dawn mission. Thus, as the next step, the scientific community should consider in-situ investigations to decipher this open scientific question.

Concerning future studies of Vesta with the acquired Dawn´s observations, I suspect that possible relevant insights into the role of the Rheasilvia impact (and the fate of a possible preexisting olivine lithology) could be gathered with a detailed, local-scale study of small-scale lineations and ridges related to the Rheasilvia basins. In addition, the study of howardites, consisting of olivine-rich impact-melt rocks, might shed light into the impact processes and the properties of the regolith. These properties will have direct consequences for the near-infrared spectral range observed by VIR/Dawn. I also argue that the understanding of crater size-frequency deviations from the expected production functions needs further attention and might have implications for our understanding of the bombardment history throughout the Solar System.

Considerable understanding of Vesta can possibly be gathered from studies of similar sized asteroids (i.e., Juno, Pallas, Ceres) even if they have different composition. In this respect, the Dawn investigations of dwarf planet Ceres, starting March 2015, should greatly improve the understanding of Vesta. Although Ceres is located at 2.8 AU, in an outer zone of the main belt relative to Vesta, insights from Ceres´s bombardment history will be helpful in depicting Vesta’s bombardment history. The campaign at Ceres can provide observations by the VIR instrument with which the reliability of the VIR ITF can be improved. For example, it might be useful to compare VIR observations of Ceres with ground-based observations. If the precision of the VIR ITF can be improved, more reliable quantification of the olivine abundance on Vesta will be obtained.

References

Adams, J. B., and A. L. Filice (1967), Spectral reflectance 0.4 to 2.0 microns of silicate rock powders, J. Geophys. Res., 72(22), 5705, doi:10.1029/JZ072i022p05705.

Adams, J. B. (1974), Visible and near-infrared diffuse reflectance spectra of pyroxenes as applied to remote sensing of solid objects in the solar system, J. Geophys. Res., 79(32), 4829, doi:10.1029/JB079i032p04829.

Ammannito, E. (2007), Laboratory spectroscopy to support the Dawn space mission, PhD Thesis, Università degli studi di Padova, Padova.

Anderson, J.A., K.J. Becker, T.N. Titus, M.C. De Sanctis, A. Nathues, F. Tosi, et al. (2011), Isis Cartographic Tools for the Dawn Framing Camera and Visual and Infrared Spectrometer, American Geophysical Union, Fall Meeting, Abstract #U31A-0009.

Arvidson R., J. Boyce, C. Chapman, M. Fulchignoni, H. Moore, G. Neukum, P. Schultz, L. Soderblom, R. Strom, A. Woronow, R. Y. (1979), Standard Techniques for Presentation and Analysis of Crater Size-Frequency Data, Icarus, 37, 467-474.

Barrat, J.-A., A. Yamaguchi, B. Zanda, C. Bollinger, M. Bohn (2010), Relative chronology of crust formation on asteroid Vesta: Insights from the geochemistry of diogenites, Geochim. Cosmochim. Acta, 74(21), 6218-6231, doi:10.1016/j.gca.2010.07.028.

Beck, A. W., and H. Y. McSween (2010), Diogenites as polymict breccias composed of orthopyroxenite and harzburgite, Meteorit. Planet. Sci., 45(5), 850-872, doi:10.1111/j.1945-5100.2010.01061.x.

Beck, P., J.-A. Barrat, F. Grisolle, E. Quirico, B. Schmitt, F. Moynier, P. Gillet, C. Beck (2011), NIR spectral trends of HED meteorites: Can we discriminate between the magmatic evolution, mechanical mixing and observation geometry effects?, Icarus, 216(2), 560-571, doi:10.1016/j.icarus.2011.09.015.

Beck, A.W., K.C. Welten, H.Y., McSween, C.E. Viviano, C.W. Caffee (2012), Petrologic diversity among the PCA 02 howardite group, one of the largest pieces of the vestan surface. Meteorit. Planet. Sci. 47:947-969.

Binzel, R. P., and S. Xu (1993), Chips off of asteroid 4 Vesta: Evidence for the parent body of basaltic achondrite meteorites, Science 260, pp.186-191.

Bischoff, A., E.R.D. Scott, K. Metzler, C.A. Goodrich (2006), Nature and origins of meteorite breccias, in Meteorites and the early solar system II, D.S. Lauretta and H.Y. McSween (eds), 697-712, Univ. of Arizona Press, Tucson, AZ.

Bode, J.E. (1825), Entwurf der astronomischen Wissenschaften, G. Reiner, Berlin. p.147.

Bohren, C.F., and D.R. Huffman (1983), Absorption and Scattering of Light by Small Particles, Wiley, New York.

Bonnefoy, N., O. Brissaud, B. Schmitt, S. Douté, M. Fily, W. Grundy, P. Rabou (2000), Experimental system for the study of planetary surface materials BDRF, Remote sensing reviews, 19, 59-74.

Bottke, W. F., M. C. Nolan, R. Greenberg, R. A. Kolvoord (1994), Velocity distribution among colliding asteroids, Icarus, 107, 255-268.

Buczkowski, D.L., D.Y. Wyrick, M. Toplis, R.A. Yingst, D.A. Williams, W.B. Garry, S. Mest, et al. (2014), The unique morphology and physical properties of the Vestalia Terra plateau, Icarus, 244, 89-103, doi:10.1016/j.icarus.2014.03.035.

Burbine, T.H., T.J. McCoy, A. Meiborn, B. Gladman, K. Keil (2002), Meteoritic Parent Bodies: Their Number and Identification, in Asteroids III, W. F. Bottke Jr., A. Cellino, P. Paolicchi, and R. P. Binzel (eds), 653-667, Univ. of Arizona Press, Tucson, AZ.

Burbine, T. H., P. C. Buchanan, T. Dolkar and R. P. Binzel (2009), Pyroxene mineralogies of near-Earth vestoids, Meteorit. Planet. Sci., 44(9), 1331-1341, doi: 10.1111/j.1945-5100.2009.tb01225.x.

Burns, R.G. (1993), Mineralogical applications of crystal field theory. Cambridge topics in mineral physics and chemistry, band 5. Cambridge University Press.

Bus, S.J. and R.P. Binzel (2002), Phase II of the Small Main-Belt Asteroid Spectroscopic Survey: the Observations, Icarus, 158, 106-145, doi:10.1006/icar.2002.6857.

Capaccioni, F., P. Cerroni, M. A. Barucci, M. Fulchignoni (1990), Phase curves of meteorites and terrestrial rocks - laboratory measurements and applications to asteroids, Icarus 83, 325-348, doi: 10.1016/0019-1035(90)90071-G.

Capria, M.T. and S. Joy (2011), VIR standard data products and archive volume software specification, Planetary Data System, Planetary Science Institute.

Carter, J., and F. Poulet (2013), Ancient plutonic processes on Mars inferred from the detection of possible anorthositic terrains, Nature Geoscience, 6, 1008-1012, doi:10.1038/NGEO1995.

Chandrasekhar, S. (1960), Radiative Transfer. Dover, New York.

Chapman, C.R., and J.W. Salisbury (1973), Comparisons of meteorite and asteroid spectral reflectivities, Icarus, 19, 507-522.

Clark, R.N., and T.L. Roush (1984), Reflectance spectroscopy: quantitative analysis techniques for remote sensing applications, J. Geophys. Res., 89(B7), 6329-6340, doi:10.1029/JB089iB07p06329.

Clark, R.N. (1999), Spectroscopy of rocks and minerals and principles of spectroscopy, in Remote sensing for the Earth sciences: manual of remote sensing, 3 ed., vol.3, A.N. Rencz (ed), John Wiley & Sons, ISBN: 978-0-471-29405-4.

Clayton, R.N., and T.K. Mayeda (1983), Oxygen isotopes in eucrites, shergottites, nakhlites, and chassignites, Earth and Planetary Science Letters, 62, 1-6.

Clayton, R.N., and T.K. Mayeda (1996), Oxygen isotope studies of achondrites, Geochem. Cosmochim. Acta, 60, 1999-2017.

Clenet, H., M. Jutzi, J.-A. Barratt, E. Asphaug, W. Benz, and P. Gillet (2014), A deep crust-mantle boundary in the asteroid Vesta, Nature, 511, 303-306, doi:10.1038/13499.

Cloutis, E.A., M.J. Gaffey, T.L. Jackowski, and K.L. Reed (1986), Calibrations of phase abundance, composition, and particle size distribution for olivine-orthopyroxene mixtures from reflectance spectra, J. Geophys. Res., 91(B11), 11641, doi:10.1029/JB091iB11p11641.

Cloutis, E.A., P. Houdon, T. Hiroi, M.J. Gaffey, P. Mann (2011), Spectral reflectance properties of carbonaceous chondrites: 2. CM chondrite, Icarus, 216, 309-346, doi:10.1016/j.icarus.2011.09.009.

Cloutis, E.A., M.R.M. Izawa, L. Pompilio, V. Reddy, H. Hiesinger, A. Nathues, P. Mann, L. Le Corre, E. Palomba, J.F. Bell III (2013), Spectral reflectance properties of HED meteorites + CM2 carbonaceous chondrites: comparison to HED grain size and compositional variations and implications for the nature of low-albedo features on asteroids 4 Vesta, Icarus, 223, 850-877, doi:10.1016/j.icarus.2013.02.003.

Consolmagno, G., D. Turrini, G. Golabek, V. Svetsov, S. Sirono, K. Tsiganis (2014), Vesta is not an intact protoplanet, Asteroids Comets Meteors conference, Helsinki, conference abstract.

Cruiskshank, D.P., D.J. Tholen, W.K. Hartmann, J.F. Bell, and R.H. Brown (1991), Three basaltic Earth-approaching asteroids and the source of the basaltic meteorites, Icarus, 86, 1-13.

Davis, D.R., C.R. Chapman, S.T. Weidenschilling, R. Greenberg (1985), Collisional history of asteroids: evidence from Vesta and the Hirayama families, Icarus, 62, 30-53.

De Pater, I., J.J. Lissauer (2010), Planetary Sciences, Cambridge University Press, ISBN: 9781107091610.

De Sanctis, M.C., A. Coradini, E. Ammannito, G. Filacchione, M.T. Capria, S. Fonte, G. Magni, et al. (2011), The VIR Spectrometer, Space Sci. Rev., 163(1-4), 329-369, doi:10.1007/s11214-010-9668-5.

De Sanctis, M.C., E. Ammannito, M.T. Capria, F. Tosi, F. Capaccioni, F. Zambon, F. Carraro, et al. (2012), Spectroscopic characterization of mineralogy and its diversity across Vesta, Science, 336, 697-700, doi:10.1126/science.1219270.

De Sanctis, M.C., E. Ammannito, M.T. Capria, F. Capaccioni, J.-P. Combe, A. Frigeri, A. Longobardo, et al. (2013), Vesta's mineralogical composition as revealed by the visible and infrared spectrometer on Dawn, Meteorit. Planet. Sci., 48(11), 2166-2184, doi:10.1111/maps.12138.

Denevi, B.W., P.G. Lucey, E.J. Hochberg, D. Steutel (2007), Near-infrared optical constants of pyroxene as a function of iron and calcium content, J. Geophys. Res., 112, E05009, doi:10.1029/2006JE002802.

Denevi, B. W., D. T. Blewett, D. L. Buczkowski, F. Capaccioni, M. T. Capria, M. C. De Sanctis, W. B. Garry, R. W. Gaskell, L. Le Corre, J.-Y. Li, et al. (2012), Pitted terrain on Vesta and implications for the presence of volatiles, Science, 338, 246, 10.1126/science.1225374.

Douté, S., and B. Schmitt (1998), A multilayer bidirectional reflectance model for the analysis of planetary surface hyperspectral images at visible and near infrared wavelengths. J. Geophys. Res. 103, E13, 31367-31389.

Filacchione, G. and E. Ammannito (2011), Dawn VIR calibration document, Planetary Data System, Planetary Science Institute.

Filacchione, G. (2006), Calibrazione a terra e prestazioni in volo di spettrometri ad immagine e nel vicino infrarosso per l´esploratione planetaria, PhD thesis, Università degli studi di Napoli Federico II. Napoli.

Fordera Srui, G., A. Manara, P. Scioli (2002), Giuseppe Piazzi and the discovery of Ceres, in Asteroids III, W. F. Bottke, A. Cellino, P. Paolicchi, R. P. Binzel editors, The University of Arizona Press, Tucson, AZ.

Fowler, G.W., Papike, J.J., Spilde, M.N., Shearer, C.K. (1995), Diogenites as asteroidal cumulates. Insights from orthopyroxene trace element chemistry. Geochim. Cosmochim. Acta 59, 3071-3084.

Gaffey, M.J. (1993), Forging an asteroid-meteorite link, Science, 260, 167-168.

Gaffey, M.J. (1997), Surface Lithologic Heterogeneity of Asteroid 4 Vesta, Icarus, 127, 130-157, doi:10.1006/icar.1997.5680

Gaffey, M.J., E.A. Cloutis, M.S. Kelly, and K.L. Reed (2002), Mineralogy of asteroids, in Asteroids III, W. F. Bottke Jr., A. Cellino, P. Paolicchi, and R. P. Binzel (eds), 183-204, Univ. of Arizona Press, Tucson, AZ.

Gosh, A., and H.Y. McSween Jr. (1998), A thermal model for the differentiation of asteroid 4 Vesta, based on radiogenic heating, Icarus, 134, 187-206, IS985956.

Gradie, J. and J. Veverka (1986), The wavelength dependence of phase coefficients, Icarus 66, 455-467, doi: 10.1016/0019-1035(86)90085-0.

Gradie, J., J. Veverka, and B. Buratti (1980), The effects of scattering geometry on the spectrophotometric properties of powdered material, Proc. Lunar Planet. Sci. Conf. 11th, Houston, TX, 799-815.

Greeley R. and R.M. Batson (eds) (1990), Planetary mapping, Cambridge Planetary Science Series, Cambridge University Press. ISBN 00-521-30774-0.

Greenberg, R., J.F., Wacker, W.K. Hartmann, C.R. Chapman (1978), Planetesimals to planets: numerical simulations of collisional evolution, Icarus, 35, 1-26.

Gunderson, K., B. Lüthi, P. Russell, N. Thomas (2007), Visible/NIR photometric signatures of liquid water in martian regolith simulant, Planetary and Space Science, 55, 1272-1282, doi:10.1016/j.pss.2007.03.004.

Hapke, B.W. 1981. Bidirectional reflectance spectroscopy. I. Theory. J. Geophys. Res. 86,4571-4586.

Hapke, B.W. (2008), Bidirectional reflectance spectroscopy: 6 effects of porosity, Icarus, 195, 918-926, doi:10.1016/j.icarus.2008.01.003.

Hapke, B.W. (2012), Theory of reflectance and emittance spctroscopy, second ed., Cambridge University Press, New York.

Harlow, G. E., and R., Klimentidis (1980), Clouding of pyroxene and plagioclase in eucrite: implications for post-crystallization processing, Proc. Lunar Planet. Sci. Conf. 11th, Houston, TX, 1131-1143.

Hartmann, W. K. (1966), Ealy lunar cratering, Icarus 5, 406-418.

Hazen, R.M., P.M. Bell, H.K. Mao (1978), Effects of compositional variation on absorption spectra of lunar pyroxene, Proc. Lunar Planet. Sci. Conf. 9th, 2919-2934.

Hardersen, P.S., V. Reddy, R. Roberts, A. Mainzer (2014), More chips off of asteroid (4) Vesta: characterization of eight Vestoids and their HED meteorite analogs, Icarus, 242, 269-282.

Head, J.W., C.I. Fassett, S.J. Kadish, D.E. Smith, M.T. Zuber, G.A. Neumann, E. Mazarico (2010), Global distribution of large lunar craters: Implications for resurfacing and impactor populations, Science, 329, 1503-1507, doi:10.1126/science.1195050.

Herschel, W., (1802), Letter to Joseph Banks, dated 10 June 1802, Dawson Turner Collection 13, 163-164, Natural History Museum, London.

Hiesinger, H., R. Jaumann, G. Neukum, J.W. Head (2000), Ages of mare basalts on the lunar nearside, J. Geophys. Res., 105, 29239-29275, 2000JE001244.

Hilton, J.L. (2002), Asteroid Masses and Densities, in Asteroids III, W. F. Bottke Jr., A. Cellino, P. Paolicchi, and R. P. Binzel (eds), Univ. of Arizona Press, Tucson, AZ.

Hiroi, T., C.M. Pieters, H. Takeda (1994), Grain size of the surface regolith of asteroid 4 Vesta estimated from its reflectance spectrum in comparison with HED meteorites. Meteoritics 29, 3, 394-396

Housen, K.R., and K.A., Holsapple (2011), Ejecta from impact craters, Icarus, 211(1), 856-875, doi:10.1016/j.icarus.2010.09.017.

Hutchison, R. (2004), Meteorites, Cambridge University Press, Cambridge, UK, ISBN 0521470102.

Ivanov, B.A. (2001), Mars/Moon Cratering Rate Ratio Estimates, Space Science Reviews, (96), 87-104.

Jaumann, R., D.A. Williams, D.L. Buczkowski, R.A. Yingst, F. Preusker, H. Hiesinger, N. Schmedemann, et al. (2012), Vesta's shape and morphology, Science, 336(6082), 687-90, doi:10.1126/science.1219122.

Jutzi, M., E. Asphaug, P. Gillet, J. Barrat, W. Benz (2013), The structure of the asteroid 4 Vesta as revealed by models of planet-scale collisions., Nature, 494(7436), 207-10, doi:10.1038/nature11892.

Kahn, E. G., O. S. Barnouin, L. Debra, C. M. Ernst, N. Izenberg, S. Murchie, L. M. Prockter (2011), A Tool for the Visualization of Small Body Data, 44th LPSC, Abs.1618. Lunar Planet. Inst., Houston, TX.

Keil, K. (2002), Geological History of Asteroid 4 Vesta: The "Smallest Terrestrial Planet", in Asteroids III, W. F. Bottke Jr., A. Cellino, P. Paolicchi, and R. P. Binzel (eds), Univ. of Arizona Press, Tucson, AZ.

King, P.L., M.S. Ramsey, P.F. McMillan, G. Swayze (2004), Laboratory fourier transform infrared spectroscopy methods for geologic samples, in Infrared Spectroscopy in Geochemistry, Exploration, and Remote Sensing, P. King, M. Ramsey, G. Swayze (eds.), Mineral. Assoc. of Canada, London, ON. Canada.

Kirkwood, D. (1867), Meteoric Astronomy: a treatise on shooting-stars, fire-balls and aerolites, Lippincott and Co, Philadelphia, PA.

Kleine, T., C. Münker, K. Mezger, H. Palme (2002), Rapid accretion and early core formation on asteroids and the terrestrial planets from Hf-W chronometry, Nature, 418, 952-955.

Klima, R.L., C.M. Pieters, and M.D. Dyar (2007), Spectroscopy of synthetic Mg-Fe pyroxenes I: Spin-allowed and spin-forbidden crystal field bands in the visible and near-infrared, Meteorit. Planet. Sci., 42(2), 235-253, doi:10.1111/j.1945-5100.2007.tb00230.x.

Klima, R.L., M.D. Dyar, C.M. Pieters (2011), Near-infrared spectra of clinopyroxenes: Effects of calcium content and crystal structure. Meteorit. Planet. Sci. 46, 379-395.

Kneissl, T., S. Van Gasselt, G. Neukum (2011), Map-projection-independent crater size-frequency determination in GIS environments - New software tool for ArcGIS, Planetary and Space Science, 59(11-12), 1243-1254, doi:10.1016/j.pss.2010.03.015.

Lazzaro, D., T. Michtchenko, J.M., Carvano, R.P. Binzel, S.J. Bus, T.H. Burbine, T. Mothe-Diniz, et al. (2000), Discovery of a basaltic asteroid in the outer main belt, Science, 288, 2033-2035.

Longobardo, A., E. Palomba, F. Capaccioni, M. C. De Sanctis, F. Tosi, E. Ammannito, S. E. Schröder, et al. (2014), Photometric behavior of spectral parameters in Vesta dark and bright regions as inferred by the Dawn VIR spectrometer, Icarus, 240, 20-35, doi:10.1016/j.icarus.2014.02.014.

Marchi, S., H.Y. McSween, D.P. O´Brien, P. Schenk, M.C. De Sanctis, R. Gaskell, R. Jaumann, et al. (2012), The violent collisional history of asteroid 4 Vesta, Science, 336(6082), 690-694, doi:10.1126/science.1218757.

McCarthy, D.W., J.D. Freeman, J.D. Drummond (1994), High resolution images of Vesta at 1.65 µm, Icarus, 108, 285-297.

McCord, T.B., J.B. Adams, T.V. Johnson (1970), Asteroid Vesta: Spectral reflectivity and compositional implications. Science 168, 1445-1447.

McCord, T.B. J.-Y. Li, J.-P. Combe, H.Y. McSween, R. Jaumann, V. Reddy, F. Tosi, et al. (2012), Dark material on Vesta from the infall of carbonaceous volatile-rich material, Nature, 491(7422), 83-6, doi:10.1038/nature11561.

McFadden, L.A., T.B. McCord, C. Pieters (1977), Vesta: the first pyroxene band from new spectroscopic measurements, Icarus, 31, 439-446.

McSween, H.Y., A. Gosh, R.E. Grimm, L. Wilson, E.D. Young (2002), Thermal Evolution Models of Asteroids, in Asteroids III, W. F. Bottke Jr., A. Cellino, P. Paolicchi, and R. P. Binzel (eds), Univ. of Arizona Press, Tucson, AZ.

McSween, H.Y., D. W. Mittlefehldt, A. W. Beck, R. G. Mayne, T.J. McCoy (2011), HED Meteorites and Their Relationship to the Geology of Vesta and the Dawn Mission, Space Science Reviews, 163(1-4), 141-174, doi:10.1007/s11214-010-9637-z.

McSween, H.Y. E. Ammannito, V. Reddy, T.H. Prettyman, A.W. Beck, M.C. De Sanctis, A. Nathues, et al. (2013), Composition of the Rheasilvia basin, a window into Vesta ' s interior, J. Geophys. Res., 118, doi:10.1002/jgre.20057.

Melosh, H.J. (1989), Impact cratering a geological process. Oxford Monographs on Geology and Geophysics No. 11. Oxford University Press (ISBN 0-19-504284-0).

Metzler, K., K.D. Bode, H. Palme, B. Spettel, D. Stöffler (1995), Thermal and impact metamorphism on the HED parent asteroid, Planet. Space Sci. 43, Nos. 3/4, 499-525.

Michael, G.G., and G. Neukum (2010), Planetary surface dating from crater size - frequency distribution measurements: Partial resurfacing events and statistical age uncertainty, Earth and Planetary Science Letters, 294(3-4), 223-229, doi:10.1016/j.epsl.2009.12.041.

Migliorini, F., A. Morbidelli, V. Zappala, B.J. Gladman, M.E. Bailey, A. Cellino (1997), Vesta fragments from v6 and 3:1 resonances: implications for V-type near-Earth asteroids and howardite, eucrite and diogenite meteorites, Meteorit. Planet. Sci., 32, 903-916.

Mittlefehldt, D.W. (1994), The genesis of diogenites and HED parent body petrogenesis. Geochim. Cosmochim. Acta 58, 1537-1552.

Mittlefehldt, D.W. (2000), Petrology and geochemistry of the Elephant Moraine A 79002 diogenite: A genomict breccia containing a magnesian harzburgite component, Meteorit. Planet. Sci., 35, 901-912.

Mittlefehldt, D.W. (2004), Achondrites, in Treatise on geochemistry, Vol. 1 Meteorites, Comets and Planets, H.D. Holland and K.K. Turekian (eds), ISBN: 978-0-08-043751-4.

Moroz, L., and G. Arnold (1999), Influence of neutral components on relative band contrasts in reflectance spectra of intimate mixtures: Implications for remote sensing: 1. Nonlinear mixing modeling, J. Geophys. Res., 104(E6), 14109, doi:10.1029/1999JE900014.

Moroz, L. (2000), Reflectance Spectra of Olivine-Orthopyroxene-Bearing Assemblages at Decreased Temperatures: Implications for Remote Sensing of Asteroids, Icarus, 147(1), 79-93, doi:10.1006/icar.2000.6430.

Mustard, J.F., and C.M., Pieters (1989), Photometric phase functions of common geologic minerals and applications to quantitative analysis of mineral mixture reflectance spectra, J. Geophys. Res., 94, 13619-13634, 89JB01001.

Nash, D.B., and J.E., Conel (1974), Spectral reflectance systematics for mixtures of powdered hypersthene, labradorite, and ilmenite, J. Geophys. Res., 79, 1615-1621.

Nass, A., S. van Gasselt, R. Jaumann, H. Asche (2011), Implementation of cartographic symbols for planetary mapping in geographic information systems, Planetary and Space Science, 59, 1255-1264.

Nathues, A., M. Hoffmann, M. Schäfer, G. Thangjam, L. Le Corre, V. Reddy, U. Christensen, et al. (2014), Exogenic olivine on Vesta from Dawn Framing Camera color data, Icarus, in press, doi:10.1016/j.icarus.2014.09.045.

Nesse, W. (1998), Introduction to mineralogy, ISBN: 9780199827381, Oxford University Press, USA.

Neukum, G. (1983), Thesis - Feb. 1983 National Aeronautics and Space Administration, Washington, DC. Transl. into english of "Meteoritenbombardement und Datierung Planetarer Oberflaechen" Munich, Feb. 1983.

Neukum, G., B.A. Ivanov, and W.K. Hartmann (2001), Cratering records in the inner solar system in relation to the lunar reference system, Space Science Reviews, 96, 55-86, doi:doi:10.1023/A:1011989004263.

O'Brien, D.P., S. Marchi, A. Morbidelli, W.F. Bottke, P.M. Schenk, C.T. Russell, C.A. Raymond (2014), Constraining the cratering chronology on Vesta, Planetary and Space Science, 103, 131-142, doi:10.1016/j.pss.2014.05.013.

O'Brein, D.P., R. Greenberg (2005), The collisional and dynamical evolution of the main-belt and NEA size distributions, Icarus, 178, 179-212.

O'Brein, D.P., and M.V., Sykes (2011), The origin and evolution of the asteroid belt - implications for Vesta and Ceres, Space Sci. Rev. doi:10.1007/s11214-011-9808-6.

Otto, K., R. Jaumann, K. Krohn, K.-D. Matz, F. Preusker, T. Roatsch, P. Schenk, et al.(2013), Mass-wasting features and processes in Vesta´s south polar basin Rheasilvia, J. Geophys. Res., 118, 2279-2294, doi:10.1002/2013JE004333.

Philibert, J., and R. Tixier (1968), Electron penetration and the atomic number correction in electron probe microanalysis, J. Phys. D1:685.

Pieters, C.M., L.A. McFadden, T. Prettyman, M.C. Sanctis, T. B. McCord, T. Hiroi, R. Klima, et al. (2011), Surface Composition of Vesta: Issues and Integrated Approach, Space Sci. Rev., 163(1-4), 117-139, doi:10.1007/s11214-011-9809-5.

Pieters, C.M. (1983), Strength of mineral absorption features in the transmitted component of near-infrared reflected light: First results from RELAB, J. Geophys. Res., 88(B11), 9534, doi:10.1029/JB088iB11p09534.

Pieters, C.M., E. Ammannito, D.T. Blewett, B.W. Denevi, M.C. De Sanctis, M.J. Gaffey, L. Le Corre, et al. (2012), Distinctive space weathering on Vesta from regolith mixing processes. Nature 491, 7422, doi:10.1038/nature11534.

Polanskey, C.A., S. Joy, C.A. Raymond (2011), Dawn Science Planning, Operations and Archiving, Space Sci. Rev., 163, 511-543, doi:10.1007/s11214-011-9855-z.

Pommerol, A., N. Thomas, M. Affolter, G. Portyankina, B. Jost, K. Seiferlin, K.-M. Aye (2011), Photometry and bulk physical properties of solar system surfaces icy analogs: the planetary ice laboratory at university of Bern, Planetary and Space Science, 59, 1601-1612, doi:10.1016/j.pss.2011.07.009.

Pommerol, A., N. Thomas, B. Jost, P. Beck, C. Okubo, A. S. McEwen (2013), Photometric properties of Mars soils analogs, J. Geophys. Res. 118, 1-28, doi:10.1002/jgre.20158.

Prettyman, T.H., W.C. Feldman, H.Y. McSween Jr., R.D. Dingler, D.C. Enemark, D.E. Patrick, S.A. Storms et al. (2011), Dawn´s gamma ray and neutron detector, Space Sci. Rev. 163:371-459, doi:10.1007/s11214-011-9862-0.

Prettyman, T.H., D.W. Mittlefehldt, N. Yamashita, A.W. Beck, W.C. Feldman, J.S. Hendricks, D.J. Lawrence, et al. (2013), Neutron absorption constraints on the composition of 4 Vesta, Meteorit. Planet. Sci., 48, 11, 2211-2236, doi:10.1111/maps.12244.

Rayman, M.D., T. C. Fraschetti, C.A. Raymond, C.T. Russell (2006), Dawn: A mission in development for exploration of main belt asteroids Vesta and Ceres, Acta Astronautica, 58, 605-616, doi:10.1016/j.actaastro.2006.01.014.

Raymond, C.A., R. Jaumann, A. Nathues, H. Sierks, T. Roatsch, F. Preusker, F. Scholten, et al. (2011), The Dawn topography investigations, Space Sci. Rev., 163, 487-510, doi:10.1007/s11214-011-9863-z.

Raymond, C.A., R.S. Park, S.W. Asmar, A.S. Konopliv, D.L. Buczkowski, M.C. De Sanctis, H.Y. McSween, et al. (2013), Vestalia Terra: An ancient mascon in the southern hemisphere of Vesta, 44th LPSC, Abs. 2882, Lunar Planet. Inst., Houston, TX.

Reddy, V., J.A. Sanchez, A. Nathues, N.A. Moskovitz, J.Y. Li, E.A. Cloutis, K. Archer, et al. (2011), Photometric, spectral phase and temperature effects on 4 Vesta and HED meteorites: Implications for the Dawn mission, Icarus, 217(1), 153-168, doi:10.1016/j.icarus.2011.10.010.

Reddy, V., A. Nathues, L. Le Corre, H. Sierks, J.-Y. Li, R. Gaskell, T. McCoy, et al. (2012), Color and albedo heterogeneity of Vesta from Dawn, Science, 336, 6082, 700-4, doi:10.1126/science.1219088.

Reed, S. J. B. (1993), Electron microprobe analysis, Cambridge University Press, Cambridge.

Righter, K., and M. J. Drake (1997), A magma ocean on Vesta: core formation and petrogenesis of eucrite and diogenites, Meteorit. Planet. Sci., 32, 929-944.

Roatsch, T., E. Kersten, K. Matz, F. Preusker, F. Scholten, and R. Jaumann (2012), High resolution Vesta High Altitude Mapping Orbit (HAMO) Atlas derived from Dawn framing camera images, Planetary and Space Science, 73, 283-286, doi:10.1016/j.pss.2012.08.021.

Roatsch, T., E. Kersten, K.-D. Matz, F. Preusker, F. Scholten, S. Elgner, R. Jaumann, et al.(2013), High-resolution Vesta Low Altitude Mapping Orbit Atlas derived from Dawn Framing Camera images, Planet. Space Sci., 85, 293-298, doi:10.1016/j.pss.2013.06.024.

Russell, C.T., A. Coradini, U. Christensen, M.C. De Sanctis, W.C. Feldman, R. Jaumann, H.U. Keller, et al. (2003), Dawn: a journey in space and time, Planetary and Space Science, 52, 465-489, doi:10.1016/j.pss.2003.06.013.

Russell, C.T., C.A. Raymond, T.C. Fraschetti, M.D. Rayman, C.A. Polanskey, K.A. Schimmels, S.P. Joy (2006), Dawn mission and operations, Proceedings International Astronomical Union Symposium No. 229, 2005, D. Lazzaro, S. Ferraz-Mello and J. A. Fernandez (eds).

Russell, C.T., and C.A. Raymond (2011), The Dawn Mission to Vesta and Ceres, Space Science Reviews, 163(1-4), 3-23, doi:10.1007/s11214-011-9836-2.

Russell, C.T., C.A. Raymond, R. Jaumann, H.Y. McSween, M.C. De Sanctis, A. Nathues, T.H. Prettyman, et al. (2013), Dawn completes its mission at 4 Vesta, Meteorit. Planet. Sci., 48(11), 2076-2089, doi:10.1111/maps.12091.

Ruzicka, A., G. A. Snyder, and L. A. Taylor (1997), Vesta as the howardite, eucrite and diogenite parent body: Implications for the size of a core and for large-scale differentiation, Meteorit. Planet. Sci., 32(6), 825-840, doi:10.1111/j.1945-5100.1997.tb01573.x.

Safronov, V.S. (1969), Evolution of the protoplanetary cloud and the formation of the Earth and planets. Nauka, Moscow, NASA TTF-677, US Government Printing Office, Washington, DC, 1972.

Schilling, C. (1894), Wilhelm Olbers: sein Leben und seine Werke, J. Springer, Berlin.

Schröder, S.E., Ye. Grynko, A. Pommerol, H.U. Keller, N. Thomas, and T.L. Roush (2014), Laboratory observations and simulations of phase reddening, Icarus, 239, 201-216, doi: 10.1016/j.icarus.2014.06.010.

Schubart, J., and D. L. Matson (1979), Masses and densities of asteroids, in Asteroids I, T. Gehrels editor, The University of Arizona Press, Tucson, AZ.

Scott, E.R.D., R.C. Greenwood, I.A. Franchi, I.S. Sanders (2009), Oxygen isotopic constraints on the origin and parent bodies of eucrites, diogenites, and howardites, Geochim. Cosmochim. Acta, 73, 5835-5853, doi:10.1016/j.gca.2009.06.024.

Shearer, C.K., G.W. Fowler, J.J. Papike (1997), Petrogenetic models for magmatism on the eucrite parent body: evidence from orthopyroxene in diogenites, Meteorit. Planet. Sci., 32, 877-889.

Shearer, C.K., P. Burger, J.J. Papike (2010), Petrogenetic relationships between diogenites and olivine diogenites: Implications for magmatism on the HED parent body, Geochim. Cosmochim. Acta, 74(16), 4865-4880, doi:10.1016/j.gca.2010.05.015.

Shepard, M.K., and P. Helfenstein (2007), A test of the Hapke photometric model, J. Geophys. Res., 112, E03001, doi:10.1029/2005JE002625.

Shkuratov, Y., L. Starukhina, H. Hoffmann, G. Arnold (1999), A model of spectral albedo of particulate surfaces: implications for optical properties of the moon, Icarus, 137, 235-246.

Sierks H., H.U. Keller, R. Jaumann, H. Michalik, T. Behnke, F. Bubenhagen, I. Büttner, U. Carsenty, U. Christensen, R. Enge, et al. (2011), The Dawn Framing Camera, Space Science Reviews, doi:10.1007/s11214-011-9745-4.

Singer, R.B., (1981), Near-infrared spectral reflectance of mineral mixtures: systematic combinations of pyroxenes, olivine, and iron oxides, J. Geophys. Res. 86, B9, pp 7967-7982.

Snyder, J.P. (1987), Map Projections: A Working Manual. US Government Printing Office, Washington, DC.

Stöffler, D. and G. Ryder (2001), Stratigraphy and isotope ages of lunar geologic units: chronological standard for the inner solar system, Space Science Reviews, volume 96, No. 1-4.

Strom, R.G., R. Malhotra, T. Ito, F. Yoshida, D.A. King (2005), The origin of planetary impactors in the inner solar system, Science, 309, 1847-1850, doi:10.1126/science.1113544.

Sunshine, J.M., and C.M. Pieters (1998), Determining the composition of olivine from reflectance spectroscopy, J. Geophys. Res., 103(E6), 13675-13688.

Takeda, H., and A.L. Graham (1991), Degree of equilibration of eucritic pyroxenes and thermal metamorphism of the earliest planetary crust, Meteoritics, 26, 129-134.

Takeda, H. (1979), A layered-crust model of a Howardite parent body, Icarus, 40(3), 455-470, doi:10.1016/0019-1035(79)90039-3.

Tanaka, K. L., J. A. Skinner, L. S. Crumpler, J. M. Dohm (2009), Assessment of planetary geologic mapping technique for Mars using terrestrial analogs: the SP mountain area of the San Francisco Volcanic Field, Arizona, Planetary and Space Science 57, 510-532.

Terada, K., and A. Bischoff (2009), Asteroidal granite-like magmatism 4.53 Gyr ago, The astronomical journal, 699:L68, doi:10.1088/0004-637X/699/2/L68.

Thomas, V.C., J.M. Makowski, G.M. Brown, J.F. McCarthy, D. Bruno, J.C. Cardoso, et al. (2011), The Dawn spacecraft, Space Sci. Rev. 163:175-249, doi: 10.1007/s11214-011-9852-2.

Thomas, P. C., R. P. Binzel, M. J. Gaffey, A. D. Storrs, E. N. Wells, and B. H. Zellner (1997), Impact Excavation on Asteroid 4 Vesta: Hubble Space Telescope Results, Science 277, 1492-1495.

Warren, P.H. (1985), Origin of howardite, diogenite and eucrites: a mass balance constraint, Geochemica Cosmochim.Acta, 49, 5577-586.

Warren, P.H. (1997), Magnesium oxide-iron oxide mass balance constraints and a more detailed model for the relationship between eucrites and diogenites, Meteorites early Sol. Syst. II, 32, 945-963.

Wasson, J.T. (2013), Vesta and extensively melted asteroids: why HED meteorites are probably not from Vesta, Earth and Planet. Sci. Let., 381, 138-146, doi: 10.1016/j.epsl.2013.09.002.

Weidenschilling, S.J., and J.N. Cuzzi (2006), Accretion Dynamics and Timescales: Relation to Chondrites, in Meteorites and the Early Solar System II, D. S. Lauretta and H. Y. McSween Jr. (eds.), Univ. of Arizona Press, Tucson, AZ.

Werner, S.C. (2005), Major aspects of the chronostratigraphy and geologic evolutionary history of Mars, PhD Thesis, Freie Universität Berlin, Berlin.

Wetherill, G.W., and G.R. Stewart (1989), Accumulation of a swarm of small planetesimals, Icarus, 77, 330-357.

Wiechert, U.H., A.N. Halliday, H. Palme, D. Rumble (2004), Oxygen isotope evidence for rapid mixing of the HED meteorite parent body, Earth and Planetary Science Letters, 221, 373-382, doi:doi:10.1016/S0012-821X(04)00090-1.

Wilhelms, D.E., V.R. Oberbeck, H.R. Aggarwal (1978), Size-frequency distributions of primary and secondary lunar impact craters, Proc. Lunar Planet Sci. Conf. 9th, 3735-3762. Lunar and Planetary Institute.

Wilhelms, D.E. (1990), Geologic mapping, in Greeley, R, and Batson, R.M., eds., Planetary Mapping: New York, Cambridge University Press, p. 208-260.

Williams, D.A., D.P. O'Brein, P.M. Schenk, B.W. Denevi, U. Carsenty, S. Marchi, J.E. Scully, et al. (2014), Lobate and flow-like features on asteroid Vesta, Planetary and Space Science, 103, 24-35, doi:10.1016/j.pss.2013.06.017.

Williams, D.A., R. Jaumann, H.Y. McSween, S. Marchi, N. Schmedemann, C.A. Raymond, C.T. Russell (2014), The chronostratigraphy of protoplanet Vesta, Icarus, 244, 158-165. doi:10.1016/j.icarus.2014.06.027.

Wilson, L., and K. Keil (2012), Volcanic activity on differentiated asteroids: a review and analysis, Chemie der Erde, 72, 289-321, doi:10.1016/j.chemer.2012.09.002.

Wray, J.J., S.T. Hansen, J. Dufek, G.A. Swayze, S.L. Murchie, F.P. Seelos, J.R. Skok, R.P. et al. (2013), Prolonged magmatic activity on Mars inferred from the detection of felsic rocks, Nature Geoscience, 6, 1013-1017, doi:10.1038/NGEO1994.

Yamaguchi, A., G. J. Taylor, K. Keil (1996), Global crustal metamorphism of the eucrite parent body, Icarus, 124, 97-112.

Yamaguchi, A., J.-A. Barrat, M. Ito, and M. Bohn (2011), Posteucritic magmatism on Vesta: Evidence from the petrology and thermal history of diogenites, J. Geophys. Res., 116(E8), E08009, doi:10.1029/2010JE003753.

Yamashita, N., T.H. Prettyman, D.W. Mittlefehldt, M.J. Toplis, T.J. McCoy, A.W. Beck, R.C. Reed, et al. (2013), Distribution of iron on Vesta, Meteorit. Planet. Sci., 48(11), 2237-2251, doi:10.1111/maps.12139.

Zachariasen, W.H. (1967), A general theory of x-ray diffraction in crystals, Acta Cryst. 23, 558.

Zambon, F., M.C. De Sanctis, S. Schröder, F. Tosi, J.-Y. Li, A. Longobardo, E. Ammannito, D.T. Blewett, et al. (2014), Spectral analysis of the bright materials on the asteroid Vesta.Icarus, 240, 73-85, doi:10.1016/j.icarus.2014.04.037.

Zolensky, M., M.K. Weisberg, P.C. Buchanan, D.W. Mittlefehldt (1996), Mineralogy of carbonaceous chondrite clasts in HED achondrites and the Moon, Meteoritics and Planetary Science, 31, 518-537.

Conferences and meetings attended during the course of the PhD
(in chronological order)

- European Planetary Science Conference (EPSC) – Division of Planetary Sciences (DPS) of the American Astronomical Society Joint Meeting 2011, October 02-07, 2011, Nantes, France.
- 43rd Lunar and Planetary Science Conference (LPSC), March 19-23, 2012, Houston, TX, United States.
- Dawn Science Team Meeting, March 25-27, 2012, Washington, DC, United States.
- European Geosciences Union (EGU), General Assembly 2012, 22-27 April, 2012, Vienna, Austria.
- EPSC Meeting 2012, September 23-28, 2012, Madrid, Spain.
- Dawn Science Team Meeting, October 1-3, 2012, Rome, Italy.
- Paneth Kolloquium, October, 2012, Nördlingen, Germany.
- 44rd Lunar and Planetary Science Conference (LPSC), March 18-22, 2013, Houston, TX, United States.
- Vesta Crater Chronology Meeting, April 25-26, 2013, Boulder, CO, United States.
- Dawn Science Team Meeting, May 28-31, 2013, Providence, RI, United States.
- EPSC Meeting 2012, September 08-13, 2013, London, United Kingdom.
- Dawn Science Team Meeting, November 20-22, 2013, Laurel, MD, United States.
- Vesta in the light of Dawn, February 3-4, 2014, Houston, TX, United States.
- 45rd Lunar and Planetary Science Conference (LPSC), March 17-21, 2014, Houston, TX, United States.
- Dawn Science Team Meeting, May 20-22, 2014, Berlin, Germany.

Abstracts related to the PhD submitted to conferences and meetings

If first authored, the type of presentation (i.e., poster/oral) is indicated.

LPSC (Lunar and Planetary Science Conference) 03/2012 Poster presentation
Geologic Mapping of the Av-2 Bellicia Quadrangle of 4 Vesta
Ruesch, O.; Hiesinger, H., Schmedemann, N.; Kneissl, T., Blewett, D. T., Williams, D. A., Russell, C. T.; Raymond, C. A.

LPSC 03/2012
Smooth Pond-Like Deposits on Asteroid 4 Vesta: Preliminary Results from the Dawn Mission
Hiesinger, H.; Ruesch, O., Jaumann, R.; Nathues, A., Raymond, C. A.; Russell, C. T.

EGU (European Geophysical Union General Assembly) 04/2012
Smooth pond-like deposits on asteroid 4 Vesta: First results from the Dawn mission
Hiesinger, H.; Ruesch, O., Jaumann, R.; Nathues, A., Raymond, C. A.; Russell, C. T.

EGU 04/2012 Poster presentation
Geologic mapping of the Av-2 Bellicia quadrangle of asteroid 4 Vesta
Ruesch, O.; Hiesinger, H., Schmedemann, N.; Kneissl, T., Blewett, D. T., Williams, D. A., Russell, C. T.; Raymond, C. A.

EPSC (European Planetary Science Conference) 09/2012 Poster presentation
Influence of Observation Geometry and Composition on Vis-NIR Spectra of HED Meteorites
Ruesch, O.; Hiesinger, H., Metzler, K.; Nathues, A., Cloutis, E. A.; Reddy, V., Le Corre, C.; Mann, P. J.

Paneth Kolloquium 10/2012 Oral presentation
Influence of Observation Geometry and Composition on Vis-NIR Spectra of HED Meteorites
Ruesch, O.; Hiesinger, H., Metzler, K.; Nathues, A., Cloutis, E. A.; Reddy, V., Le Corre, C.; Mann, P. J.

LPSC 03/2013
Lunar-Like Chronology for Vesta --- Crater Retention Ages Matching Independent Ar-Ar HED Ages
Schmedemann, N.; Kneissl, T., Ivanov, B. A.; Michael, G. G., Neukum, G.; Nathues, A., Sierks, H.; Wagner, R.; Krohn, K.; Le Corre, L.

LPSC 03/2013 Poster presentation
Assessment of HED Spectral Variability: Observation Geometry and Accuracy in Retrieving Composition
Ruesch, O.; Hiesinger, H.; Metzler, K.; Kallisch, J.; Cloutis, E. A.; Reddy, V.; Le Corre, L.; Mann, P. J.; Nathues, A.

LPSC 03/2013
Geologic Map of the Northern Hemisphere of Vesta Based on Dawn FC Images
Hiesinger, H.; Ruesch, O.; Blewett, D. T.; Buczkowski, D. L.; Scully, J. E. C.; Williams, D. A.; Yingst, R. A.; Russell, C. T.; Raymond, C. A.

EGU 04/2013
Crater Retention Ages from (4) Vesta Matching Independent Ar-Ar Ages of HED Meteorites
Schmedemann, N.; Kneissl, T. Ivanov, B. A.; Michael, G. G.; Neukum, G.; Nathues, A. Sierks, H.; Wagner, R.; Krohn, K.; Le Corre, L.

EGU 04/2013
Geologic Map of the Northern Hemisphere of Vesta
Hiesinger, H.; Ruesch, O.; Blewett, D. T.; Buczkowski, D. L.; Scully, J.; Williams, D. A.; Aileen Yingst, R.; Russell, C. T.; Raymond, C. A.

Vesta Crater Chronology Meeting 04/2013 Oral presentation
Stratigraphy of Vesta northern hemisphere
Ruesch, O. Hiesinger, H.

DPS (Division of Planetary Science - American Astronomical Society) 10/2013
A compositional and geological view into ejecta of small fresh impact craters on asteroid 4 Vesta
Stephan, K.; Jaumann, R.; De Sanctis, M. C.; Tosi, F.; Ammannito, E.; Krohn, K.; Zambon, F.; Marchi, S.; Ruesch, O.; Matz, K.

LPSC 02/2014
Geomorphology and Structural Geology of Saturnalia Fossae and Adjacent Structures in the Northern Hemisphere of Vesta
Scully, J. E. C.; Yin, A.; Russell, C. T.; Buczkowski, D. L.; Williams, D. A.; Blewett, D. T.; Ruesch, O.; Hiesinger, H.; Le Corre, L.; Mercer, C.

Vesta in the light of Dawn 02/2014 Oral presentation
Some more Locations of Possible Exposed Olivine on Vesta Using VIR/Dawn Data
Ruesch, O.; Hiesinger, H.; De Sanctis, M. C.; Ammannito, E.; Palomba, E.; Longobardo, A.; Capria, M. T.; Capaccioni, F.; Frigeri, A.; Tosi, F.

LPSC 03/2014 Poster presentation
Distribution of the Near-IR Spectral Signature of Olivine on Vesta with VIR/Dawn Data: The Ultramafic Side of Vesta´s Surface
Ruesch, O.; Hiesinger, H. DeSanctis, M. C.; Ammannito, E.; Palomba, E.; Longobardo, A.; Capria, M. T.; Capaccioni, F.; Frigeri, A.; Tosi, F.

LPSC 03/2014
Vesta Evolution from Surface Mineralogy: Mafic and Ultramafic Mineral Distribution
De Sanctis, M. C.; Ammannito, E.; Palomba, E.; Longobardo, A.; Mittlefehldt, D. W.; McSween, H. Y.; Marchi, S.; Capria, M. T.; Capaccioni, F.; Frigeri, A.

LPSC 03/2014
Geomorphology and Structural Geology of Saturnalia Fossae and Adjacent Structures in the Northern Hemisphere of Vesta
Scully, J. E. C.; Yin, A.; Russell, C. T.; Buczkowski, D. L.; Williams, D. A.; Blewett, D. T.; Ruesch, O.; Hiesinger, H.; Le Corre, L.; Mercer, C.

LPSC 03/2014 Poster presentation
Marcia Crater, Vesta: Geology, Mineralogy, Composition, and Thermal Properties
Ruesch, O.; Hiesinger, H.; Williams, D. A.; Nathues, A.; Prettyman, T. H.; Tosi, F.; De Sanctis, M. C.; Scully, J. E. C.; Schenk, P. M.; Yingst, R. A.

EGU 04/2014
An in-depth study of Marcia Crater, Vesta
Hiesinger, H.; Ruesch, O.; Williams, D.A.; Nathues, A.; Prettyman, T.H.; Tosi, F.; De Sanctis, M.D.; Scully, C.E.; Schenk, P.; Yingst, R.A.; Denevi, B.W.; Jaumann, R.; Raymond, C.A.; Russell, C.T.

PDS 11/2014
Modal mineralogy of Vesta
Poulet, F. ; Ruesch O.; Hiesinger, H.; Langevin, Y.

Appendix

Peer-review articles I to IX

Non-peer-review articles I to III